Computer Simulations of Self-Assembly, and Critical Phenomena in Complex Fluids

Leonardo Lenoci

A thesis submitted in fulfilment of requirements for the degree of

Doctor of Philosophy

to

School of Chemistry

University of Edinburgh

January 2008

Declaration

I hereby declare that this thesis is of my own composition, and that it contains no material previously submitted for the award of any other degree. The work reported in this thesis has been executed by myself, except where due acknowledgement is made in the text.

Abstract

Biomineralisation is the process by which living organisms produce minerals. Shells and bones are outstanding examples of biominerals, as well as teeth, sea urchin spicules, and diatom cell walls. 80% of biominerals are crystalline solids and only 20% are made by amorphous materials. Interestingly, amorphous biominerals (such as the silica diatom skeletons) often posses highly organised structures. The molecular-scale processes that lead formless material to assume highly symmetric shapes are still largely unknown.

It is currently known that biominerals are composite materials of organic molecules and inorganic materials, such as SiO_2 and $CaCO_3$, and form at ambient conditions. They are often equipped with mesoporous structures which, in the case of diatoms, serve to convoy the oxygen into the cell.

In the case of amorphous biominerals, it is thought that the organic molecules might self-assembly on the nanoscale to form templates around which the inorganic material can then be deposited. On a larger lengthscale (tens of micrometres) phase separation of a binary mixture into an organic phase (around which the inorganic material can be deposited) and an aqueous phase can be the leading phenomenon in biomineralisation. In the first part of this work, we report

computer simulation studies of some biological systems implicated in biomineralisation in order to test the self-assembly and phase separation scenarios, whereas the second part of this thesis is concerned with critical phenomena.

The self-assembly of model peptides has been studied using Brownian dynamics (BD) computer simulations. In particular, a bead-spring coarse-grained model (a model in which a set of molecules is represented by a single bead and the bonding interactions by simple spring forces) has been designed to mimic small proteins called "silaffins" observed to favor the formation of amorphous silica nanospheres *in vitro* and involved in the biomineralisation of certain diatoms cell walls. The coarse-grained model used in the simulations keeps the primary characteristics of the silaffins, these being a 15 amino acid hydrophilic backbone and two modified lysine residues near the ends of the backbone each carrying a hydrophobic polyamine chain. In the simulations, the model peptides self-assemble to form micelles, networks of strands, or bicontinuous structures depending on the peptide concentration and the system temperature. The simulation results show that over a broad range of peptide volume fractions ($0.05 - 25\%$) the characteristic structural lengthscales fall in the range $12 - 45$ nm. This suggests that the self-assembled structures observed may act as either nucleation points or scaffolds for the deposition of $10 - 100$ nm silica-peptide composite building blocks from which diatom skeletons and synthetic nanospheres are made.

A systematic coarse-grained computer-simulation study of the role of putrescine homologues [$H_2N - (CH_2)_n - NH_2$] on silica morphogenesis is presented. Brownian dynamics simulations of model putrescine are performed highlighting the importance of aggregation on the degree of silica deposition. The results suggest that over a broad range of solute concentration ($15 - 50$ mM) the charac-

teristic lengthscales of the observed self-assembled structures correlate with structural properties of the silicas observed in vitro.

We have proposed an experimentally motivated model for the formation of fluid-phase templates corresponding to the porous silica skeletons of diatoms, single-cell organisms found in freshwater and marine environments. It is shown that phase-separation processes on a planar surface could give raise to a quasi-static mold which might direct the deposition of condensing silica to form complex arrays of pores. Our calculations show that appropriate fluid scaffolds can be generated for a number of diatom species. The results can be of some biological relevance, but the most significant advance might be the identification of a reliable synthetic strategy for generating complex porous structures from simple, amorphous materials.

The heat capacity at constant volume, near the critical point, shows a very strong dependence on the particular ensemble employed in the simulations. We study this phenomenon for the three-dimensional Ising model in the canonical ensemble (NVT) and in the grand-canonical (μVT) ensemble. We use Wang-Landau Monte Carlo computer simulations to characterise this dependence and estimate the difference near the critical temperature. We, then, attempt to use our simulation results to obtain useful scaling laws and discuss the ensemble dependence of the constant-volume heat capacity and its still puzzling behaviour.

Acknowledgements

I would like to thank my parents Lia and Claudio, and my sister Paola for their permanent support through the years. A special thank goes to my partner Chiung Ying Ou Yang for being always with me. I also wish to acknowledge my colleagues Alastair Dewar, Peter Duncan, Alex Chremos, Georg Ganzenmüller, and David Martins for sharing their precious time with me.

Many thanks also to Drs. Barran and Dryden for proof-reading one of my papers and Prof. David Mann for being very helpful in discussing diatoms. I am grateful to Prof. John Hodgkiss (Fleetwood, England), Dr. Rex Lowe (Bowling Green State University, U.S.A.), Prof. David Mann (Royal Botanic Garden, Edinburgh) and Dr. Hans Schrader (Ulset, Norway) for granting permission to reproduce experimental images of diatoms. I acknowledge Prof. Paul Madden for useful comments and discussions during my studies here in Edinburgh. I thank the School of Chemistry at the University of Edinburgh for financial support and finally, a huge thank goes to my supervisor Dr Philip J. Camp for being a real friend of mine since my very first day in Edinburgh.

Contents

CHAPTER 1

Introduction

This work is divided into two main parts. In the first part we study self-assembly and phase-separation phenomena in the context of biomineralisation. We use computer simulation techniques to understand the physico-chemical mechanisms involved in the production, for example, of siliceous biominerals with the ultimate goal of deriving new theories and experiments to reproduce them. The second part is concerned with critical phenomena, which are characteristic of physical systems near the critical point of their phase diagram.

1.1 Biomineralisation

Biomineralisation is the process by which living organisms produce and control the growth of inorganic minerals [1]. Rice, cereals, and cucumber, for instance, deposit silica to reinforce their tissues and as a systemic response to pathogen attacks [2]. Other examples of biominerals are bones and shells, but amongst the most extraordinary examples on earth are, perhaps, diatom cell walls. Diatoms are unicellular, photosynthetic organisms living in marine and freshwater environments, and apart from their biological relevance, they are

Figure 1.1: Some diatoms microscopy images. The colours in the figure arise from diffraction effects. The pores in the skeleton allow the oxygen to reach the cell. Reproduced with permission from Ref. [4].

well known because of the amazing, highly ordered structures made of amorphous silica that fashion their skeletons. The forms of the diatom skeletons differ from species to species and are vital for their taxonomical identification. Diatom silica (SiO_2) structures are on the micrometre scale and often posses highly symmetric porous arrays [3] to allow the passage of oxygen. The understanding of the basic processes involved in the formation of these complex porous structures can help derive new strategies for the synthesis and the production of porous materials in the laboratory. Porous materials can be used for a myriad of nanotechnological applications, such as molecular sieving.

Other examples of biominerals include sea urchins [5], whose shells and spines are made of crystalline calcium carbonate ($CaCO_3$), and single crystals of magnetite (Fe_3O_4) which can be found in large quantities in beach sand and in magnetotactic bacteria [6]. Mineralisation of single crystals (on the nanometre lengthscale) is thought to involve different processes from those involved in the formation of the amorphous biominerals, such as the diatoms. Morphological control of single crystals is often associated with preferential absorption exerted by biomolecules on certain faces of a crystal nucleus, directing the mineral growth along specific directions [5, 7]. On the other hand, the morphogenesis of amorphous materials is generally associated with a "templating" mechanism in which biomolecules are thought to self-assemble to offer suitable scaffolds for the subsequent precipitation of the inorganic material [8]. In this thesis we

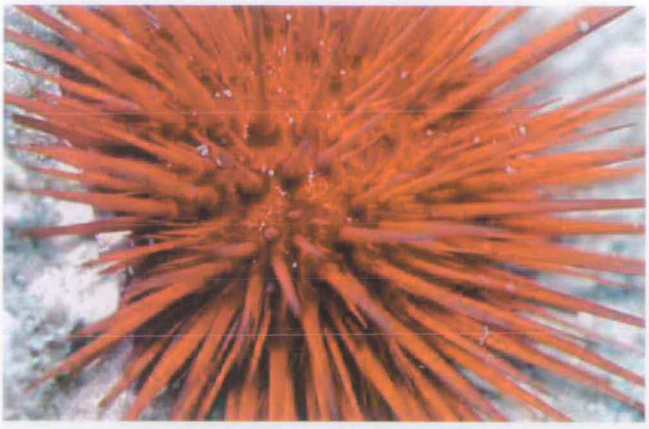

Figure 1.2: A sea urchin and its single-crystal spines. Image taken from Ref. [9].

focus on the templating mechanism and in the morphogenesis of biominerals whose inorganic material is amorphous at least on the nanometre lengthscale. The templating mechanism will be rationalised and tested in in Chapters 3, 4, and 5.

1.1.1 Role of self-assembly in biomineralisation

The composition of amorphous[1] biominerals has been widely studied during the past years. It is well known that they have two components, one inorganic and the other organic [10], and might achieve their final structure at the nanoscale through the self-assembly of organic molecules (proteins and/or lipids) that build the scaffolding which guides the deposition of the inorganic material (e.g. SiO_2, etc.). It is important to note that a similar strategy is currently used to synthesise mesoporous materials such as the MCM-41 which contains rod-like surfactant aggregates [2] [11–13].

[1] At least on the nanometre scale.

[2] We recall that mesoporous materials present pores of diameters between 2 and 50 nm, whereas zeolites are limited to pore sizes of $\sim$ 15Å. In zeolitic materials, therefore, the template is a single molecule or ion.

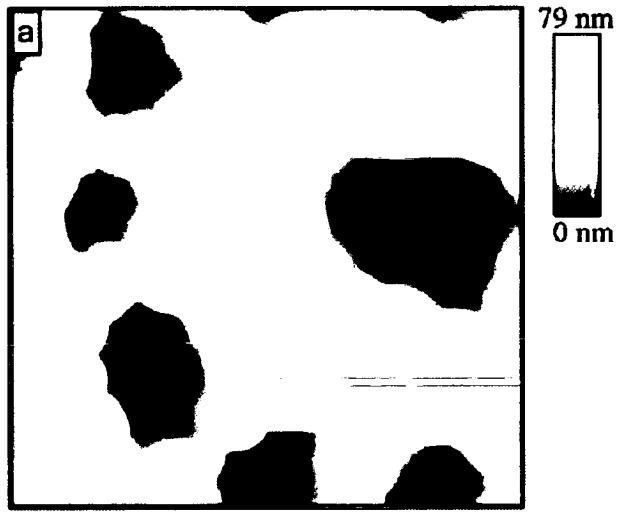

Figure 1.3: AFM image of the outer surface of a valve of diatom *C. granii*. The granular nanostructure of the surface is observed. The image is reproduced from Ref. [14].

The self-assembly of the organic molecules in solution occurs in the presence of inorganic precursors - e.g. silicilic acid $Si(OH)_4$ - which might also play an active role in the process, promoting and effecting self-assembly in the system [11]. The templating mechanism, therefore, allows one to replicate the structures of the biocomplex fluid into an organic/inorganic nanostructured biomineral composite.

The most basic understanding of these materials would involve separate studies of the organic phase in the absence of the inorganic one, and the nucleation and growth of the inorganic material in absence of the organic phase. However, a more appropriate study has to deal with both components which co-operate to form biominerals. In the case of diatoms, about 97 % of their skeletons consists of inorganic compounds (mostly silica) and the rest is attributed to organic molecules (mostly proteins). Recently, small polypeptides called "silaffins" have been found trapped in the diatom cell walls of the species *Cylindrotheca fusiformis* [15, 16] and are thought to be actively involved in the precipitation

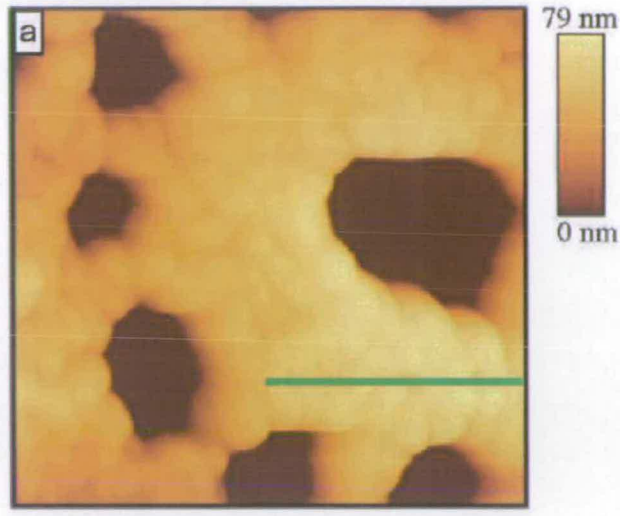

Figure 1.3: AFM image of the outer surface of a valve of diatom *C. granii*. The granular nanostructure of the surface is observed. The image is reproduced from Ref. [14].

The self-assembly of the organic molecules in solution occurs in the presence of inorganic precursors - e.g. silicilic acid $Si(OH)_4$ - which might also play an active role in the process, promoting and effecting self-assembly in the system [11]. The templating mechanism, therefore, allows one to replicate the structures of the biocomplex fluid into an organic/inorganic nanostructured biomineral composite.

The most basic understanding of these materials would involve separate studies of the organic phase in the absence of the inorganic one, and the nucleation and growth of the inorganic material in absence of the organic phase. However, a more appropriate study has to deal with both components which co-operate to form biominerals. In the case of diatoms, about 97 % of their skeletons consists of inorganic compounds (mostly silica) and the rest is attributed to organic molecules (mostly proteins). Recently, small polypeptides called "silaffins" have been found trapped in the diatom cell walls of the species *Cylindrotheca fusiformis* [15, 16] and are thought to be actively involved in the precipitation

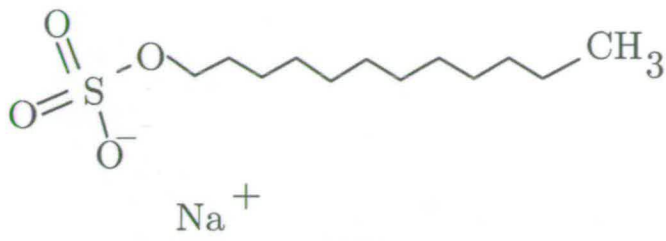

Figure 1.4: Anionic surfactant sodium dodecyl sulfate (SDS) [17].

of silica. In fact, experiments have shown that silaffins [15, 16], and some long-chain polyamines [2], produce networks of silica nanospheres (with diameters up to 100 nm) within seconds when added to a solution of silicilic acid, $Si(OH)_4$. These spheres have been also observed in microscopy experiments on diatoms and constitute their skeleton building blocks (Fig. 1.3). A possible mechanism which could explain the experimental observations is the templating mechanism. It is thought that silaffins and polyamines self-assemble in solution because of their amphiphilic properties to form aggregates which might constitute templates for the deposition of the inorganic material in the form of nanospheres [8]. This would be the reason why these macromolecules have been found harvested and trapped in diatom skeletons [15, 16]. These speculations are introduced, tested, and validated in Chapter 3 and Chapter 4.

Amphiphiles

Amphiphiles or surfactants are solute molecules which possess both hydrophilic and hydrophobic parts [17]. Because of the opposite affinity for the liquid, the two parts generally have a repulsive interaction with each other. Amphiphilic molecules tend to spontaneous formation of water-oil interfaces (the hydrophobic component being on the oil-rich part and the hydrophilic part being on the water-rich side of the interface) [18]. For this reason, these molecules are also called surfactants. An important property of surfactants is that they favour mixing of two immiscible liquids. In fact, amphiphiles that have a part which

is soluble only in the first liquid and the other part which is soluble only in the second liquid, will be at equilibrium at the interface between the two liquids. By adding an appropriate amount of surfactants to the mixture, the interface will eventually become bigger and bigger until any point in each fluid is only a microscopic distance from the interface. At this point, the immiscible fluids are in fact mixed.

For water solutions, the most common surfactants have ion pairs as their miscible parts. When put into water, these ions soon dissociate becoming strongly soluble. On the other hand, the immiscible parts are generally molecules with low polarity, such as hydrocarbon chains. Increasing the length of these chains makes these parts less and less miscible. If the polar head is positively charged, then the molecule is called a cationic surfactant. On the contrary, if the head is negatively charged, the amphiphile is called an anionic surfactant. One of the most common surfactants is SDS (sodium dodecyl sulfate) and can be found in many household cleaning products, such as soaps, detergents, and shampoo. A molecular structure of SDS is shown in Fig. 1.4.

Surfactants in solutions: micelles

If a small enough amount of surfactant is put into a liquid, the amphiphiles will disperse throughout it without interacting with each other. However, if we increase the concentration, a point comes where the dispersion no longer prevails over the surfactants' mutual interactions. At this point, the amphiphiles prefer to aggregate to reduce the surface of the insoluble part in contact with the fluid. The resulting aggregate structures are called micelles. Micelles typically form when the surfactant concentration is beyond a certain concentration called the critical micelle concentration (CMC). At these concentrations, the basic units of

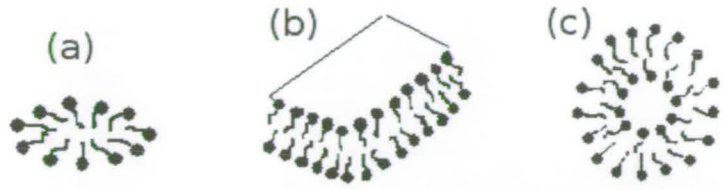

Figure 1.5: Three types of micelles: (a) Disc-like, (b) bilayer, and (c) spherical.

the fluid are no longer single surfactants but micelles. Micellisation is a process that occurs spontaneously as a result of the balance between entropy and enthalpy [17]. Micelles exist in various shapes, such as spherical, cylindrical, worm-like, and disk-like (Fig. 1.5) depending on the relative volumes of the hydrophobic and hydrophilic parts. They can also form various aggregates and phases, such as lamellar, cubic and bicontinuous. A review on amphiphilic systems and micelles is given in Ref. [17].

1.1.2 Role of phase separation in biomineralisation

On a larger lengthscale (tens of micrometres), self-assembled micelles and aggregates of micelles can be seen as organic-rich regions in a phase-separating complex solution of biomolecules (e.g. silaffins), water, and a silica precursor. Phase-separated structures, then, could act as templates for the subsequent precipitation of the inorganic material. Such a mechanism constitutes the base of recent theories, for instance, of pattern formation in diatoms. The phase-separation morphogenesis model of diatoms formulated by Sumper [16] a few years ago constitutes a landmark work on pattern formation in biominerals and on biomineralisation itself. In this model, phase-separated organic domains provide the silica with the necessary scaffolds for the subsequent precipitation and growth. This successful model has been for the first time tested by computer experiments and the results reported in Chapter 5.

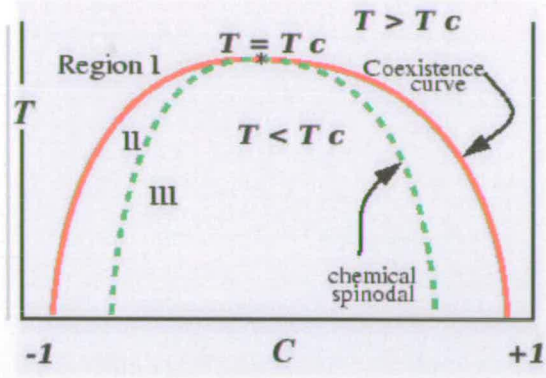

Figure 1.6: Phase diagram T vs C of a phase-separating binary mixture, where C is the system order parameter and T the temperature. Region I denotes the one-phase region in which the system is in at the onset. T_c is the critical temperature, the red line represents the coexistence curve, and the green dashed line the spinodal curve. Region II is the region delimited by the spinodal and coexistence curves and represents a metastable phase. Finally, region III denotes the spinodal phase in which the system ($C = 0$) will be after being quenched at temperature much lower than T_c. This phase is characterised by the patterns in Fig. 1.7.

Phase separation

A phase separation transforms a homogeneous system into two (or more) coexisting phases. In order to explain this phenomenon, let us consider the phase diagram of a model binary mixture in Fig. 1.6. At the onset, the binary mixture A-B is prepared such that is somewhere in region I of its phase diagram ($T > T_c$, where T_c is the critical temperature). If the concentration of component A (c_A) is higher than the concentration of component B (c_B) and the order parameter is defined as $C = c_A - c_B$, the system is in the right-hand part of the diagram. On the contrary, if component B prevails over component A, the system is in the left-hand side of the graph. Let us assume $c_A \gg c_B$. If the system is now quenched to a temperature not much below T_c, droplets of component B will start forming throughout the mixture triggering a nucleation process and pushing the system into region II. A similar scenario happens starting from the opposite configuration. A more interesting phenomenon happens if the system

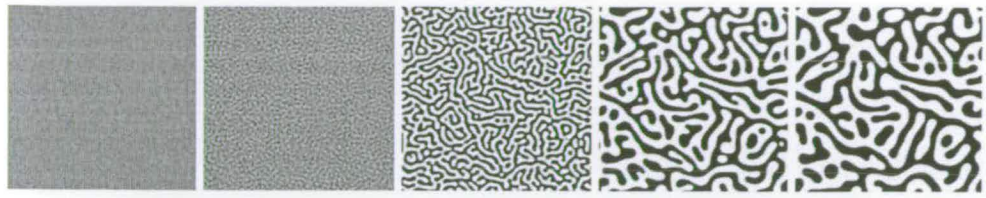

Figure 1.7: Computer simulation snapshots of spinodal decomposition. The simulation time increases from left to right.

is initially prepared in a configuration such that $C = 0$. Upon quenching at temperature much lower than T_c, the system is forced to start a spinodal decomposition into the two-phases. Spinodal decomposition is characterised by intricate and labyrinthine patterns (Fig. 1.7) typical of this phenomenon and has been extensively studied in the past years [19].

The possibility of controlling the shape of the resulting patterns by varying, for instance, the initial value of C, has given us the possibility of describing pattern formation in diatoms via phase separation. This problem will be discussed in detail in Chapter 5.

1.2 Critical phenomena

Matter at thermodynamic equilibrium exists in different states (liquid, solid ...). These states are defined by thermodynamics quantities (temperature, pressure, etc...) which fall within precise ranges depending on the material under examination. By varying one or more parameters, we can force the matter to leave the present state and assume a different one. The change of phase is called the *phase transition*.

Phase transitions can be classified into groups. The first attempt at classifying phase transitions was made by Ehrenfest who grouped them according to their degree of non-analycity. Under this scheme, phase transitions are labelled

by the lowest derivative of the free energy that is discontinuous at the transition. For instance, the various solid/liquid/gas transitions are classified as first-order transitions because they involve a discontinuous change in density which is the first derivative of the free energy $\mathcal{F}$ with respect to the chemical potential. Other examples include the discontinuity in the entropy $S = -\left(\frac{\partial \mathcal{F}}{\partial T}\right)_V$ and in the pressure $p = -\left(\frac{\partial \mathcal{F}}{\partial V}\right)_T$ in an experiment performed at constant temperature and volume. Similarly, second-order phase transitions have a discontinuity in a second derivative of the free energy, such as in the heat capacity $C_V \sim \left(\frac{\partial^2 \mathcal{F}}{\partial T^2}\right)$ [20, 21].

However, the Ehrenfest classification is inaccurate because it does not take into account the case where a derivative of free energy diverges (which is only possible at the thermodynamic limit). For instance, in the ferromagnetic transition (Section 6.4), the heat capacity diverges to infinity. A modern classification of phase transitions is therefore the following:

- First-order phase transitions are characterised by exchange of energy (latent heat) between the system and its environment and mixed-phase regimes (in which some parts of the system have completed the transition and others have not). Examples are the various solid/liquid/gas transitions;
- Second-order phase transitions are associated with continuum regimes and no latent heat, for example the ferromagnetic transitions.

In any system containing liquid and gaseous phases, there exists a special combination of pressure and temperature, known as the *critical point*, at which the transition between liquid and gas becomes a second-order transition. Near the critical point, the fluid is sufficiently hot and compressed that there is no distinction between the two phases [20]. In the binary-mixture phase diagram of Fig. 1.6, the critical point is located at the apex of the bell-shaped diagram.

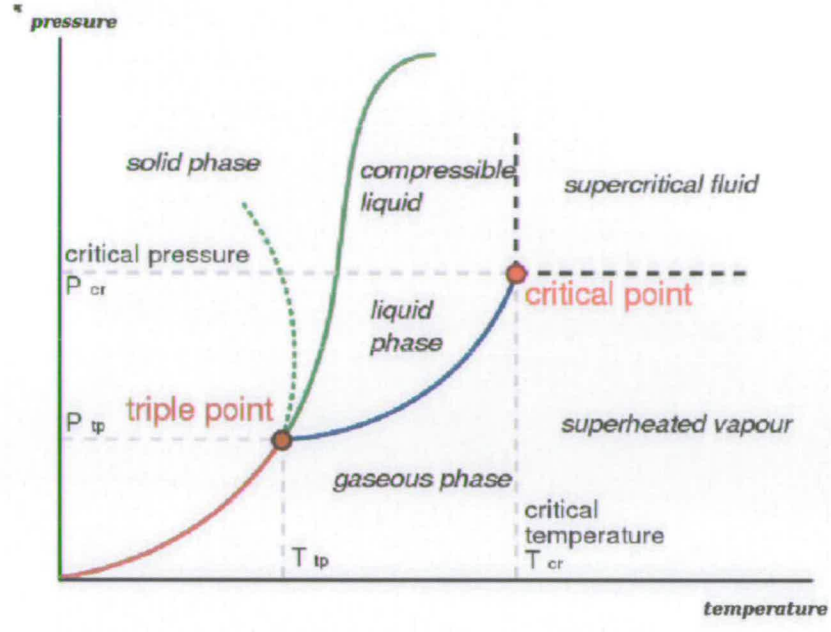

Figure 1.8: Typical pressure-temperature phase diagram. The dashed green line represents the anomalous behaviour of water. Image taken from [20].

Non-analytical properties of the system near the critical point are called *critical phenomena* [22] and will constitute the core of the second part of this work. In particular, we will be studying the still puzzling behaviour of the constant-volume heat capacity near the critical temperature in different statistical ensembles.

In second-order phase transitions, some observables (such as the heat capacity) might diverge. It is possible to show that a diverging observable (O) near the critical point behaves according to

$$\mathcal{O}(T) \sim (T - T_c)^{\alpha} \tag{1.1}$$

where α is called a *critical exponent*. Different observables exhibit different critical exponents, but different systems belonging to the same universality class have the same critical exponents (Section 6.2). A detailed review of critical phenomena is in Refs. [22, 23].

1.3 Computer simulations of self-assembly, phase separation, and critical phenomena in complex fluids

A better understanding of the physico-chemical processes implicated in biomineralisation (self-assembly of macromolecules on the nanometre scale and phase separation on the micrometre scale), and critical phenomena might be achieved by computer simulations. Computer simulations may serve as an auxiliary and complementary method of investigation to standard experiments, providing insights that these latter cannot provide. Furthermore, we can use computer simulations to validate experimental theories or test new ones [24]. For instance, in Chapter 5, we use computer simulations to test and validate a diatom morphogenesis model based on experimental observations.

The presence of different time and length scales in biomineralisation makes computer experiments more challenging and exciting. A different degree of detail is required to study different problems. This suggests that different approaches must be followed according to the accuracy and resolution we would like to achieve in our simulations. For example, in order to study biomineralisation at the molecular level, it will be inappropriate and unwise to carry out computer simulations with atomistic details. This, in fact, will make the simulations time consuming and full of irrelevant detail. Following this approach, we have used different computer simulations techniques throughout this thesis.

The simulation study of self-assembly of silaffins, or other biological amphiphiles, in aqueous solutions, for example, requires a certain degree of coarse graining. It is in fact not possible, at the present, to simulate bulk properties with atomistic detail in models of such complicated molecules. We instead seek "minimal" molecular models able to capture the essential characteristic of the system

we are going to study. These simple models, clearly, are experimentally motivated and/or constructed with the aid of calculations on single molecules.

In the case of the simulations of silaffins and simple diamines respectively reported in Chapter 3 and Chapter 4, we were interested in deriving theoretical models which could explain how they self-assemble in solution and favour the precipitation of silica in the form of nano-spheres. This was achieved by choosing a simulation technique which allowed one to comfortably simulate structures of the order of tens of nanometers. This goal was achieved by implementing a coarse-grained Brownian dynamics technique (see Section 2.5) on the model molecules. This technique was found to work reasonably well in this case allowing us to study and characterise the self-assembled structures on the nano-metre scale and compare our results to the experimental ones.

To study pattern formation by means of phase separation models (Chapter 5), or self-assembly on a larger scale, a higher degree of coarse graining was needed. To analyse structures of the order of tens of micrometres, molecular models are no longer efficient. Continuum simulations (Section 2.8), which implement continuum models, must be adopted. The amazing diatom structures described in Chapter 5 have been studied using this approach.

The possibility of understanding and biomimicking the processes involved in biomineralisation might allow the synthesis of mesoporous materials at ambient conditions with great control on the shape and the forms of the final product. The resulting material, then, could be used in a number of technological applications spanning from molecular sieving to catalysis.

Because of its potential technological applications, biomimetics has attracted a huge attention from scientists, for instance, trying to reproduce the highly ordered silica structures present in diatoms, starting from simple solutions of

biological macromolecules and silica precursors. However, although steps forward have been made, an exhaustive understanding of the mechanisms involved in biomineralisation has not been achieved yet.

Finally, the ensemble dependence of the constant-volume heat capacity near the critical point was studied using Monte Carlo techniques in which the sampling can be biased towards regions of specific interest of the phase diagram (in this case $T \simeq T_c$). Monte Carlo simulations contain no true dynamical information and are not constrained by natural timescales (as in MD or BD), and therefore constitute a powerful method for studying critical phenomena.

1.4 Summary and overview

This thesis is divided into two main parts. In the first part, we carry out computer simulations of self-assembly and phase separation in bio-complex fluids motivated by a desire to understand biomineralisation. In the second part, we focus on critical phenomena, in particular on the ensemble dependence of the constant-volume heat capacity near the critical point in order to understand its still puzzling behaviour.

This work is therefore organised as follows. In Chapter 3 we study the self-assembly of silaffins in aqueous solution. Silaffins self-assemble because of their amphiphilic properties forming arrays of micelles which constitute templates for the depositing silica. Silica nano-spheres would then fill the voids in between the micelles.

Chapter 4 reports an extensive study on the role played by simple diamines (putrescine homologues) in controlling the final shape of the siliceous products in biomineralisation. Here, we emphasise the importance of the hydrophobic properties of the diamine chains and their role in biomimetics.

Chapter 5 describes an experimentally motivated diatom morphogenesis model based on phase separation of mixtures of organic molecules (such as silaffins or polyamines) and water containing a silica precursor. The phase-separated organic structures can act as templates for the subsequent precipitation and deposition of silica.

Finally, Chapter 6 gives some insights on critical phenomena. We adopt a relatively new Monte Carlo sampling (based on the Wang-Landau [25] algorithm) to study the ensemble dependence of the constant-volume heat capacity of the three-dimensional Ising model near the critical point.

CHAPTER 2

Computer simulations

The study of condensed matter has a long and rich history from both the theoretical and experimental standpoints [24]. Experimentalists, have continuously worked to improve the understanding of the structure of the matter, for example by means of scattering experiments. At the same time, theoreticians have tried to construct simple models of matter which explain how it behaves. Theories, then, can be tested by comparing their predictions with experimental results. However, a discrepancy could either mean that the theory is inaccurate or the model is not an adequate description of the real system.

The introduction of computers in science has then provided an alternative mode of research in condensed-matter physics. Computer simulations can be used as a linking bridge between theory and experiments. Computer experiments provide results against which theories can be tested. Furthermore they can aid in interpreting experimental results, and sometimes in devising new experimental strategies.

2.1 Motivations and applications

Statistical mechanics is the discipline that connects the microscopic variables (positions and momenta) of a physical system to its macroscopic ones (temperature, pressure, etc.). Many simple problems in statistical mechanics are exactly solvable but only a handful of non-trivial problems can actually be solved exactly. A typical example of a complex solvable system is the two-dimensional Ising model [24, 26].

Other problems can be tackled by using successive approximation algorithms, and perturbative expansions; computers play an important role in such work, for instance in calculating virial coefficients, Feynman diagrams, graphs, and so on [24, 27].

The study of phase transitions, for example, is nowadays characterised by a combination of exact solutions (obtained by means of theories such as mean field theory), theoretical approaches, and numerical ones. Computer simulations have now joined these methods as an effective tool to better understand Nature. There are, in fact, physical systems that can only be understood by using models which are unsolvable by current analytic methods and for which computer simulations can provide the only answers [28].

As well as being of academic interest, the information obtained by computer simulations is extremely useful in cases where it may be difficult or impossible to carry out real experiments. For example, while experiments under extreme conditions might be quite difficult to perform, to simulate a system under extreme conditions is perfectly feasible [24, 29].

Computer simulation techniques are generally categorised according to the phenomena they will have to deal with. The choice of the simulation strategy to be used to tackle a particular problem relies on the characteristic length and

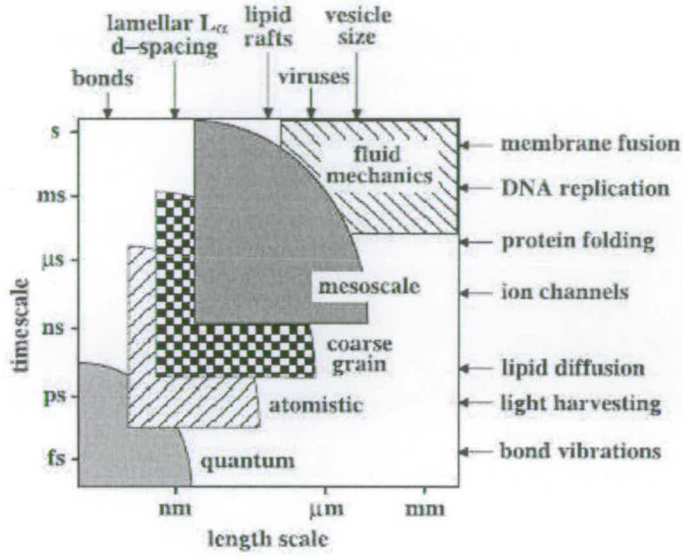

Figure 2.1: Schematic diagram of spatial and temporal phenomena scales accessible by different simulation techniques. Some characteristic structures and events are also reported. Figure reproduced from [30].

time scales of the complex system to be studied. The diagram in Fig.2.1 shows how different techniques are used for different problems, each of them characterised by different length and time scales. The specific computer simulation techniques used in this work will be discussed in Sections 2.4-2.8.

2.2 General aspects of molecular simulations

Computer simulations in condensed-matter physics are often employed to calculate the thermodynamic and structural properties of the system under investigation, starting from its microscopic details. The system is represented by interacting "particles" or "beads" each modelling single atoms, molecules, or groups of molecules according to the degree of "coarse-graining" adopted in the simulation approach.

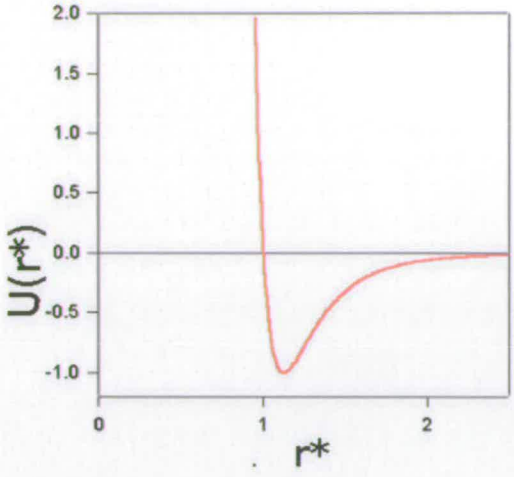

Figure 2.2: Schematic representation of a Lennard-Jones potential.

Each pair of particles interacts according to "simple" interatomic potentials, which are generally assumed to be spherically symmetric and pairwise additive. These potentials are to be regarded as *effective* pair potentials that take into account also the contribution from many-body forces [21]. The total potential energy is therefore the sum of all the pair contributions for all pairs of particles, i.e.

$$u = \sum_{i<j} u_{ij} \tag{2.1}$$

where u_{ij} is the contribution from particles i and j.

2.2.1 *Interaction potentials*

One of the most used potentials is the Lennard-Jones $12-6$ potential,

$$u(r) = 4\epsilon \left[\left(\frac{\sigma}{r}\right)^{12} - \left(\frac{\sigma}{r}\right)^{6} \right] \tag{2.2}$$

where r is the distance between the two particles, σ is the particle diameter (usually representing the basic unit of length in the simulations) and ϵ is the potential well depth. This potential is made up of two contributions, a repulsive one with $1/r^{12}$ dependence, describing the strong repulsion between very

close particles (which has its origin in the overlap of the outer electron shells), and an always-attractive one, with $-1/r^6$ dependence which also accounts for van der Waals interactions at large distances. Atomic liquids such as argon are well described by the Lennard-Jones potential [24, 27].

The Lennard-Jones potential is often cut-and-shifted at a certain distance r_{cut} beyond which any interaction is considered negligible. This latter operation reduces drastically the time to compute the sums in Eq. (2.1) without altering the final result. The shift, instead, is made to avoid using a discontinuous potential (hence an undefined force, $\mathbf{F} = -\nabla u$) at the distance where the potential was cut. A cut-and-shifted potential speed up the simulation reducing the time necessary to calculate the total energy and the force acting on each particle.

Another widely used potential is the so-called hard-sphere potential. This describes the particles of the system as impenetrable spheres of diameter σ, namely

$$u(r) = \begin{cases} \infty & r \leq \sigma \\ 0 & r > \sigma. \end{cases} \tag{2.3}$$

2.2.2 *Periodic boundary conditions*

Computer simulations are generally carried out on small systems for many reasons. For instance they are computationally less expensive and do not require huge amount of storage space in the computer. On the other hand, computer simulations of small systems are not satisfactory when studying bulk properties. In fact, in a small system of N particles almost half of them will be too close to the simulation cell surfaces, experiencing quite different forces from the rest of the particles in the bulk, and leading to imprecise results.

To overcome this problem, periodic boundary conditions (PBC) can be implemented throughout the system. The simulation box is replicated infinite times

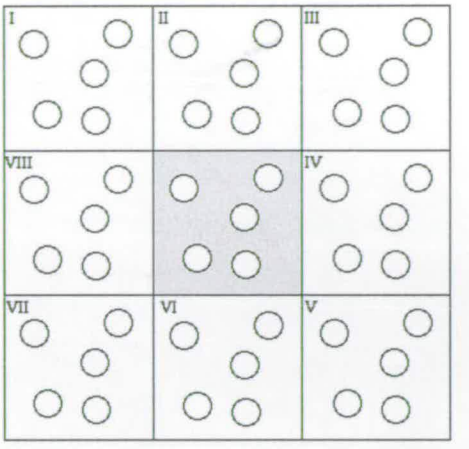

Figure 2.3: Boundary conditions in a two-dimensional periodic system. Molecules can enter or leave each cell across each of the four edges [31].

throughout the space in order to mimic a bulk system. During the simulation, as the particles in the central cell move around, their image-particles will do the same in each of the neighbouring cells. So if a particle leaves the central cell a new one coming from a neighbouring cell will enter the main cell keeping the number of particles in it constant.

In principle, all of the particles in all of the cell replicas will interact with each other, making the simulations very time consuming. To make the calculations tractable the minimum image convention is used: particles are allowed to interact only with the nearest periodic images of the other $N - 1$ particles.

2.2.3 Reduced units

Computer simulations are often carried out in reduced units. These units are conveniently defined for two main reasons. The most important one is that many different states in real units correspond only to a single state in reduced units. This means that reduced units avoid the repetition of the simulation for each of these states. The second reason is that an appropriate choice of reduced units will make all simulation parameters and results of the order of unity, and

Quantity	Reduced units
Distance	$r^* = r/\sigma$
Density	$\rho^* = (N/V)\,\sigma^3$
Energy	$U^* = U/\epsilon$
Temperature	$T^* = k_B T/\epsilon$
Pressure	$P^* = P\sigma^3/\epsilon$
Time	$t^* = \sqrt{\epsilon/m\sigma^2}t$

Table 2.1: Reduced units for computer simulations of Lennard-Jones liquids. k_B denotes the Boltzmann constant and m the mass of the particles. This latter quantity is usually set equal to 1, that is as a fundamental unit in the simulations.

also simplify the mathematical expression of the potentials. This latter would increase the numerical precision in the simulation results. In the example of the Lennard-Jones pair potential (2.2), an appropriate choice of reduced units is given in Tab. 2.1. The Lennard-Jones potential (2.2) in this case can be rewritten as

$$u^*(r^*) = 4\left[\left(\frac{1}{r^*}\right)^{12} - \left(\frac{1}{r^*}\right)^{6}\right]. \tag{2.4}$$

2.2.4 *Coarse-grained techniques*

Coarse-grained techniques are mainly used to study physical phenomena which occur at characteristic length and time scales of the order of hundreds of nanometers and tens of nanoseconds, respectively (Fig. 2.1). Throughout this thesis, the term "coarse-grained" will indicate that the interacting particles of our simulations represent groups of atoms or molecules rather than single atoms. These particles will interact via appropriate effective potentials.

2.3 Ensembles and averages in statistical mechanics

Statistical mechanics is a probability theory which provides mathematical tools for dealing with systems of many particles. Statistical mechanics is able to

predict macroscopic properties (for instance, pressure and temperature) of a many-body system from its microscopic properties (such as positions and velocities) [21, 32].

2.3.1 Ensembles

Statistical mechanics groups many-body systems into *ensembles*. A statistical-mechanical ensemble consists of a very large (theoretically infinite) number of copies of a system, all characterised by the same macroscopic variables [21, 32].

A *micro-canonical* ensemble is a group of systems characterised by the same number of particles N, the same energy E, and the same volume V. This ensemble is often denoted as NVE ensemble and consists of copies of an isolated system.

A *canonical* ensemble consists of many-body systems of equal number of particles N, of same volume V and at thermal equilibrium with a heat bath at temperature T. This ensemble exchanges energy with the heat bath and is also denoted as NVT ensemble.

A *grand-canonical* ensemble is a collection of identical systems at equilibrium with an external reservoir with which they exchange both energy and particles. This ensemble is often referred as μVT, where μ denotes the chemical potential which controls the fluctuations in the number of particles.

In the *Isothermal-isobaric ensemble*, all the systems have the same number of particles N and maintain the same temperature T and pressure P. This ensemble is also denoted as NPT-ensemble and plays a very important role in chemistry as many chemical reactions are carried out under constant temperature and pressure conditions.

2.3.2 *Time averages and ensembles averages*

The microscopic states (positions $\mathbf{r}$ and momenta $\mathbf{p}$) of a many-particle system can be represented in *phase space*. In the case of a three-dimensional system of N particles, the values assumed by the variables $\mathbf{r}^N$ and $\mathbf{p}^N$ at any time define a point in the $6N$-dimensional phase space. A set of points in phase space defines a trajectory.

If $\mathcal{A}(\mathbf{r}^N, \mathbf{p}^N)$ is a function of the $6N$ coordinates and momenta, its time average over a period τ is defined as

$$\langle \mathcal{A} \rangle_t = \lim_{\tau \to \infty} \frac{1}{\tau} \int_0^\tau [\mathcal{A}(\mathbf{r}^N, \mathbf{p}^N)] dt. \tag{2.5}$$

A different averaging procedure based on the concept of ensemble can also be introduced. To do so, we denote with $f^{(N)}(\mathbf{r}^N, \mathbf{p}^N, t)$ the *probability density*. This function describes the distribution in phase space at the time t of the phase points relative to a certain statistical-mechanical ensemble. Under equilibrium conditions, f is independent of time and ensemble averages can be defined as follows

$$\langle \mathcal{A} \rangle_e = \int \int \mathcal{A}(\mathbf{r}^N, \mathbf{p}^N)\ f(\mathbf{r}^N, \mathbf{p}^N) d\mathbf{r}^N d\mathbf{p}^N. \tag{2.6}$$

If the average in Eq. (2.5) is performed over a long time, and the system eventually flows through all its possible microstates, then ensemble averages become the same as time averages, that is

$$\langle \mathcal{A} \rangle_t = \langle \mathcal{A} \rangle_e. \tag{2.7}$$

This equivalence is known as the *ergodic* theorem and it is believed to hold for all many-body systems present in Nature [32].

2.4 Molecular Dynamics

Molecular dynamics (MD) simulation is a classical technique to compute equilibrium and transport properties of a many-body system.

In this technique each particle moves according to Newton's laws of motion, which are integrated numerically. The positions and the velocities of the particles are updated every time-step and the equations of motion integrated to generate a trajectory in phase space. This procedure is repeated for a number of time-steps required to equilibrate the system and calculate accurate time averages.

A typical MD simulation will proceed as follows: positions $\mathbf{r}$ and velocities $\mathbf{v}$ of the particles at time t are stored in the computer. The force acting on each particle is then calculated from the potentials ($\mathbf{F}_i = -\nabla_i u$) and the equation of motion $\mathbf{F}_i = m_i \mathbf{a}_i$ integrated over a finite time-step Δt according, for instance, to the Verlet algorithm to get the position of the particles a short time later $t + \Delta t$ [24, 27]

$$\mathbf{r}_i(t + \Delta t) = 2\mathbf{r}_i(t) - \mathbf{r}_i(t - \Delta t) + \mathbf{a}_i(t)\Delta t^2. \tag{2.8}$$

The velocities can be calculated separately from the positions using

$$\mathbf{v}_i(t) = \frac{\mathbf{r}_i(t + \Delta t) - \mathbf{r}_i(t - \Delta t)}{2\Delta t}. \tag{2.9}$$

The numerical integration of the equations of motion using the Verlet algorithm generates errors of the order of Δt^4 in the positions and Δt^2 in the velocities [24, 27].

A better integration algorithm is the so-called "velocity-Verlet", which is

$$\mathbf{r}_i(t + \Delta t) = \mathbf{r}_i(t) + \mathbf{v}_i(t)\Delta t + \frac{1}{2}\mathbf{a}_i(t)\Delta t^2 \tag{2.10}$$

$$\mathbf{v}_i(t + \Delta t) = \mathbf{v}_i(t) + \frac{1}{2}\Delta t \left[\mathbf{a}_i(t) + \mathbf{a}_i(t + \Delta t)\right]. \tag{2.11}$$

The implementation of this algorithm is as follows. The new positions at time $t + \Delta t$ are calculated using Eq. (2.10) and the velocities updated to half-step according to

$$\mathbf{v}_i(t + \Delta t) = \mathbf{v}_i(t) + \frac{1}{2}\Delta t\, \mathbf{a}_i(t). \tag{2.12}$$

Then, the forces and accelerations at time $t + \Delta t$ can be calculated from the positions, $\mathbf{r}(t + \Delta t)$, and the velocities advanced half-step using

$$\mathbf{v}_i(t + \Delta t) = \mathbf{v}_i(t + \frac{1}{2}\Delta t) + \frac{1}{2}\Delta t\, \mathbf{a}_i(t + \Delta t). \tag{2.13}$$

In a standard MD simulation total energy and momentum are conserved quantities. In the statistical-mechanical jargon, an MD program simulates a micro-canonical ensemble (constant NVE). Molecular dynamics simulations can also be performed in constant-temperature ensembles, such as NVT (also called canonical ensemble), and NPT (where P is the system pressure). In these cases the temperature T is kept constant by coupling the system to a heat bath. A detailed review of constant-temperature MD methods is given in Refs. [24] and [27].

2.5 Brownian Dynamics

An alternative simulation technique that keeps the system temperature constant is Brownian dynamics (BD).

In the presence of large time-scale separations between the rapid motion of the solvent and the slower motion of the solute, such as in the case of polymer, amphiphile and colloidal suspensions, the simulation time can become prohibitively long. In fact, the short time steps needed to capture the fast motion of the solvent, and the long runs needed to study the structural evolution of the solute, can make the simulations very time consuming and irritating, especially in those cases in which the fast (solvent) modes are not of interest. BD is a mesoscale simulation technique in which explicit solvent particles are replaced by stochastic and frictional forces.

At the very core of this technique there is the integration of the Langevin equation in order to generate trajectories of the solute particles in which we are interested, by letting friction and random terms mimic the solvent. The Langevin equation in this situation is written

$$\mathbf{F}_i = -\nabla_i u - m\xi\dot{\mathbf{r}}_i + \mathbf{R}_i \tag{2.14}$$

where $\mathbf{r}_i$ is the position vector of particle i, u is the potential energy (given by an appropriate sum over pairs of particles), ξ is the friction coefficient, and $\mathbf{R}_i$ is a random force, representing the effect of the solvent. The random force is typically Gaussian white noise and obeys the fluctuation-dissipation theorem

$$\begin{aligned} \langle \mathbf{R}_i(t) \rangle &= 0 \\ \langle \mathbf{R}_i(t) \cdot \mathbf{R}_j(t') \rangle &= 6mk_{\mathrm{B}}T\xi\delta_{ij}\delta(t-t'). \end{aligned} \tag{2.15}$$

The Langevin equation (2.14) can be integrated numerically, for example using a Verlet-like algorithm [24]. The friction coefficient ξ is related to the diffusion

coefficient D accordingly to Einstein's equation

$$\xi = \frac{k_B T}{mD} \tag{2.16}$$

where k_B is Boltzmann's constant and m is the mass of the diffusing particle.

Hydrodynamic effects, that is the influence of one particle on another through the flow of the solvent around them, and the interaction between two particles due to solvent structure, can also be included in this simulation scheme. Details are in Ref. [24].

2.6 Monte Carlo

Monte Carlo methods aim to generate trajectories in the configuration space which sample from a chosen statistical-mechanical ensemble. The ensemble average of a certain quantity $\mathcal{A}$ is then calculated via

$$\langle \mathcal{A} \rangle = \frac{1}{Q} \sum_i \mathcal{A}_i \exp\left(-\beta E_i\right), \tag{2.17}$$

where $Q = \sum_i \exp\left(-\beta E_i\right)$ is the partition function, $\beta = 1/k_B T$ and $\exp\left(-\beta E_i\right)$ is the Boltzmann factor which weights every accessible state i of energy E_i. However, the number of accessible states in a very large system can be huge making the exact evaluation of the average (2.17) unfeasible with current computers [21]. Moreover, certain states (those with small Boltzmann factor, e.g. due to particle overlap) contribute very little to the average, slowing down the simulation. To overcome these problems, what is used is the so-called importance-sampling Monte Carlo. In this scheme the only configurations to be sampled are those that make a significant contribution to the partition function and ensembles averages. This task is achieved generating a *Markov* chain of configurations in which each state is generated by "perturbing" the preceding

one in the chain, and accepted as a new configuration only if the *detailed-balance* condition is satisfied [21, 24, 27].

A sufficient (but not necessary) detailed-balance condition is that for all new states denoted n

$$J(o \rightarrow n) = J(n \rightarrow o) \tag{2.18}$$

where $J(o \rightarrow n)$ is the probability flux from a state o to a "new" state n during a given time step. The flux $J(o \rightarrow n)$ can be factored into three terms

$$J(o \rightarrow n) = p(o) \cdot \alpha(o \rightarrow n) \cdot acc(o \rightarrow n) \tag{2.19}$$

where $p(o)$ is the probability of being in state o (at equilibrium should follow the Boltzmann distribution), $\alpha(o \rightarrow n)$ is the probability of generating the trial move from o to n, and $acc(o \rightarrow n)$ is the probability of accepting the trial move from o to n. By combining Eqs. (2.18) and (2.19), the detailed-balance condition can be rewritten as

$$\frac{acc(o \rightarrow n)}{acc(n \rightarrow o)} = \frac{\alpha(n \rightarrow o)}{\alpha(o \rightarrow n)} \cdot e^{-\beta[E(n)-E(o)]} \tag{2.20}$$

where $E(n)$ and $E(o)$ are the system energies after the move and before the move. If $\alpha(o \rightarrow n) = \alpha(n \rightarrow o)$, the solution to Eq. (2.20) is

$$acc(o \rightarrow n) = \min\left(1, e^{-\beta[E(n)-E(o)]}\right). \tag{2.21}$$

A typical importance-sampling Monte Carlo scheme to perform a simulation in the canonical (NVT) ensemble will proceed as follows. The system is prepared in some initial configuration. A particle is chosen randomly and displaced within the simulation cell. If the trial move results in a decrease of system energy, then the move is accepted and the particle positions updated. If

the trial move results in an increase of energy, instead, the move is accepted with probability $\exp(-\beta\Delta E)$, where ΔE is the difference in system energy associated to the trial move. This is implemented in a computer experiment by generating a random number (from here the name Monte Carlo) in the interval $(0, 1)$ and accepting the move only if the random number is less than the value $\exp(-\beta\Delta E)$. These steps are repeated for the next randomly selected particle. After a large number of trial moves, simple unweighted averages over the visited states can be calculated since each state is sampled with a probability proportional to its Boltzmann factor [21, 24].

2.7 Measurable quantities

As in real experiments, during our simulations, we make measurements of certain physical quantities. This is achieved by estimating ensemble averages in MC methods or time averages in MD/BD methods. Ensemble averages and time averages should converge to the same numbers if the simulations are long enough to fulfill the ergodicity theorem (2.7). Some examples of measurable quantities from computer simulations are given below.

2.7.1 Structure: radial distribution function and structure factor

A simple quantity which characterises the structure of a fluid is the pair distribution function $g_2(\mathbf{r}_1, \mathbf{r}_2)$, or in an isotropic, homogeneous fluid, the radial distribution function $g(r)$. This latter measures the probability of finding any pair of particles separated by a distance r. These quantities are usually compared with the corresponding distributions for an ideal gas at the same density.

If the particles are uncorrelated (i.e., the fluid is unstructured), then the expected pair distribution function is [32]

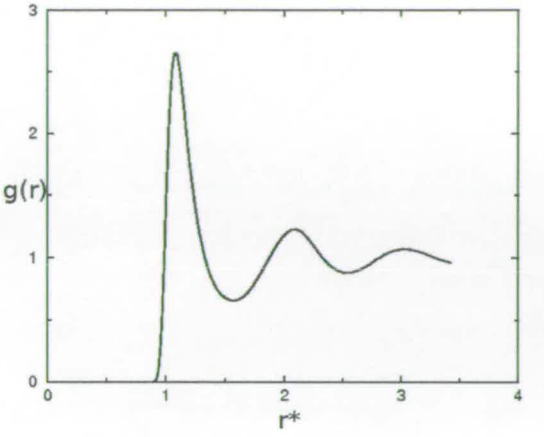

Figure 2.4: Pictorial representation of $g(r)$ for a Lennard-Jones liquid at density $\rho^* = 0.8$ and $T^* = 1$. Image reproduced from Ref. [31].

$$g_2(\mathbf{r}_i, \mathbf{r}_j) = \left(1 - \frac{1}{N}\right) \simeq 1 \tag{2.22}$$

provided the number of particles N is large enough.

A typical $g(r)$ for a Lennard-Jones liquid is shown in Fig. 2.4. The peaks result from the co-ordination shells around a given particle and $g(r)$ typically decays to 1 as $r \to \infty$, because the correlations between the positions of the particles vanish. The liquid, in this case, is said to have short-range order.

The radial distribution function $g(r)$ is important for different reasons. For instance, it can be measured experimentally, using neutron-scattering techniques so that it provides a link between computer simulations and real experiments. Moreover, for pairwise additive potentials, knowledge of the $g(r)$ is sufficient to calculate thermodynamic properties, particularly the system energy, pressure, and compressibility [24].

The static structure factor, $S(q)$, measures fluctuations in the fluid density, and is accessible through scattering experiments [23]. $S(q)$ can be calculated as a

Fourier transform of the radial distribution function $g(r)$,

$$S(q) = 1 + \rho \int [g(\mathbf{r}) - 1] e^{-i\mathbf{q}\cdot\mathbf{r}} d\mathbf{r} \tag{2.23}$$

where q is a wave-vector and ρ is the average density. Alternatively, $S(q)$ can be calculated directly as an autocorrelation function of the Fourier components of the instantaneous local particle density, $\rho(\mathbf{r}) = \sum_{j=1}^{N} \delta(\mathbf{r} - \mathbf{r}_j)$, i.e.,

$$S(\mathbf{q}) = \frac{1}{N} \langle \rho_{\mathbf{q}} \rho_{-\mathbf{q}} \rangle \tag{2.24}$$

where

$$\rho_{\mathbf{q}} = \int \exp(-i\mathbf{q} \cdot \mathbf{r}) \rho(\mathbf{r}) d\mathbf{r} = \sum_{j=1}^{N} \exp(-i\mathbf{q} \cdot \mathbf{r}_j) \tag{2.25}$$

are the Fourier components.

2.7.2 *Diffusion*

The mean square displacement measures the diffusion of the particles in the fluid. It is defined as [24]

$$\Delta R^2(t) = \langle |\mathbf{r}_i(t) - \mathbf{r}_i(0)|^2 \rangle \tag{2.26}$$

where $\mathbf{r}_i(t)$ is the position of particle i at time t, and it is averaged over the number of particles and the number of time origins. At short times t, the particles have not collided yet with their neighbours, and move with constant velocities; the resulting motion is called "ballistic" and is characterised by $\Delta R^2 \propto t^2$. At longer times, the particles start colliding with each other and the system is said to be in the "diffusive" regime characterised by Brownian motion and the Einstein relation [24]

$$\Delta R^2 = 2dDt \tag{2.27}$$

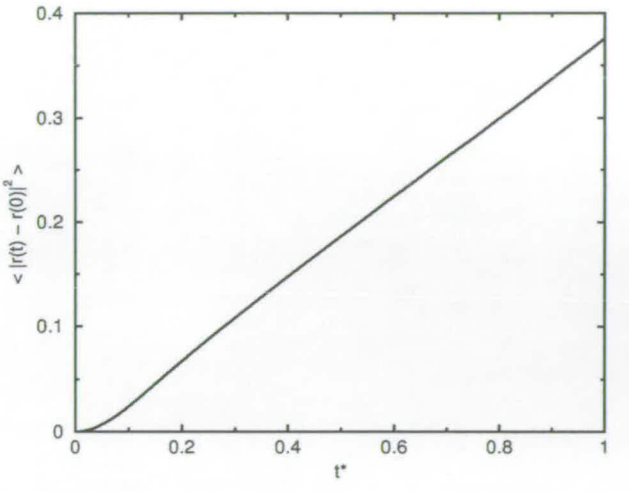

Figure 2.5: Mean square displacement for a Lennard-Jones liquid at density $\rho^* = 0.8$ and temperature $T^* = 1$. Image reproduced from Ref. [31].

where D is the diffusion coefficient and d the dimension of the system. D can therefore be easily estimated from the slope of the mean square displacement. We note that in Brownian dynamic computer simulations the crossover from the ballistic regime to the diffusive one is also observed in the case of a simulation performed on a single particle. A typical mean square displacement for a Lennard-Jones liquid is in Fig. 2.5.

An alternative way to estimate the diffusion coefficient is by the Green-Kubo relations [24, 27]. The Green-Kubo formulae give exact mathematical expressions for transport coefficients in terms of integrals of time correlation functions (linear response theory). In this case, D is calculated by integrating the velocity autocorrelation function, namely

$$D = \frac{1}{d} \int_0^\infty \langle \mathbf{v}(t) \cdot \mathbf{v}(0) \rangle. \tag{2.28}$$

The time autocorrelation functions will be described in the next section.

2.7.3 *Time correlation functions*

Time correlation functions are very important in computer simulations for the following reasons [24]:

- they describe the dynamics of the fluid;
- they are related to macroscopic transport coefficients via the Green-Kubo formulae;
- their Fourier transforms can be related to experimental spectra (dynamic light scattering).

The time correlation function of two quantities $\mathcal{A}(t)$ and $\mathcal{B}(t)$ is defined as

$$C_{\mathcal{AB}}(t) = \langle \mathcal{A}(t)\mathcal{B}(0) \rangle \tag{2.29}$$

whereas the autocorrelation function is

$$C_{\mathcal{AA}}(t) = \langle \mathcal{A}(t)\mathcal{A}(0) \rangle. \tag{2.30}$$

An example of the velocity time autocorrelation function for a Lennard-Jones system is shown in Fig. 2.6. At $t = 0$, $C_{\mathcal{AA}}(0) = \langle \mathcal{A}^2 \rangle$. As the time goes on, the time autocorrelation function decays approximately exponentially until it reaches a negative value denoting the presence of particles which have reversed their velocities after collisions. At longer time, the particles eventually forget about their past and $\mathcal{A}(t \to \infty)$ becomes uncorrelated with $\mathcal{A}(0)$. In other words, $C_{\mathcal{AA}} \simeq \langle \mathcal{A}(t) \rangle \langle \mathcal{A}(0) \rangle \simeq 0$, assuming $\langle \mathcal{A}(t) \rangle = 0$.

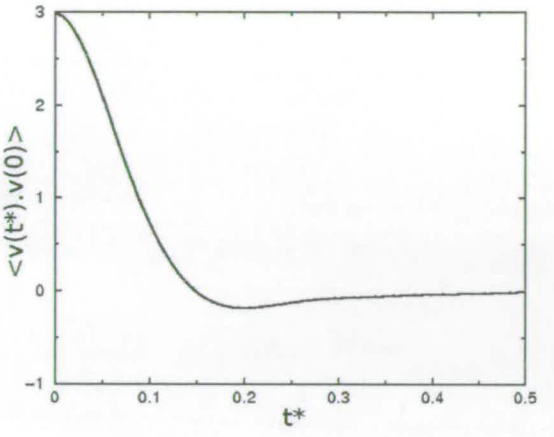

Figure 2.6: Velocity autocorrelation function for a Lennard-Jones liquid at density $\rho^* = 0.8$ and temperature $T^* = 1$. Image reproduced from Ref. [31].

2.8 Continuum methods

So far, the basic units in our simulations were particles. In continuum methods, the fluid is represented by a continuous medium, fully described by its free-energy functional[1] or Hamiltonian $\mathcal{H}[\psi(\mathbf{r}, t)]$, where $\psi(\mathbf{r}, t)$ is an appropriate order parameter that depends on the position $\mathbf{r}$ and time t.

Continuum computer simulations are adopted in all cases where a very high degree of coarse graining is required to investigate, for instance, the microstructures produced by phase-separating microemulsions or some interesting hydrodynamic problems. Microemulsions are mixtures of oil, water and surfactants, and they often exhibit interesting microstructures and dynamics that occur on lengthscales and timescales unattainable in molecular simulations.

The structure and dynamics of microemulsions can be studied using a time dependent Ginzburg-Landau model [23, 33]. A typical simulation to implement this model would follow these steps. An appropriate order parameter ψ which depends on the position $\mathbf{r}$ and time t is chosen to represent the system under

[1] A functional is a function that takes a function as its argument and returns a real number.

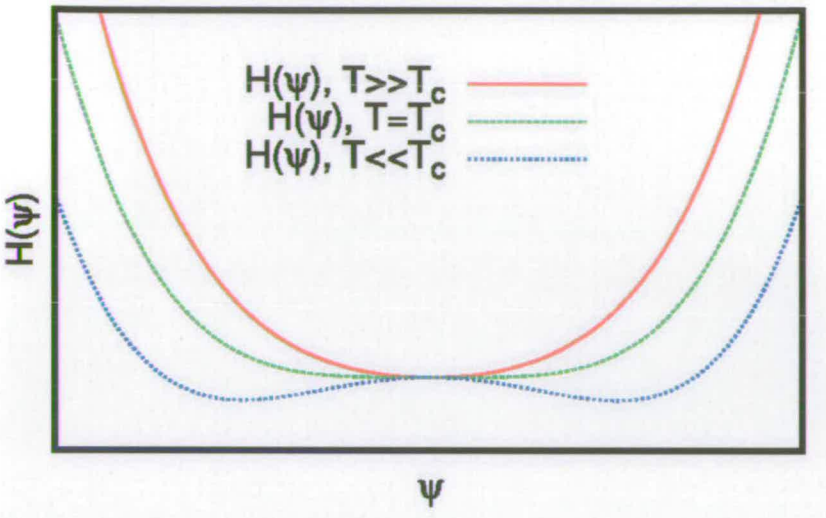

Figure 2.7: Qualitative representation of a Landau free-energy for a binary mixture: at temperature T much higher than the critical temperature T_c, the fluid components are randomly mixed; if the mixture is cooled down at a temperature much lower than the critical temperature T_c, the fluid phase-separate into its two components, each of them represented by the well in the graph.

investigation. The free energy of the system is written down as a function of the order parameter, for example

$$\mathcal{H}[\psi(\mathbf{r},t)] = \int d\mathbf{r}[f(\psi) + (\nabla^2\psi)] \tag{2.31}$$

where the term f represents the "bulk" Landau-type free energy and the term $(\nabla^2\psi)$ the leading-order term in a functional expansion of the interfacial free energy as derived by Cahn and Hilliard [34]. In the Landau theory of phase transitions, assuming that the order parameter is small and uniform near the critical temperature T_c, the free energy f is written as a functional expansion in the form [23, 33]

$$f(\psi) = a(T - T_c)\psi^2 + b\psi^4 \tag{2.32}$$

where $a > 0$ and $b > 0$ are system-specific constants. The free energy (2.32) has a double-well shape as shown in Fig. 2.7. The time evolution of the order parameter ψ is then followed by integrating numerically a typical continuity

equation (as derived in Chapter 5), such as

$$\frac{\partial \psi}{\partial t} = M\nabla^2 \frac{\delta \mathcal{H}}{\delta \psi} + \eta(\mathbf{r}, t) \tag{2.33}$$

where M is the mobility of the fluid components, and η is a thermal noise which satisfies the fluctuation-dissipation theorem (2.15). ψ is thereby calculated at every time step and average quantities estimated during the simulation.

2.9 Summary

In this chapter, we have briefly introduced computer simulations, described their importance in science, and indicated how the results can be compared to those from real experiments. We have also outlined different computer simulation techniques according to the degree of coarse graining required to represent the most relevant length and time scales in the system under investigation. We reported a number of physical quantities which can be estimated directly via computer experiments, their meaning, and how to relate them to real experimental outcomes.

Details of specific techniques/applications are contained within the relevant chapters.

CHAPTER 3

Self-assembly of Silaffins in biosilica formation

3.1 Introduction

One of the objectives of material science is to devise methods for the controlled fabrication of complex structures from inorganic materials. As well as of being of huge inherent interest, the ability to reproduce complex architectures on the nanoscale allows the fabrication of devices for nanotechnological applications, such as molecular sieving. In developing appropriate synthetic strategies, it is becoming commonplace to look for inspiration from Nature and how she controls biomineralisation. Interestingly, biominerals often possess ordered inorganic structures, even though the inorganic material itself is often amorphous and unable to form interesting architectures. In the case of diatoms, for instance, silica (SiO_2) is the prevalent amorphous inorganic component of their skeletons, which often are fashioned with symmetric arrays of pores or other complex architectures as shown in Figs. 3.1 (c) and 5.1. We recall that the morphogenesis of these biominerals is different from the morphogenesis of crystalline materials such as calcium carbonate ($CaCO_3$). Calcium carbonate is gen-

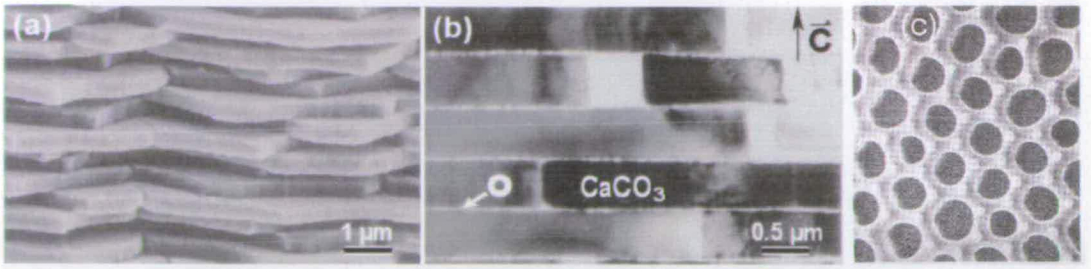

Figure 3.1: (a) SEM image of an abalone shell showing $CaCO_3$ platelets $\sim 0.5\mu$m thick. (b) TEM image of the cross-section of an abalone shell revealing the thin (< 10 nm) organic "marble" between the platelets. (c) Microscopy image of a portion of a diatom silica shell. Images (a) and (b) are reproduced from Ref. [11], whereas image (c) is from Ref. [3].

erally transformed by Nature into more complex structures such as spicules and shells. Abalone shells consist of layers of thick ($\sim$ 200 nm) platelets of $CaCO_3$ held together by a thin layers (< 10 nm) of polymer "cement" [Figs. 3.1 (a) and (b)]. The shell of the abalone is known for being exceptionally strong and can be employed in constructions [11].

At this stage in the study of biomineralisation at the molecular scale, we will focus on some specific cases before trying to find connections between seemingly disparate systems. We will consider some particular diatom species and in particular we will report some exciting experiments on diatoms that have advanced the understanding of biomineralisation in the past decade. Diatom cell walls (frustules) often exhibit complex porous structures on the 10 nm to 10 μm lengthscale, made from composites of silica and organic macromolecules. Recent atomic force and scanning electron microscope experiments of diatom frustules show that their fundamental building blocks are tightly packed siliceous spheres (Fig. 3.2) of diameter in the region $10-100$ nm [14, 35–38]. In this chapter, we will devise a physico-chemical model able to rationalise the presence of these elementary building blocks.

In a series of experiments, Sumper and co-workers have analysed the detailed structure and composition of biosilica extracted from a variety of diatom species [14,

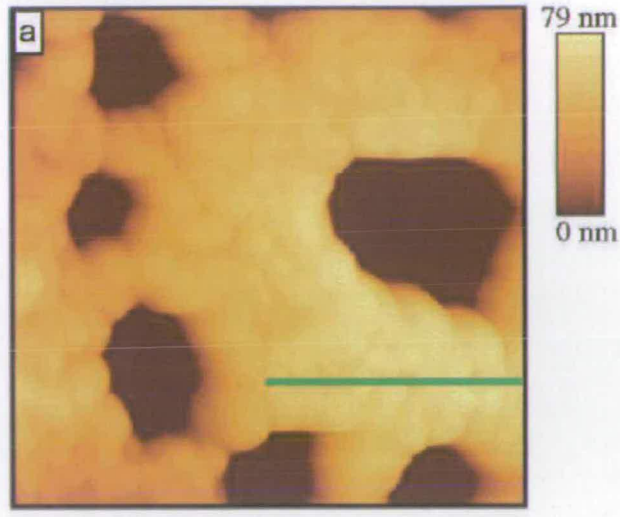

Figure 3.2: AFM image of the outer surface of a valve of diatom *C. granii*. The granular nanostructure of the surface is observed. The image is reproduced from Ref. [14].

39]. For instance, the cell walls of diatom *Cylindrotheca fusiformis* were found to contain significant amount of organic material which included some small proteins subsequently called "silaffins" [40] and long-chain polyamines (LCPA's) [39]. Other components are present but they are associated with biosilica only after deposition is completed [41, 42]. Three main silaffin fractions were identified with molecular weights of 4 kDa (silaffin 1A), 8 kDa (silaffin 1B), and 17 kDa (silaffin 2). Silaffin 1A itself was found to consist of a mixture of two peptides – designated $1A_1$ and $1A_2$ – with very similar primary structures. The primary structure of silaffin $1A_1$ contains serine (S), lysine (K), glycine (G), and tyrosine (Y) residues[1]: SSKKSGSYSGSKGSK. The serines are phosphorylated[2], while the lysines at positions 3 and 15 are each modified with a polyamine tail containing 5-10 *N*-methyl-propylamine $[-(CH_2)_3-N(CH_3)-]$ units connected to the backbone by a link of propylamine $[-(CH_2)_3-NH-]$ units (see Fig. 3.3).

[1]Amino acids which constitute the building blocks of many proteins.

[2]Phosphorylation is the addition of a phosphate (PO_4) group to a protein molecule.

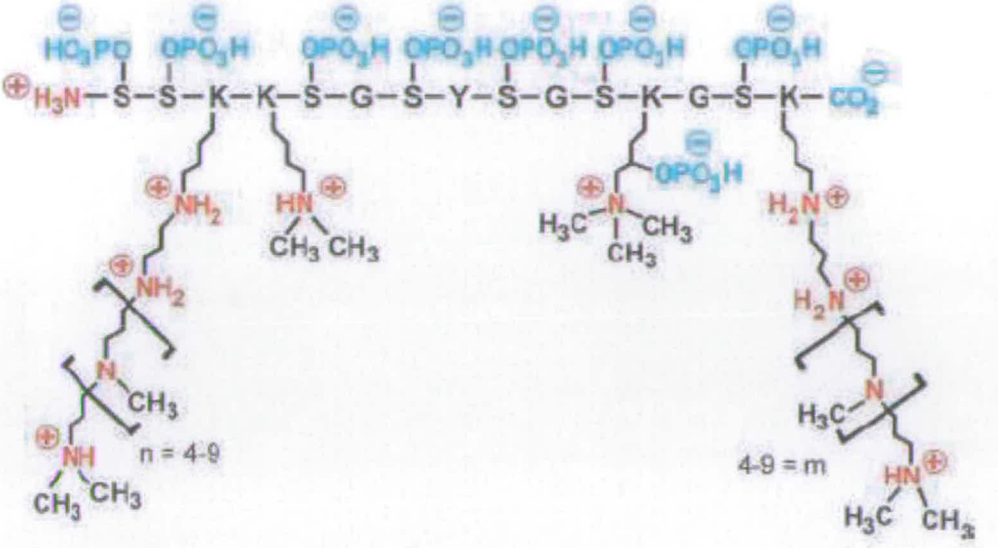

Figure 3.3: Pictorial representation of silaffin-1A_1. The post-translational modifications are in colour and the annotation of charges is for a solution at pH $\sim$ 5. The figure is reproduced from Ref. [15].

Since silaffins have been found harvested in the complex structures of some diatom frustules, experiments have been carried out in the past to find out whether silaffins alone could promote silica formation *in vitro* from a suitable precursor. Both silaffin 1A and 2 have been studied in a number of experiments. For instance, the addition of silaffins 1A (0.1-0.5 mM) to $\sim$ 1 M silicilic acid at pH $>$ 3 yields a precipitate of silica spheres with diameters in the range 400-700 nm [15, 40]. These final dimensions are not biologically relevant, but further experiments suggest that moldable silica-silaffin composites are produced during the first stages of biosilica formation. Large silica spheres can emerge from them as a result of subsequent artificial processes *in vitro* [15], for example the irreversible coalescence (due to unconfinement) of the silica-silaffin composites produced during the first stage of biosilica formation. In diatoms, instead, the formation of biosilica takes place within a membrane (silica deposition vesicle) which acts as a casting mold limiting the coagulation process. Silaffin 2 has been found to play a regulatory role in biomineralisation [43], whereas LCPAs

are known to promote formation of nanopatterned siliceous materials in different biological species [39, 44]. An exhaustive review of experiments on silaffins and LCPAs can be found in Ref. [2].

3.1.1 Silaffins

The fact that silaffins 1A alone are able to precipitate silica [15, 40] indicates that they have an inherent ability to self assemble [15]. From this starting point we carry out the first simulation-led investigation of how silaffins can promote the formation of 10-100 nm silica-peptide composites, which constitute biomineral building blocks on the nanometre scale (Fig. 3.2). It is tempting to speculate that these small peptides self-assemble to form aggregates that constitute a sort of template around which silica could condense [11, 45, 46]. A similar mechanism is generally adopted in the synthetic templating of porous materials, such as the MCM-41 [12, 13]. The silaffin backbone is made by polar amino acids and phosphorylated serines which are strongly hydrophilic due to the electrostatic and hydrogen-bonding interactions with water. We hence speculate that silaffins self-assemble because of an effective attraction between the two polyamine tails. This could arise either from a solubility mismatch between the tails and the backbone or from a phosphate-bridging mechanism, as we explain below.

Once protonated, the tertiary [3] amine groups represent the only polar units in the tails. However, the presence of other protonation sites in the tails decreases the probability of many sites being protonated simultaneously under neutralish conditions. In fact, the pK_a for the conjugate acid of an isolated tertiary amine group is usually around 9 [47], but in the present conditions it will

[3] In tertiary amines all three hydrogen atoms are replaced by organic substituents.

be significantly lower. To get an idea of the order of magnitude of this phenomenon, consider the following example. While the pK_a of the singly protonated N, N, N', N'-tetramethyl-1, 3-propanediamine $(CH_3)_2N(CH_2)_3N(CH_3)_2$ is 9.76, that of the doubly protonated molecule is 7.53. In our case, understanding the degree of protonation of the tails at finite dilution (where the activity coefficients differ from unity) is not easy, however, the presence of strongly hydrophobic parts (propyl and methyl units) in the tails themselves, for sure limits the extent to which the polyamine-tails can compete with the backbone for contact with the solvent[4].

Alternatively, a phosphate-bridging mechanism could also operate to favour the aggregation of polyamine chains [44, 49, 50]. It is indeed possible that the phosphorylated silaffin backbone could essentially provide the necessary bridging phosphate groups to mediate an effective attraction between the polyamine tails. In fact, previous studies reveal that the numerous phosphate groups in silaffins 1A could constitute an intrinsic source of anions for the formation of siliceous diatom materials [15]. Moreover, experiments on polyallylamines (PAA) with molecular weights in the region of 15 kDa show that the formation of aggregates is dependent on the concentration of phosphate anions (PO_4^{3-}) [44] and on the pH which tunes the interactions between the positively charged PAA parts and the negatively charged phosphate ions [49]. It is also seen that different anions do not facilitate aggregation, and so it is likely that there is a specific hydrogen-bonding mechanism for the cross-linking of the polyamine tails. Similar observations have been made with dephosphorylated silaffins [15] and poly(L-lysine) [50].

[4] A protonated propylamine unit by itself may possess amphiphilic characteristics; even small polar molecules, such as methanol and ethanol, do not fully mix with water on the molecular scale [48].

We therefore argue that there is an effective solvent-or added solute-mediated attraction between the polyamine tails driving self-assembly and hence template formation becomes possible.

3.2 Model and simulation methods

To verify our assumptions on a possible templating mechanism driven by silaffin self-assembly, it would be preferable to perform atomistically-detailed simulations. However, for the size of the molecules under consideration, and the lengthscales ($10 - 100$ nm) observed in experiments, this is not possible. We have therefore sought a coarse-grained model (Section 2.2.4) that retains the essential features of the silaffins, and ignores irrelevant atomistic and molecular details. On the basis of the arguments provided above we model the silaffins as consisting of a very strongly hydrophilic backbone and two mutually attractive (hydrophobic) flexible polyamine tails. We use a so-called *bead-spring* model widely used and tested in previous simulations of polymers [51–53] and amphiphiles [54]. Each bead represents a group of atoms and the beads are connected to each other via extensible springs mimicking the bonds. We will use Brownian dynamics (BD) simulations to assemble and study silaffin aggregates that could be formed and hence identify putative structures which might act as scaffolds for biosilica spheres.

3.2.1 Silaffin model

The silaffin backbone consists of 15 amino acids. Due to its high concentration of phosphorylated serine units, it is likely that the backbone will form an elongated β-strand in solution rather than a more compact α-helix. Since in

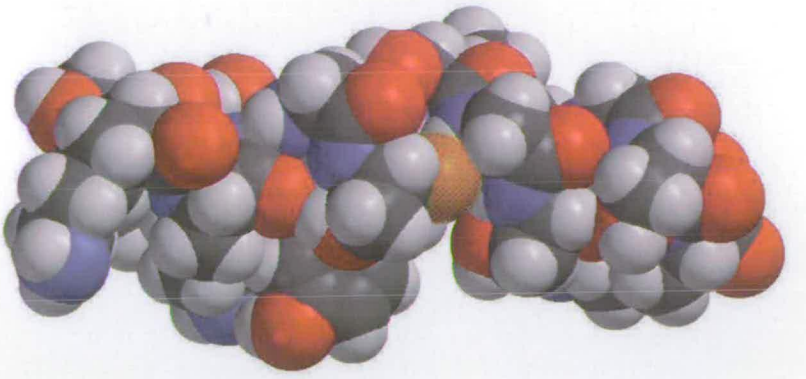

Figure 3.4: Atomistic simulation snapshot of a silaffin $1A_1$ backbone after equilibration [55].

crystals the average spacing between amino acids is roughly 0.35 nm, we assume that the length of the backbone is $\sim$ 6 nm. Furthermore atomistic simulation studies on a single silaffin backbone [55] show that its structure after equilibration resembles three joined blobs (Fig. 3.4). We therefore represent the backbone with three hydrophilic "head" (H) beads mimicking five amino acids each. The beads are then linked by finitely extensible nonlinear elastic (FENE) springs (to be defined below) in order to define the essential structural characteristic of the molecule (Fig 3.5). Each silaffin tail, which typically consists of $\sim$ 10 propylamine units (two C-C bonds and one C-N bond each), has a length roughly comparable to that of the backbone assuming $C-C$ and $C-N$ bond lengths of $\sim$ 0.15 nm. Therefore we represent each polyamine tail by three tail (T) beads, again linked by FENE springs. A pictorial representation of the resulting coarse-grained model is in Fig. 3.5. For the sake of comparison to the experimental results reported in Section 3.3, and on the basis of the arguments reported above, we assume the bead diameter to be roughly equal to 2 nm.

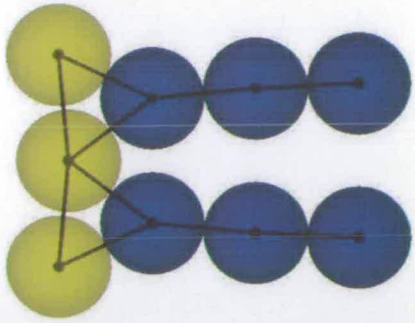

Figure 3.5: Computer model of silaffin considered in this work. The yellow beads represent the peptide backbone, and the blue beads represent the polyamine tails. The FENE springs are shown as black lines connecting the beads.

3.2.2 *Simulation methods*

We define the bead-bead interactions in terms of the Lennard-Jones (LJ) potential

$$u_{\mathrm{LJ}}(r) = 4\epsilon\left[\left(\frac{\sigma}{r}\right)^{12} - \left(\frac{\sigma}{r}\right)^{6}\right] \tag{3.1}$$

where σ is the bead diameter and ϵ is the potential well depth. The head-head (HH) interaction potential is chosen to coincide with the Weeks-Chandler-Andersen potential [56], which is purely repulsive, and in this case reflects the assumption that the components of the hydrophilic backbone are ambivalent toward solvation and mutual interaction:

$$u_{\mathrm{HH}}(r) = \begin{cases} u_{\mathrm{LJ}}(r) - u_{\mathrm{LJ}}(r_0) & r \leq r_0 \\ 0 & r > r_0. \end{cases} \tag{3.2}$$

$r_0 = 2^{1/6}\sigma$ is the position of the minimum in the LJ potential. The tail-tail (TT) interaction potential must include an attractive part in order to promote aggregation of the hydrophobic tails:

$$u_{\mathrm{TT}}(r) = \begin{cases} u_{\mathrm{LJ}}(r) - u_{\mathrm{LJ}}(r_c) & r \leq r_c \\ 0 & r > r_c. \end{cases} \tag{3.3}$$

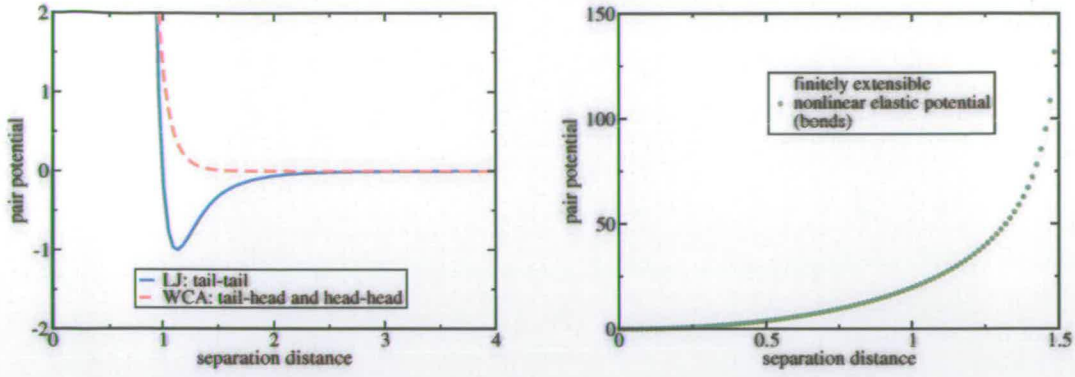

Figure 3.6: Representation of the effective potentials used in the simulations. The plot are in reduced units.

The cut-off distance is chosen to be $r_c = 2.5\sigma$; this is a cut-and-shifted LJ potential and is continuous at $r = r_c$. The tail-head (TH) interaction, finally, is taken to be the same as the HH interaction of Eq. (3.2). The FENE bead-bead spring potential is defined as follows

$$u_{\text{FENE}}(r) = -\frac{1}{2}kR_0^2 \ln\left[1 - \left(\frac{r}{R_0}\right)^2\right] \tag{3.4}$$

where $k = 30\epsilon\sigma^{-2}$ is the spring constant, $R_0 = 1.5\sigma$ is the maximum allowable separation between bonded beads. These values have been employed in previous simulations of polymers [57] and should be qualitatively correct in the case of peptides which are basically biopolymers.

With a cutoff distance of $r_c = 2.5\sigma$, the range of the potential $u_{TT}(r)$ is comparable with the bead diameter. At first glance, this situation appears somewhat unrealistic because each bead (representing many functional groups) has dimension ~ 2 nm, while direct interatomic forces are limited to the subnanometre range. However, it is important to remark that coarse-grained "potentials" are really free energies, resulting from an integration over the solvent degrees of freedom, with the beads held fixed. Therefore, the interaction range not only include those typical of interatomic forces, but also should be extended

to accommodate longer-range, solvent mediated effects such as hydrophobic attraction [58].

We performed BD [24] computer simulations of $N_m = 300$ or $N_m = 600$ molecules (corresponding to $N_b = 2700$ and $N_b = 5400$ beads, respectively) in a cubic box with periodic boundary conditions applied. The mass of each bead was set to be m and the equations of motion (2.14) integrated numerically by means of a Verlet-like algorithm [24] using a reduced time-step $\delta t = 0.01\tau$, where $\tau = \sqrt{m\sigma^2/\epsilon}$ is the basic unit of time. In all simulations, we chose a reduced friction coefficient $\xi = 5\tau^{-1}$ to represent the damped dynamics of the model beads each of them associated to large chemical units. The reduced temperature T^* was set equal to ~ 1 ($T^* = k_{\mathrm{B}}T/\epsilon$, where k_{B} is Boltzmann's constant) in order that the attraction between tails could prevail over the entropy penalty associated with clustering. Finally, the reduced bead density is $\rho^* = N_b\sigma^3/V$, and the approximate volume fraction is $\phi = \pi\rho^*/6$.

We carried out equilibration and production runs (each consisting of $\sim 10^5$ time steps) for each state point considered. [The equilibration runs were carried out at high temperatures ($T^* \sim 5$)]. The simulation was deemed to be equilibrated only after comparing energies and cluster distribution functions (see following Section 3.3) from four independent runs with different initial configurations and random-number generator seeds (for the stochastic force part). For low densities $\rho^* \leq 0.1$, systems of $N_m = 300$ molecules were sufficiently large to accommodate the self-assembled structures that emerged. At higher densities ($\rho^* = 0.3, 0.5$) systems of $N_m = 600$ molecules were studied in addition to check for finite-size effects (which were found to be insignificant).

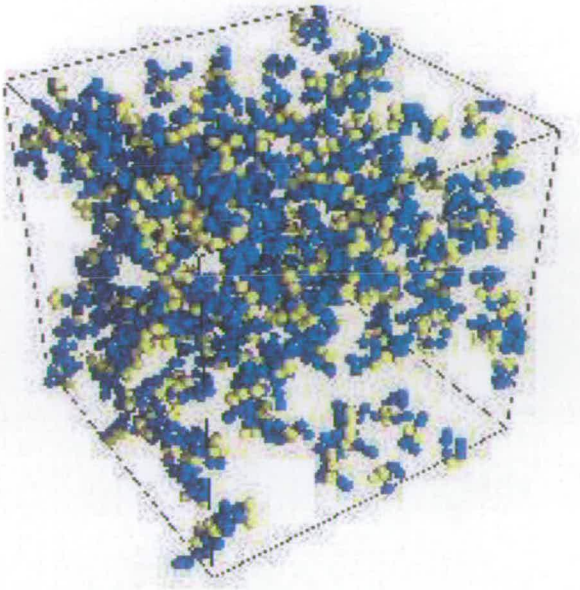

Figure 3.7: Final simulation configuration at $T^* = 1.5$ and $\rho^* = 0.1$.

3.3 Results and discussion

We first performed test runs at very low temperatures ($T^* < 0.5$) and high temperatures ($T^* > 1$). The runs at low temperatures were found to be very slow to equilibrate and therefore impossible to perform in a reasonable time, although the system clearly exhibited self-assembled structures which were possibly metastable. On the other hand, the simulations at high temperatures, showed no significant signs of aggregation (Fig. 3.7). We therefore decided to concentrate on two temperatures in between these extremes, $T^* = 0.5$ and $T^* = 0.8$.

3.3.1 Self-assembly

In Fig. 3.8 we show final configurations at a representative selection of densities, and at temperatures of $T^* = 0.5$ and $T^* = 0.8$. At low densities ($\rho^* \leq 0.1$) distinct aggregates resembling micelles are in evidence. As we will discuss in Section 3.3.2, at higher densities ($\rho^* = 0.3, 0.5$) the fluid is characterised

by extended networks of elongated structures that locally resemble bilayers or worm-like micelles, with the polyamine tails interdigitated. The self-assembled structures possess cavities which of course are filled with solvent (and a silica precursor) in real systems. Interestingly, the observed structures resemble those observed in simulations of gemini surfactants [54] and the extended networks of triblock-surfactant templates [59].

3.3.2 *Structural properties*

Due to the different properties exhibited by the fluid at low and high densities, we examine these two cases separately.

Structure at low density ($\rho^* \leq 0.1$)

We studied cluster formation at low densities ($\rho^* \leq 0.1$) by computing the volume fraction of aggregates containing n molecules, ϕ_n. Two molecules were deemed to belong to the same cluster if any of their mutually attracting tail beads were within a cut-off distance $r_{\text{tail}} = 1.5\sigma$. This criterion works well for surfactants models [60, 61]. The overall degree of micellisation (at a certain temperature) was therefore studied by analysing the plot of the volume fraction of free molecules (ϕ_1) against the total volume fraction (ϕ), as shown in Fig. 3.9. At very low concentrations, we see that the points in the graphs lie approximately on the straight line $\phi_1 = \phi$ as should be expected when there is little or no aggregation. At $T^* = 0.5$ the free-molecule concentration reaches a peak at a total volume fraction $\phi \simeq 0.008$, whilst at $T^* = 0.8$ the peak occurs at $\phi \simeq 0.01$; we define these positions as "critical micelle concentrations" [62] (see Section 1.1.1). At higher concentrations, micelles coalesce to form larger aggregates and, ultimately, structures whose characteristic dimensions are comparable to the dimensions of the simulation cell.

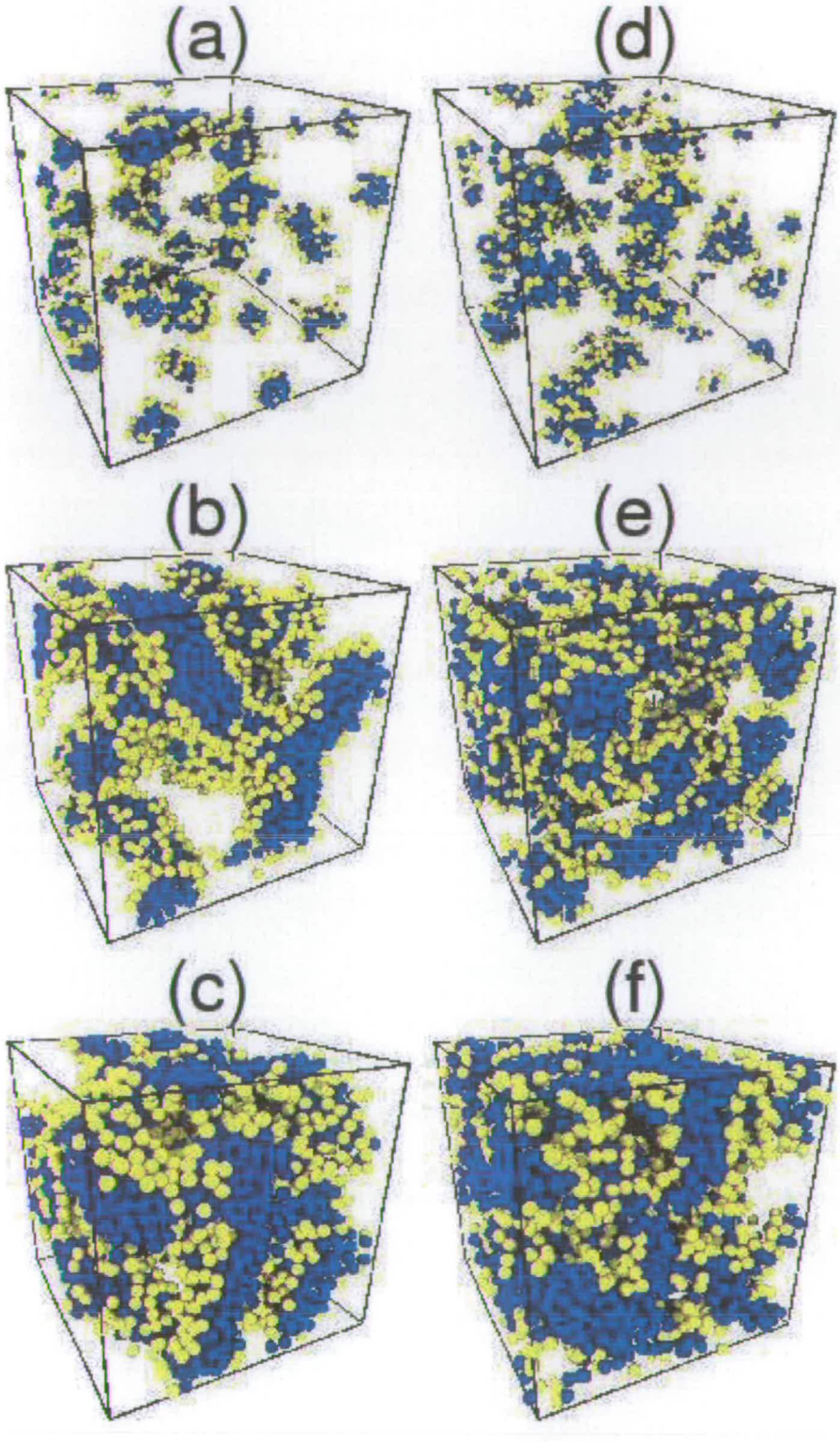

Figure 3.8: Simulation configurations after equilibration: (a) $T^* = 0.5$, $\rho^* = 0.06$; (b) $T^* = 0.5$, $\rho^* = 0.3$; (c) $T^* = 0.5$, $\rho^* = 0.5$; (d) $T^* = 0.8$, $\rho^* = 0.06$; (e) $T^* = 0.8$, $\rho^* = 0.3$; (f) $T^* = 0.8$, $\rho^* = 0.5$. System sizes at $\rho^* = 0.06$ are $N_m = 300$ molecules, while those at $\rho^* = 0.3$ and $\rho^* = 0.5$ are $N_m = 600$ molecules.

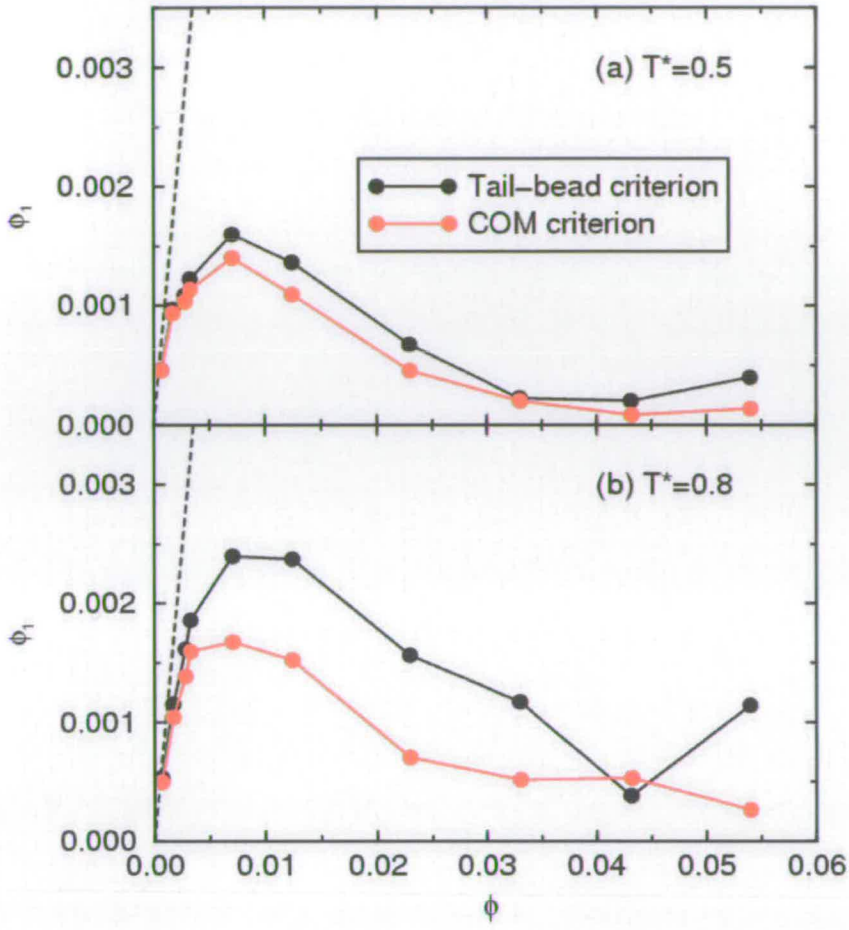

Figure 3.9: Volume fraction of free monomers (ϕ_1) against total volume fraction (ϕ) at temperatures (a) $T^* = 0.5$ and (b) $T^* = 0.8$. The black points represent the tail-bead distance criterion, and the red points represent the molecular center-of-mass distance criterion (see text). The dashed lines represent the asymptotic, low-density dependence $\phi_1 = \phi$.

The analysis reported above relies on a meaningful definition of cluster; it is therefore of fundamental importance to identify and define micelles in an unambiguous fashion. So far, our definition has been based on a tail-bead distance criterion, in line with earlier works [60, 61]. However, in the case of molecules with very long tails, this criterion becomes necessary but not sufficient to identify two monomers belonging to the same aggregate (two beads on different tails being close to each other might not be sufficient to bind the molecules together). We have therefore tested a new criterion which relies on the separation of the molecular centres-of-mass (COMs). In order to identify an appro-

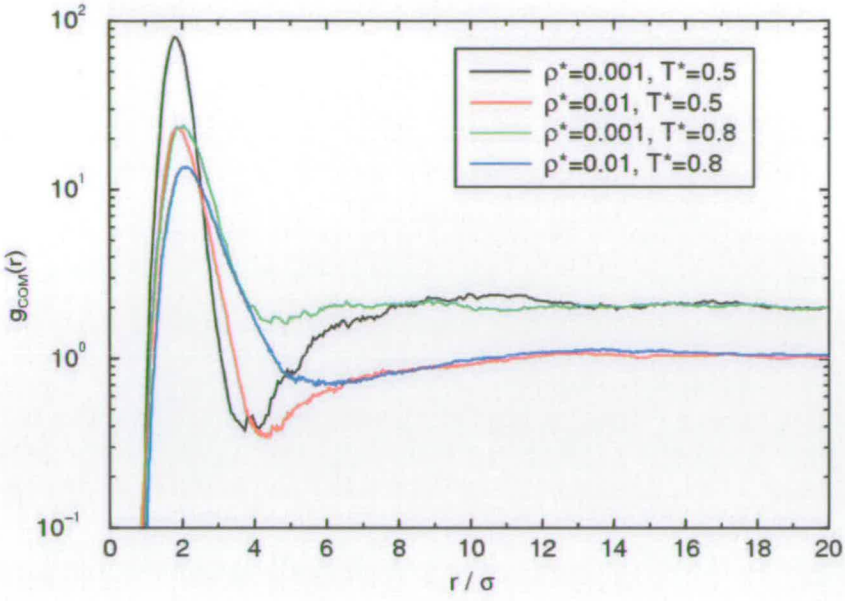

Figure 3.10: Center-of-mass radial distribution functions, $g_{\mathrm{COM}}(r)$ at $\rho^* = 0.001$, $T^* = 0.5$ (black), $\rho^* = 0.01$, $T^* = 0.5$; (red), $\rho^* = 0.001$, $T^* = 0.8$ (green), and $\rho^* = 0.01$, $T^* = 0.8$ (blue). The curves for $\rho^* = 0.001$ (green and black) approach $g_{\mathrm{COM}}(r) = 1$ at $r \gg 20\sigma$ (not shown).

priate cut-off distance, we first calculated the centre-of-mass radial distribution function, $g_{\mathrm{COM}}(r)$ [24]. Examples are shown in Fig. 3.10 for systems at various densities and temperatures. Then, we identified the minima demarcating the primary coordination shell. In the example they occur in the range $r = 4 - 6\,\sigma$. These distances provide natural criteria for discriminating between aggregated and free pairs of molecules. We implemented the COM criterion with a cut-off distance $r_{\mathrm{COM}} = 5\sigma$ and compared the results to those obtained using the tail-bead distance criterion, as shown in Fig. 3.9. At low volume fractions, the two criteria yield very similar results; this outcome was expected since clusters are easily distinguished from each other, even visually. [Figs. 3.8 (a) and 3.8 (d)]. Interestingly, at higher concentrations the COM criterion yields a smaller number of free monomers, particularly so at the higher temperature ($T^* = 0.8$). A plausible explanation for what we observe could be that because of their shape and the density, two model silaffins can have their centre-of-mass in close proximity even though their tail beads are beyond the range of attractive interactions.

Nonetheless, Fig. 3.9 shows that critical micelle concentrations (corresponding to the positions of the peaks in ϕ_1) remain insensitive to the criterion adopted.

We now analyse some structural lengthscales which might correlate with the size of the silica spheres that constitute the building blocks of many diatom cell walls. One important dimension to be taken under consideration (especially in the low density regime) is the average separation between two clusters, here denoted by l. In order to estimate l, we need to calculate the average cluster density which is given by

$$\langle \rho^*_{\text{clust}} \rangle = \frac{\rho^*}{9\langle n \rangle} \tag{3.5}$$

where 9 is the number of beads in each molecule and $\langle n \rangle$ is the average number of molecules per cluster. Hence, in reduced units l can be calculated using

$$\frac{l}{\sigma} = \left(\frac{1}{\langle \rho^*_{\text{clust}} \rangle} \right)^{1/3}. \tag{3.6}$$

$\langle n \rangle$ (calculated using the tail-bead distance criterion) and l are shown in Fig. 3.11 as functions of density for the temperatures $T^* = 0.5$ and $T^* = 0.8$. As the concentration of silaffins increases, the average cluster size $\langle n \rangle$ grows too, and above $\rho^* \simeq 0.1$ all molecules in the system belong to the same cluster. The average separation between micelles instead, appears to decrease monotonically with the density down to a value of approximately 10σ. It is therefore tempting, in this density regime, to speculate on the possibility that silica spheres might grow out radially from the surfaces of the newly formed clusters, or indeed, at lower densities, from a single peptide. This situation has already been observed in a series of experiments [63–65] in which silica condensation is seen being catalysed by charged surfaces. In this scenario, it would be possible to compare the dimension of the growing silica spheres to the mean separation between clusters, because the silica spheres might grow out radially

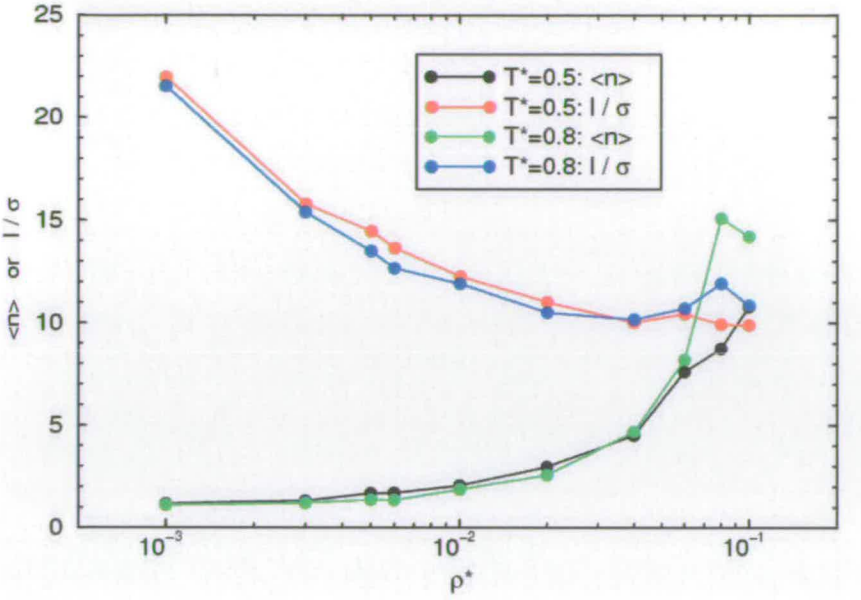

Figure 3.11: Average number of molecules per cluster ($\langle n \rangle$) and average cluster separation (l/σ) at $T^* = 0.5$ (black and red, respectively) and $T^* = 0.8$ (green and blue, respectively).

from spherical nuclei until they come in contact, and so the sphere size would be dictated by the mean separation between neighbouring clusters. In fact, we note that over a broad range of volume fraction ($0.05\% \leq \phi \leq 5\%$) and density range, the separation l does not vary dramatically (see Fig. 3.11) being in the range $10 \leq l/\sigma \leq 20$. Recalling that in our simulations $\sigma \simeq 2$ nm, the silica-sphere diameter would be between 20-45 nm. This estimate is consistent with the dimensions of the silica building blocks seen in experiments of some diatom skeletons ($10 - 100$ nm) [14, 35–38]. However, it is important to notice that this comparison is far from being precise without knowing the real volume fraction of macromolecules in the diatom frustules. The nucleation mechanism proposed here is therefore to be verified by more detailed experiments. For instance, it would be very useful to know how the peptides are distributed within the silica building blocks in diatoms in order to have better clues to the mechanism of biomineralisation.

Structure at high density ($\rho^* > 0.1$)

In this section we will study the characteristic lengthscales of the structures that form in the fluid at moderate densities, $\rho^* > 0.1$. It is important to recall that in this density regime, our simulations indicate that the aggregates resemble worm-like micelles with other elongated shapes. The fluid appears rich in cavities (the spaces between the molecules) which separate different blocks of self-assembled structures. It is natural to therefore estimate the dimension of the cavities, because these are the regions in which silica is most likely to condense. To gauge the dimensions of the cavities we used two different approaches.

The first approach consisted in calculating the static structure factor $S(q)$, which measures fluctuations in the density, and is accessible through scattering experiments [23]. $S(q)$ was calculated directly using the relation

$$S(\mathbf{q}) = \frac{1}{N_b}\langle \rho_{\mathbf{q}} \rho_{-\mathbf{q}} \rangle \tag{3.7}$$

where $\rho_{\mathbf{q}} = \sum_{j=1}^{N_b} \exp\left(-i\mathbf{q}\cdot\mathbf{r}_j\right)$ is a Fourier component of the bead density, and $\mathbf{q} = \frac{2\pi}{L}(\mathrm{n}_x, \mathrm{n}_y, \mathrm{n}_z)$, with $\mathrm{n}_\alpha = 0, \pm 1, \pm 2, ...$, is a wavevector commensurate with the cubic periodic boundary conditions. Due to the isotropicity of the fluid, averages were taken for contributions with equal $q = |\mathbf{q}|$. In Fig. 3.12 we show the structure factor at the temperatures $T^* = 0.5$ and $T^* = 0.8$ and at the densities $\rho^* = 0.3$ and $\rho^* = 0.5$. At $\rho^* = 0.3$ and at both temperatures, peaks in $S(q)$ are visible in the region of $q \simeq 0.5\sigma^{-1}$. At $\rho^* = 0.5$ and $T^* = 0.5$, $S(q)$ continues to rise down to the lowest accessible wavevector ($q = 2\pi/L$) signaling that there is a structure which spans the simulation cell [Fig. 3.8 (c)]. At $\rho^* = 0.5$ and $T^* = 0.8$ a peak is apparent at $q \simeq 1\sigma^{-1}$. The peaks in the structure factor represent inhomogeneities in the fluid density on lengthscales of $\sim 2\pi/q$, that

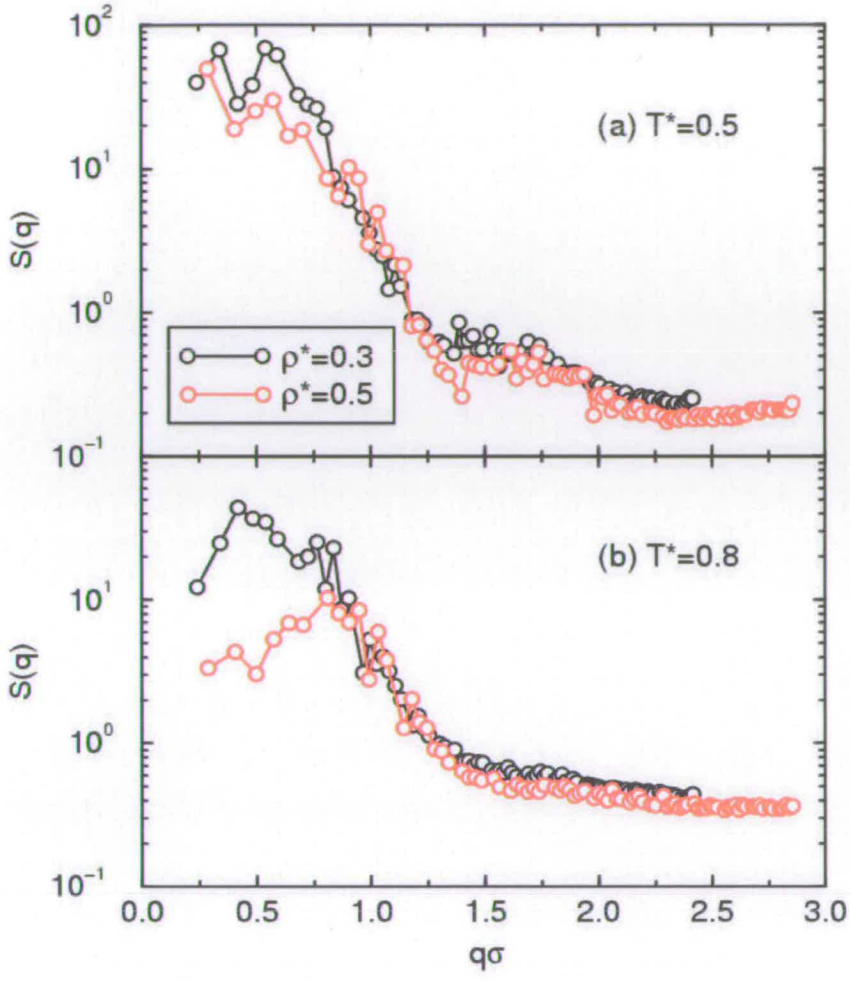

Figure 3.12: Bead static structure factor, $S(q)$, at temperatures (a) $T^* = 0.5$ and (b) $T^* = 0.8$. The black points are at density $\rho^* = 0.3$ and the red points are at $\rho^* = 0.5$.

is they give an indication of the dimension of the cavities. Recalling that in our simulations $\sigma \simeq 2$ nm, and reading the position of the peaks in $S(q)$, we are able to estimate, albeit roughly, the characteristic dimension of the voids. Peaks at $q = 0.5\text{-}1\sigma^{-1}$ correspond to real-space dimensions $(2\pi/q)$ in the range 13-25 nm. Again, this estimate is in agreement with the dimensions of the silica building blocks found in diatom skeletons [14, 35–38], and moreover consistent with our previous estimates made using a criterion based on the main separation between clusters (Section 3.3.2).

The second approach involved characterising the cavities by measuring the probability density of cavity sizes, $Q(r)$. Precisely, $Q(r)\mathrm{d}r$ is the probability that a chosen random point (probe point) in the simulation cell is at a distance between r and $r + \mathrm{d}r$ from the nearest model bead (Fig. 3.13). In our simulations, $N = N_b$ (where N_b is the number of beads) probe points were randomly selected every 20 time-steps and a histogram of $Q(r)$ was generated. In Fig. 3.14 we show examples of cavity distribution functions at densities $\rho^* > 0.1$ and at temperatures $T^* = 0.5$ and $T^* = 0.8$. In these graphs, $Q(r)$, shows two distinct main features: the first is a peak appearing at both temperatures at around $r \simeq 0.5\sigma$ representing small intramolecular voids; the second, most importantly, is the presence of peaks/shoulders at large values of r. These latter are the apparent cavities between different aggregates - see Fig. 3.8 (b) and (e). We suggest that the most relevant lengthscales for biomineralisations are the values of r above which $Q(r)$ tends essentially to zero, which are the values corresponding to the maximum dimension of the cavities (see Fig. 3.13 for a graphical illustration).

The curves in Fig. 3.14 are plotted on a linear-logarithmic scale to emphasise the the radii at which $Q(r)$ dies off. We now analyse the information contained in those graphs. If we assume that the cavities are spherical (an oversimplification), then the probability of choosing a point in the cavity at a distance between r and $r + \mathrm{d}r$ to its perimeter should scale like

$$p \sim 4\pi(r_{\max} - r)^2 \mathrm{d}r. \tag{3.8}$$

We fitted this function to $Q(r)$ in the proximity of $r_{\max}$ and reported the results in Fig. 3.14. In this way we can fit the values of $r_{\max}$ and therefore roughly estimate the dimension of the cavities. As is clear from the figure, the values of $r_{\max}$ lie in the range 3-6σ, which correspond to cavity diameters in the range 12-24 nm. These values once again have the same order of magnitude as the dimension of the cavities previously estimated via the structure factor and as

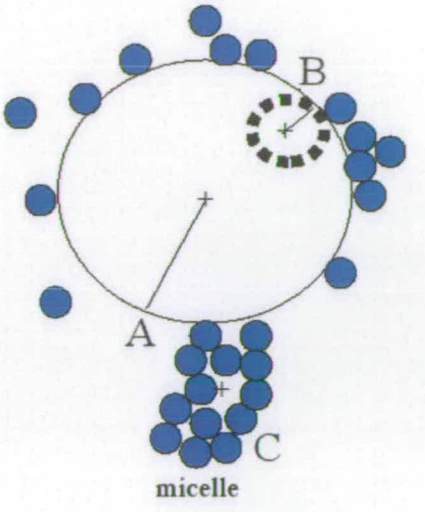

Figure 3.13: Schematic representation of cavity-definition criterion. The blue beads represent the model-beads. A probe point is inserted randomly in the simulation cell; three possible situations can then occur. In the case denoted A, the probe point is very luckily inserted near to the centre of the cavity. This situation is the least probable to occur and therefore corresponds to the regions of large r and low probability $Q(r)$ (though it gives the most reasonable measure of the dimension of the cavity). In case B, the probe point is inserted somewhere near the perimeter of the cavity; this situation is very likely to happen and is characterised by medium cavity-radius r and peaks/shoulders in $Q(r)$. In case C the probe point is inserted into an intramolecular cavity; this is the most likely situation and corresponds to the highest peaks centered around small r values.

measured in AFM experiments [14]. This supports the hypothesis that at silaffin volume fractions of 15-25%, silica might grow in the cavities and be guided by the self-assembled structures which would then constitute a template. The resulting composite of silica and silaffins might be the "moldable biosilica" from which certain (non-porous) structural elements of diatom skeletons are made [2].

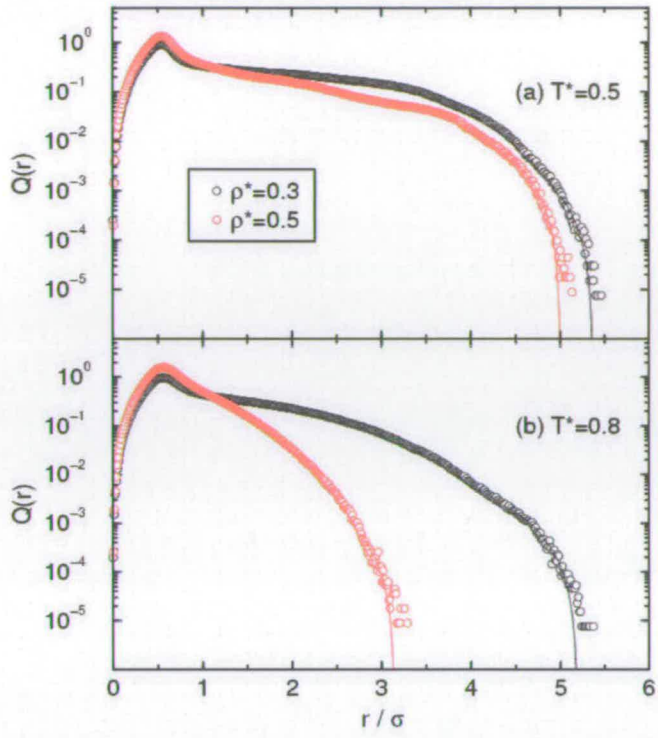

Figure 3.14: Cavity-radius probability distribution function, $Q(r)$, at temperatures (a) $T^* = 0.5$ and (b) $T^* = 0.8$. The black points are at density $\rho^* = 0.3$ and the red points are at $\rho^* = 0.5$. The solid lines are fits to the assumed asymptotic form at large r, $Q(r) \sim (r_{\max} - r)^2$, where $r_{\max}$ is the maximum cavity radius.

3.4 Conclusions

In this chapter we have reported a study of the self-assembly of model peptides in aqueous solution using coarse-grained Brownian dynamics computer simulations. The peptides consisted of polar hydrophilic backbones each made of fifteen amino acids, and each carrying two long polyamine tails. An effective attraction between the tails was proposed due to phosphate-bridging between protonated nitrogen centers and/or to hydrophobic interactions.

A variety of self-assembled fluid structures was observed by varying the volume fraction of peptides. At low volume fractions ($\leq 5\%$) distinct micelles are in evidence [Figs. 3.8 (a) and (b)] with the mean separation between them being in the range 20-45 nm, depending on concentration. Increasing the volume fraction to $\sim 15\%$ gives rise to elongated aggregates which span the simulation

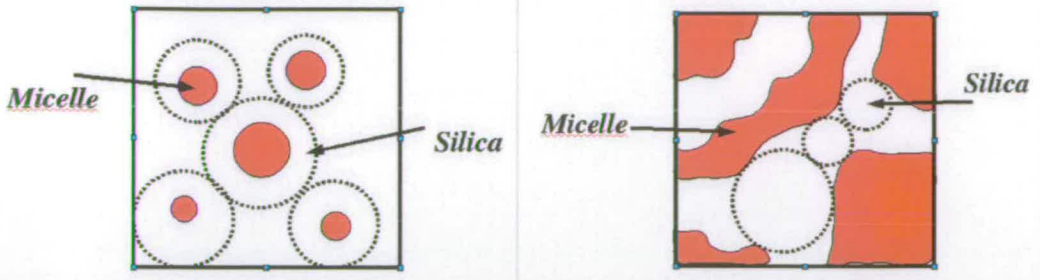

Figure 3.15: Schematic draw of the two possible scenarios for the production of moldable silica in diatom cell walls. Left: at low peptide volume fractions (< 5%). Right: at higher peptide volume fractions (> 5%).

cell. At volume fractions $\sim$ 25% bicontinuous structures appear characterised by the presence of cavities whose dimensions fall in the range 12-25 nm. These results, although obtained by a very crude model, are compatible with the dimensions of the silica building blocks found in diatom skeletons.

Our results suggest two possible scenarios that may be relevant to the production of moldable silica in diatom cell walls, each related to a certain regime of peptide volume fraction. At low peptide volume fractions, typically < 5%, distinct micelles are clearly visible as fundamental components of the fluid, suggesting that they could act as nucleation points from which the silica could grow outwards radially until they make contact to form a percolating structure (Fig. 3.15, left). In this case, the apparent silica-sphere diameter would be delimited by the mean cluster separation. At higher peptide volume fractions (> 5%), strands of peptides would instead confine the silica (Fig. 3.15, right). We are unable to tell which of the two scenarios is more likely to occur, because the concentration of peptides and their distribution in the diatom skeletons is unknown; high-resolution microscopy experiments, however, can help to achieve this goal. In fact, in the low-concentration scenario, the silaffins would be mostly concentrated in the cores of the silica building blocks, whereas in the high-concentration case they would be distributed more uniformly. As to the concentration of peptides in diatoms, we note that, as a general rule, the

volume fraction of macromolecules in a typical biological cell is of the order of 10% [66]. Alternatively, a volume fraction of $\sim 10\%$ might be representative of the *local* peptide concentration in the interior of large aggregates, or indeed a compartment of the cell. During the growth process, the silica would eventually envelope the underlying peptide matrix, possibly resulting in a moldable composite with superior mechanical properties; knock-on effects of the growing silica on the templating peptide have not been examined here, but this may be examined in future work.

Finally, we speculate more generally on the roles of long-chain polyamines and silaffins in biomineralisation. Long-chain polyamines in water likely form microemulsions of small droplets; indeed, this is the basis for the "phase separation" model proposed by Sumper [16]. Although this might lead to hierarchical patterning, it does not necessarily explain the fine structure of biosilica on the 10-100 nm scale. It is therefore conceivable that the role of the peptide backbones in silaffins is to frustrate microphase separation of the polyamine tails, and to promote local ordering on the molecular scale. This could be tested by analysing silica deposition as a function of polyamine chain length and/or backbone hydrophilicity; longer chains and less-repulsive backbone groups should favor phase separation over self assembly [67].

All the results reported in this chapter are speculative, however we have given concrete suggestions of how silaffins and peptides can finely tailor silica structures. Moreover we have also suggested straightforward experiments to verify our results.

CHAPTER 4

On the role of simple diamines on silicification

4.1 Introduction

In Nature, several classes of organisms process soluble silicon to generate highly organized amorphous biogenic silica structures under mild physical conditions of temperature and pH [63]. Diatoms, for instance, are equipped with symmetrically ordered mesoporous siliceous skeletons that offer essential rigidity and protection to the cell. Biosilica spicules in sponges provide protection as well as mechanical support [68]. In addition, silica and silicilic acid have been demonstrated to be of vital importance for plants during their growth, offering strength and resistance against insects and fungi [63]. Although biominerals are common in Nature, the molecular-scale processes that rule biomineralisation are still largely unknown.

Current synthetic techniques to produce mesoporous silicas require high temperatures and high pH [12, 13], and often result in poor control over the structure and the shape of the final product [63, 64, 69]. In fact, the synthetic pro-

duction of mesoporous materials is obtained by the so-called templating mechanism in which liquid mixtures consisting of long-chain surfactants and silica oligomers are used. Micelles, which form spontaneously, are then used as templates. Once the silica has condensed around the micellar template, the organic parts are removed by calcination leaving pores. Calcination consists of heating up the SiO_2/surfactant composite at very high temperatures with the aim of decomposing the surfactant molecules. These latter are then easier to remove from the complex by solvent extraction as the hydrogen bonds are much easier to break.

It has been estimated that the global market for silica and mesoporous materials is worth around two billion dollars a year in products used in a number of diverse areas such as separation technology, rubber reinforcement, desiccants and catalysis [64]. It is therefore crucial to understand how Nature effects biomineralisation, in order that we might achieve a comparable degree of control in synthesising silicas for technological applications [65, 69].

In this chapter, we analyse via computer simulations the role played by low molecular weight alkyldiamines in bioinspired silicification. *In vitro* experiments on putrescine homologues [1,2-diaminoethane (DA2), 1,4-diaminobutane or putrescine (DA4), 1,6-diaminohexane (DA6), 1,8-diaminooctane (DA8) and 1,10-diaminodecane (DA10)] carried out by our collaborators (Dr. D. Belton and Prof. C. Perry of Nottingham Trent University) show that the hydrophobic behaviour exhibited by the diamines and therefore their attitude towards micellisation is proportional to their carbon-chain length [63]. Hydrophobic effects are thought to be a fundamental factor regulating biomineralisation processes [63, 70]. To further test the biomineralisation scenario on the nanometre lengthscale proposed for the silaffins in Chapter 3, generalise it, and rationalise the experimental results collected by our collaborators, we have run Brownian

dynamics computer simulations of diamines at different concentrations using a bead-spring coarse-grained model similar to that used in Section 3.2.

4.2 Experimental results on putrescine homologues

In an interesting work on biomineralisation [63], Perry *et al.* reported experiments on silica deposition in the presence of putrescine homologues [$H_2N - (CH_2)_n - NH_2$] at concentration of 15 mM, and a silica precursor (dipotassium silicon triscatecholate). These experiments, which constitute the first [63] systematic and detailed study of the impact of low molecular weight diamines on silicification, show the formation of silica porous structures whose features depend on the length of the diamine chain and its hydrophobicity [63]. Micropores are observed in solutions of diamines DA2 and DA4, whereas mesopores characterise the final siliceous structure in presence of diamines DA6, DA8 and DA10. The average dimension of the pores falls in the range $30 - 50$ Å [63].

More recently, Perry *et al.* carried out experiments on solutions of putrescines at different concentrations ($c = 15$ mM, $c = 30$ mM, $c = 50$ mM) in the presence of, and without, a silica precursor (dipotassium silicon triscatecholate) [71]. The main structural features exhibited by the fluid can be grouped and summarised as follows [71].

4.2.1 *Solution depleted of diamines*

The formation of silica spheres was observed in solutions of the silica precursor, but depleted of diamines. The measured typical diameter d of these spheres falls within the range $2 - 4$ nm.

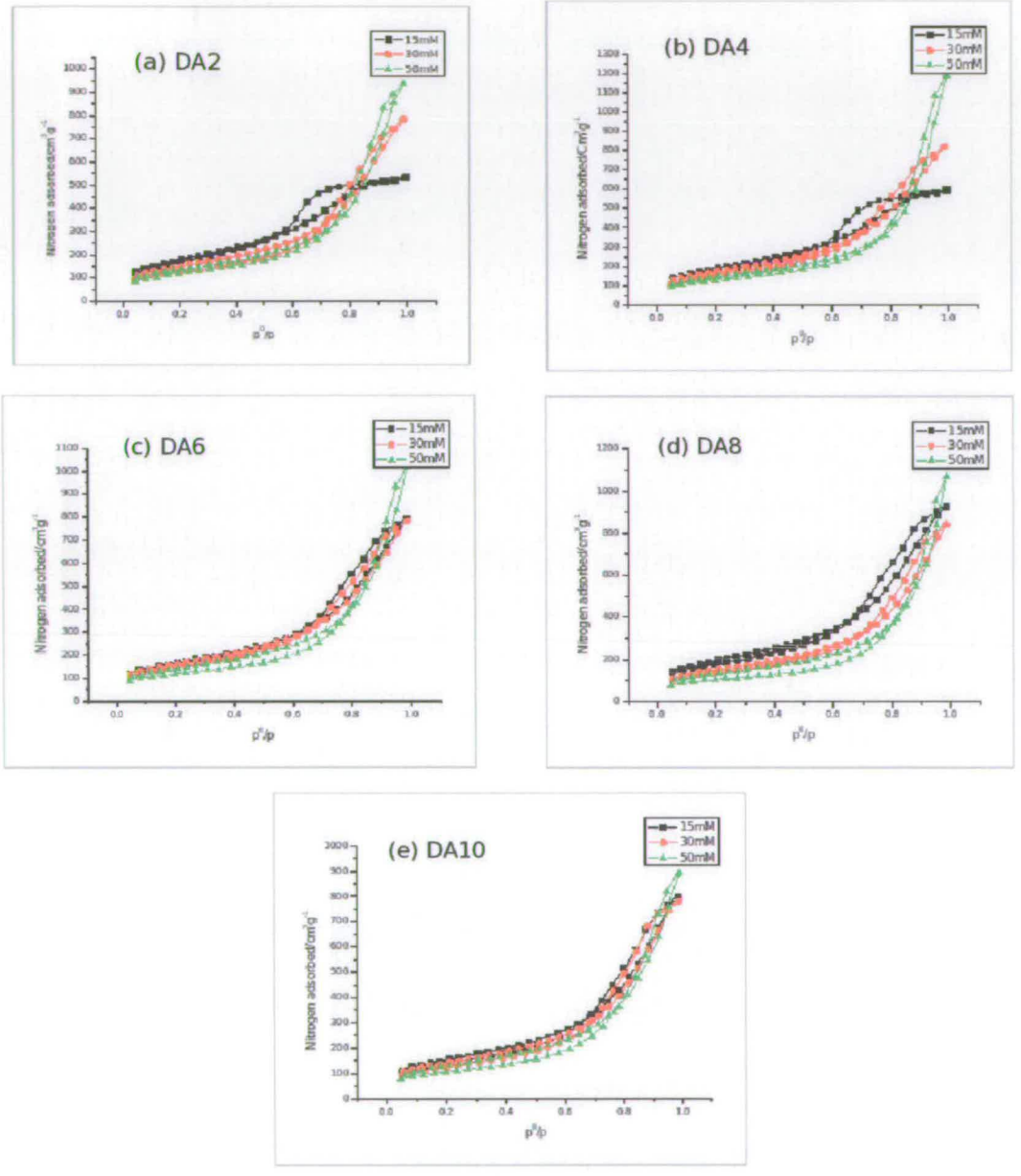

Figure 4.1: Absorption spectra of the final siliceous products for (a) a solutions containing DA2 diamines, (b) DA4 diamines, (c) DA6 diamines, (d) DA8 diamines, and (e) DA10 diamines [71].

4.2.2 *Putrescine at $c = 15$ mM*

DA2 and DA4 seem to exist in solution mainly as single molecules and are thought not to assemble into aggregates. When the silica precipitates in the form of nanospheres (of diameter $d \simeq 2 - 5$ nm), they sequester the diamines and, therefore, the silicas resemble very much the silica spheres formed in the absence of diamines (Section 4.2.1). The silica structures present micropores which have been studied in detail by analysing N_2 absorption isotherms. Due to the presence of micropores, DA2 and DA4 absorption isotherms present features characteristic of a "bottleneck" effect in which the N_2 gas has to be pushed hard to get into the micropores and similarly has to be pulled hard to get it out. The N_2 absorption isotherms present a characteristic hysteresis typical of this effect [Fig. 4.1 (a) and (b)].

Putrescine DA6, DA8, and DA10, on the other hand, because of the presence of mesopores in the final siliceous structure, are thought to form micelles. The self-assembled structures are thought to act as templates for the subsequent condensation of silica which is seen to coat these organic structures. Diamines can therefore direct the aggregation of the silica nanoparticles. The dimensions of the micelles, and hence the dimensions of the silica structures, increase with increasing n, the number of CH_2 groups in the molecule. The mesopores observed in the final siliceous products correspond to gaps between the silica nanospheres. As a consequence, the N_2 absorption isotherms no longer present the pronounced hysteresis observed in the case of putrescine DA2 and DA4 [Fig. 4.1 (c), (d), and (e)].

4.2.3 *Putrescine at $c = 30$ mM and $c = 50$ mM*

At these high putrescine concentrations, the final siliceous material presents more and larger pores (with diameters up to ~ 100 Å) because the extent of micellisation is thought to increase, irrespective of the diamine DAn considered.

These experimental results will be published as soon as possible.

4.3 Computer model and simulation methods

To gain insight on the experimental results reported in Section 4.2 on the role played by the different putrescine homologues in shaping the final inorganic product on the nanoscale, we followed a similar method to the one proposed in Chapter 3. For the present purpose, atomistically detailed simulations of these molecules (including the solvent explicitly) would make computer simulations extremely long, almost intractable. We have therefore sought and used a coarse-grained model which describes the diamines in terms of only their most fundamental properties, and ignoring irrelevant details. We model the diamines as linear chains of beads, connected by extensible springs representing the bonds. Each bead represents a chemical group and the interaction potentials will be solvent mediated effective potentials. Brownian dynamics simulations will be used to study the self-assembly of these model molecules and the role played by them in molding the final configuration of the inorganic material.

4.3.1 *Putrescine homologues model and simulation techniques*

We represent the diamines by means of a bead-spring coarse-grained model similar to the one adopted in Chapter 3 whose constituent beads interact via Lennard-Jones type potentials [24]. Interactions between hydrophilic beads are

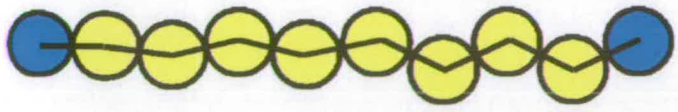

Figure 4.2: Example of molecular model considered in this work. The yellow beads represent the hydrophobic groups CH_2 and the blue beads the H_2N groups. The FENE springs are shown as black lines connecting two consecutive beads.

described by the potential (3.2), whereas hydrophobic beads interact via the potential (3.3). Adjacent beads are connected via the FENE potential (3.4) with parameters $k = 30\epsilon\sigma^{-2}$ and $R_0 = 1.5\sigma$. We stress again that in this model the interaction potentials must be considered as "effective" potentials [58] as explained in Chapter 3. An example of the resulting molecular structure[1] is illustrated in Fig. 4.2. For purposes of comparison with experimental data summarised in Section 4.2, we assume that the bead diameter is roughly equal to 0.34 nm (roughly corresponding to the Lennard-Jones diameter of the groups CH_2 and H_2N) irrespective of the diamine considered [72].

BD simulations [24] of $N_m = 288$ molecules – corresponding to $N_b = (n+2)N_m$ beads, where n is the number of CH_2 units in the molecule – at concentrations $c = 15$ mM, $c = 30$ mM, and $c = 50$ mM were carried out for each diamine system separately in a cubic simulation cell of volume $V = L^3$ with periodic boundary conditions applied . The masses of beads were set equal to m and the equations of motion (2.14) were integrated numerically according to a velocity-Verlet like algorithm [24] choosing a reduced time step $dt^* = 0.01$ and a reduced friction coefficient $\xi^* = 5$ that accounts for the dimension and the dynamics of the chemical units represented by each bead [8]. A set of reduced units similar to that reported in Chapter 3 was employed. The intensity of the interactions

[1] It is noted that a more accurate putrescine model should include a certain degree of stiffness for the carbon chain.

is measured in terms of the reduced temperature T^* and therefore it must be at the most on the order of the unity in order self-assembly to occur. In this work we concentrated on two temperatures $T^* = 0.5$ and $T^* = 0.8$. For each diamine system, simulations consisted of an equilibration part and a successive production run of 10^5 time-steps.

4.4 Simulation results and discussion

4.4.1 Self-assembly

In our simulations the diamines were seen to self-assemble producing micelles. A parameter that influences the degree of aggregation (for systems at the same concentration) is the number n of carbons in the molecules. For instance, DA10 putrescines are more likely to form micelles than DA2 putrescine because a larger number of CH_2 groups makes the molecule less miscible in solution and more inclined to form aggregates (see Fig. 4.4). In Fig. 4.3 we show the volume fraction Φ occupied by a micelle made of s molecules (we note that this quantity is proportional to the probability $P(s)$ of finding s molecules in a cluster). Two molecules were deemed to belong to the same aggregate according to the bead-distance criterion discussed in Chapter 3 with a cutoff distance $r_{\text{cut}} = 1.5\ \sigma$. Fig. 4.3 firstly suggests the appearance of bigger micelles as n increases, and secondly that the fluid becomes polydisperse rather than monodisperse as n tends to its maximum value ($n = 10$). These results are in agreement with the hypothesis that diamines with large n are more likely to self-assemble [63] and that, in this case, a similar nucleation mechanism to the one proposed in Chapter 3 in which the silica condensates around the organic aggregates can explain the presence of mesopores as observed in experiments (Section 4.2).

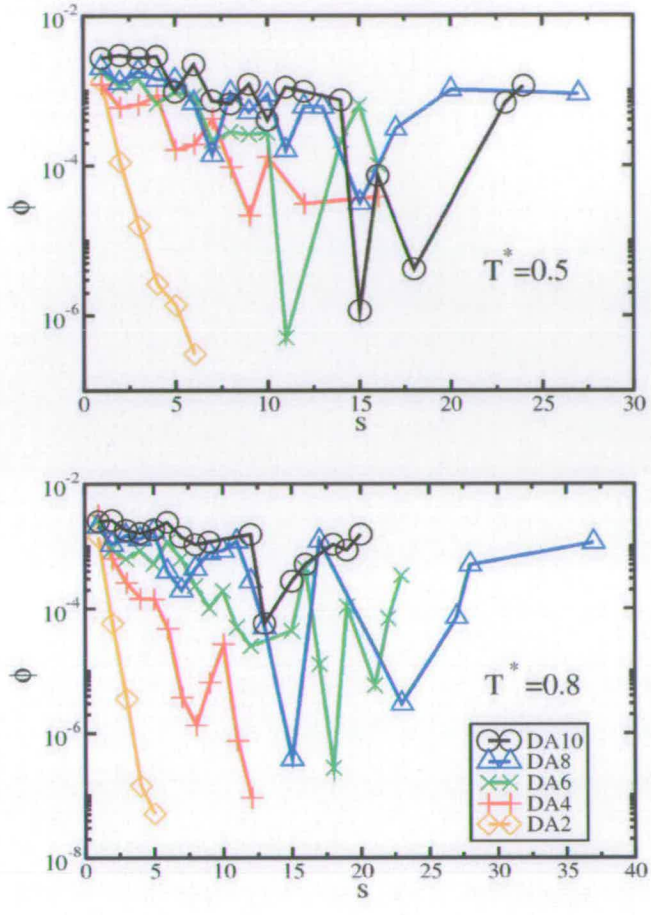

Figure 4.3: Volume fraction $\Phi(s)$ occupied by a cluster containing s molecules. Comparison between different putrescine homologues at $T^* = 0.5$ and $c = 15$ mM.

4.4.2 *Structure of the fluid*

In this section, we identify and quantify characteristic structural lengthscales that might correlate with the size of silica pores observed in vitro. Firstly, we use the data in Fig. 4.3 to calculate the average size of an aggregate. Fig. 4.5 shows the average number of molecules s in a cluster and the main separation distance l between two neighboring clusters as functions of the number of carbons in the molecule, that is

$$\frac{l}{\sigma} = \left[\frac{(n+2)s}{\rho^*}\right]^{1/3}, \tag{4.1}$$

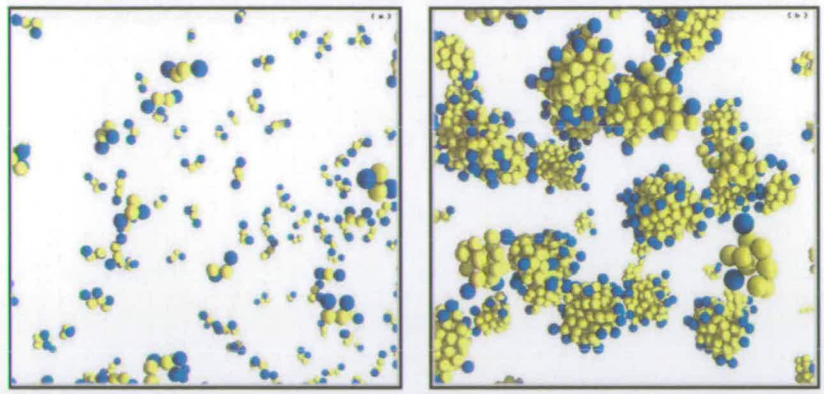

Figure 4.4: Simulation snapshots after equilibration: (left) DA2 and (right) DA10 at $c = 30\,mM$ and $T^* = 0.5$.

where ρ^* is the reduced *bead* density. The size s increases as the number n increases [Figs. 4.5 (a) and (c)]. Furthermore, we observe that for putrescine with a number n of CH_2 groups a variation in the concentration c barely affects the average dimension of the micelles [Fig. 4.5 (a) and (c)]. A clear dependence of the separation l on the number n is however observed as the concentration varies within the range $15 - 50$ mM [Fig. 4.5 (b) and (d)]. These results were found to be independent of the temperatures T^* considered in this study.

A visual confirmation of what we have just affirmed is provided by Fig. 4.4 where we show portions of final configurations for the systems DA2 and DA10 at $c = 30$ mM. DA2 diamines are shown to be less favorable to self-assembly due to the fact that the number of hydrophobic beads is too small. A very different behavior is shown in the case of DA10 where micellisation is more likely to occur as a result of a stronger hydrophobic effect [17].

According to the biomineralisation scenario discussed in Chapter 3, silica pores observed in vitro might be a direct result of the templating effect of diamine micelles. The sizes s, hence, can be used to give a rough estimation of the pore dimensions. If the volume occupied by one molecule is V_{DAn}, then a micelle containing s molecules will occupy a volume equal to sV_{DAn}. Assuming that

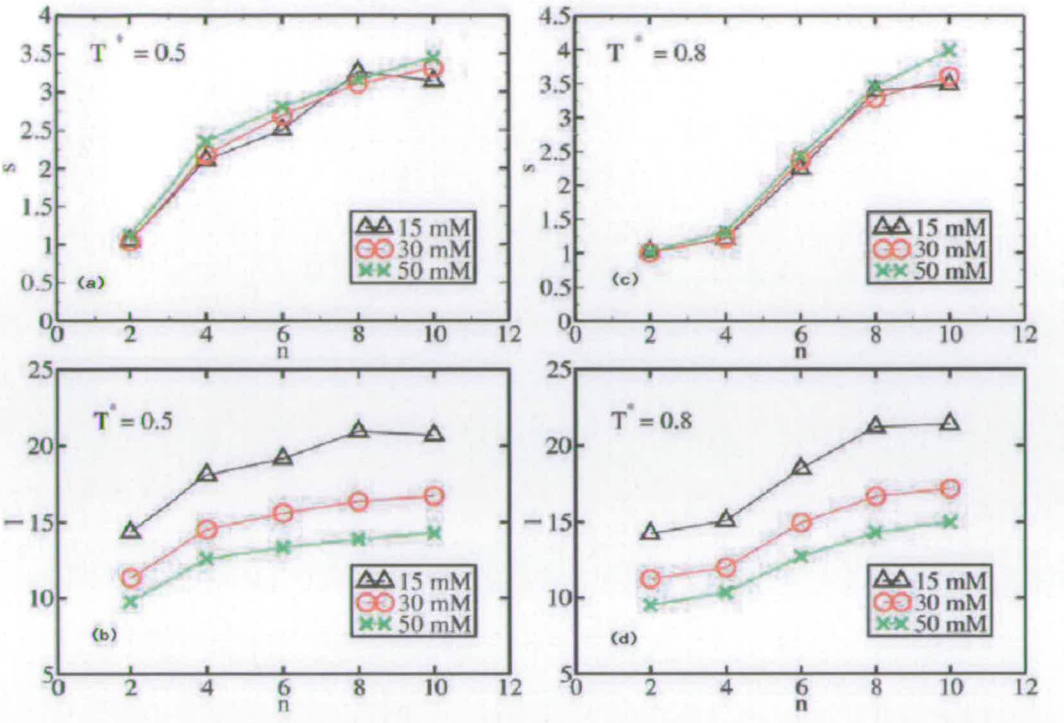

Figure 4.5: Average dimension s of a cluster and average separation l between clusters as a function of number n of carbons in the diamine. (a) Cluster dimension s at temperature $T^* = 0.5$, (b) main separation l between clusters at temperature $T^* = 0.5$, (c) and (d) are the cluster dimension and main separation at temperature $T^* = 0.8$.

a micelle is approximately spherical and made of beads in a close-packed configuration[2], the average radius of a pore in the silica is

$$\frac{R_{por}}{\sigma} = \left(\frac{3}{4\rho^*_{cp}}\pi s V_{\mathrm{DAn}}\right)^{1/3} \tag{4.2}$$

where $\rho^*_{cp} \sim 0.74$ is the reduced bead-density of a close-packed configuration [73]. We estimate that for concentrations spanning in the range $15-50$ mM the pore radii should fall approximately within the range $6-45$ Å. This estimation has the same order of magnitude as the silica-pore diameters measured in experiments by Perry [63] for putrescine at concentration $c = 15$mM, (namely $30-50$ Å), and is consistent with the results reported in Section 4.2.

[2]These are rough approximations but they help estimate the order of magnitude of the dimensions of the micelles.

As it is clear from Fig. 4.5 (a), DA10 diamines (c = 15 mM) produce reduced pore radii with respect to DA8; this effect, also observed in real experiments [63], is thought to be a function of the greater flexibility of the DA10 diamines compared to the other (DA6 and DA8) diamines used, thus allowing some degree of coiling of the hydrophobic chains to produce smaller micelles [63]. Nonetheless, we must point out that this feature seems to disappear at higher concentrations [Fig. 4.5 (a) and (b)] and temperatures [Fig. 4.5 (c) and (d)]. A possible reason for this could be that at higher concentrations and temperatures the micelles seem to assume more worm-like or elongated shapes rather than spherical ones (Fig. 4.6). This speculation can be tested, for instance, by calculating the radius of gyration of the micelles formed by different putrescine homologues and will be the object of future work.

The estimated dimension of the average separation (4.1) between neighboring aggregates falls within the range $10 - 20\ \sigma$ [Fig.4.5 (b) and (d)] independently from the concentration and the amine studied. On the basis of these results and on the basis of what was discussed in Chapter 3, we speculate on the possibility that diamine aggregates could provide suitable organic templates and act as nucleation points for the subsequent deposition of silica. In this scenario, a rough estimate for the dimensions of the silica spheres might be comparable to our estimate for l. According to our calculations, with $\sigma \sim 0.34$ nm, we predict the formation of silica spheres with diameters in the range $34 - 68$ Å. Again, this has the same order of magnitude as the characteristic lengthscales of silica structures observed in real experiments on diamines, namely several tens of ångströms [63, 65]. The self-assembly model introduced in Chapter 3, and further tested here for putrescine homologues, is therefore reasonable and consistent with the experimental observations summarised in Section 4.2.

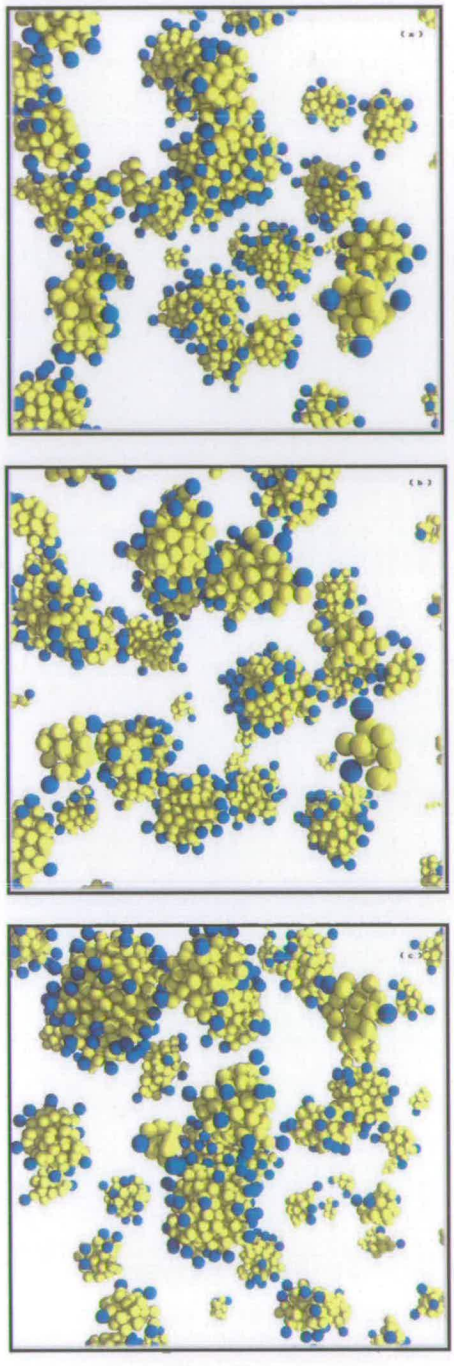

Figure 4.6: Selection of DA10 micelles at different concentrations: (a) c = 15 mM, (b) $c = 30$ mM and (c) $c = 50$ mM at $T^* = 0.5$.

An alternative and reasonable estimation of the dimension of the cavities, namely where silica condensation would occur, is also given by the static structure factor $S(\mathbf{q})$ (3.7). In Fig. 4.7 we show $S(\mathbf{q})$ for the smaller diamines (DA2) and

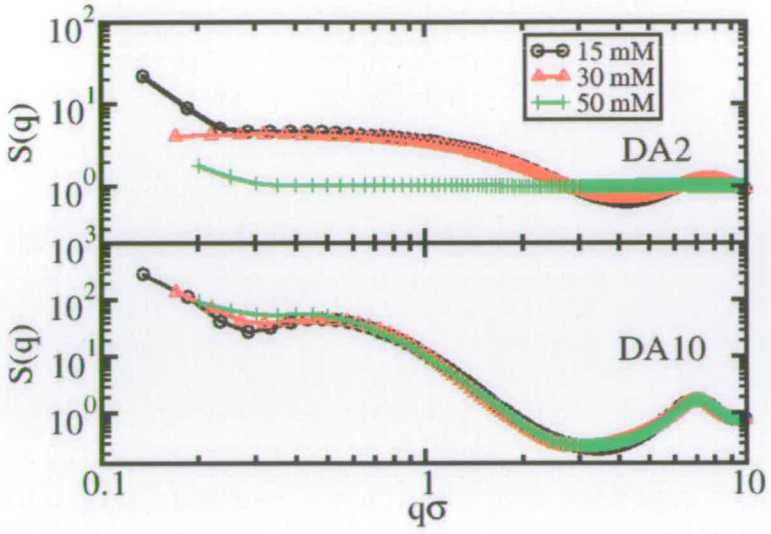

Figure 4.7: The bead static structure factors $S(q)$ for the systems DA10 and DA2 at different concentrations.

for the larger diamines (DA10) considered in this study at different concentrations and at the temperature $T^* = 0.5$. This figure highlights the differences between the fluid structures in the presence of DA2 diamines and in the presence of DA10 diamines. While DA2s barely promote any formation of clusters (evidence is in the presence of a *plateaux* in the structure factors at low q), DA10s strongly self-assemble to create micelles (peaks in DA10 structure factors at low q). DA10 structure factors present a first peak in the region $\sim 7\ \sigma^{-1}$ - due to intramicellar voids - and, more interestingly, a second one in the region $(0.3 - 0.6\ \sigma^{-1})$ suggesting an inhomogeneity in the bead density on the scale of $2\pi/q$, namely $\sim 30 - 70$ Å. These features are the *voids* that in our proposed mechanism will be filled out by the silica. These values have the same order of magnitude as those determined for l, meaning that these provide consistent estimates of the cavity dimensions. Moreover, the trends are in agreement with the experimental results reported in Section 4.2. Similar fluid structures were observed at $T^* = 0.8$.

4.5 Conclusions

In this chapter we have reported a coarse-grained computer simulation study on the effect of putrescine homologues on silica formation. The model diamines were typically made of unit beads connected by elastic springs and interacting via Lennard-Jones (LJ) potentials. Brownian dynamics computer simulations were performed in which each bead represented a single large chemical group such us CH_2 or NH_2 with diameter σ commensurate with effective coarse-grained potentials (free energies).

The model diamines were seen to self-assemble in our simulations due to the strong hydrophobic nature of CH_2 groups. A different behavior toward clusterisation was however observed as a function of number of hydrophobic groups in the molecules. At the temperatures and the concentrations studied, the degree of micellisation was seen to increase with the hydrophobicity of the molecules.

The fluid structure was characterized by measuring structure factors $S(q)$, mean distances between clusters l, and average micellar dimensions. These estimates were in agreement with each other, and with the experimental results.

Our simulation results give a strong suggestion on a possible biomineralisation scenario which might lead to the formation of the silica structures observed in vitro. In particular, a possible mechanisms for the production of siliceous mesoporous materials driven by self-assembling of amines was pointed out. In this scenario, the different degree of hydrophobicity of these molecules was seen to tune and regulate the dimension of the pores in the silicas. A qualitative agreement between our simulation results and the experimental results for diamines at the concentrations of 15 mM, 30 mM, and 50 mM was observed.

CHAPTER 5

Pattern formation in diatom cell walls

5.1 Introduction

Diatoms are unicellular, photosynthetic organisms found in marine and freshwater environments. The diatom cell is encapsulated in a porous, symmetrical and amorphous silica-shell (frustule) [3, 74]. The ability of Nature to model such complex structures starting from formless silica (SiO_2) makes diatom morphogenesis very interesting. In many diatom species the frustule comprises two valves which can be either circular (as in *centric* diatoms) or elongated (as in *pennate* diatoms) when observed in cross section (Figs. 5.1 and 5.2). These valves are often fashioned with complex and in some cases highly ordered arrays of nanometre- to micrometre-scale slits and pores. Their graceful forms

Figure 5.1: Some centric diatoms microscopy images. Reproduced with permission from Ref. [4].

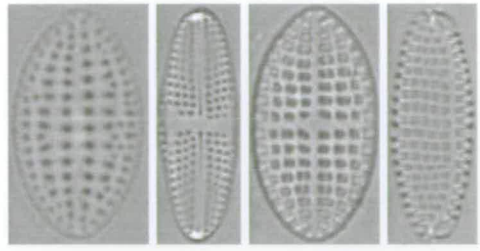

Figure 5.2: Some pennate diatoms microscopy images. Reproduced with permission from Ref. [75].

and fine details are highly species-specific and hence vital to taxonomic classification [3]. Figs. 5.1 and 5.2 show a small selection of microscopy images to fully appreciate diatom skeletons' graceful forms. It is a major goal of material science to understand diatom morphogenesis in order to achieve a high degree of control in the synthesis of complex microstructures for a variety of nanotechnological applications.

In this chapter, we propose a physical mechanism for a key stage in the development of siliceous diatom skeletons, namely the formation of complex templates on the tens-of-micrometre lengthscale which guide the deposition of silica into complex structures. Our model takes into account the fundamental processes already identified in experimental investigations of diatom morphogenesis, namely, the role of templating by structures under cellular control (*base layer*), and by complex fluid structures under exclusively physico-chemical control. In particular, we will show that a phase separation mechanism occurring in the presence of a mild degree of prepatterning (which mimics the cellular contribution to the morphogenesis) can generate suitable templates for the deposition of silica into forms as observed in a number of diatom structures. This process might provide a means of manufacturing microscale porous architectures which can used in a number of applications such as molecular sieving.

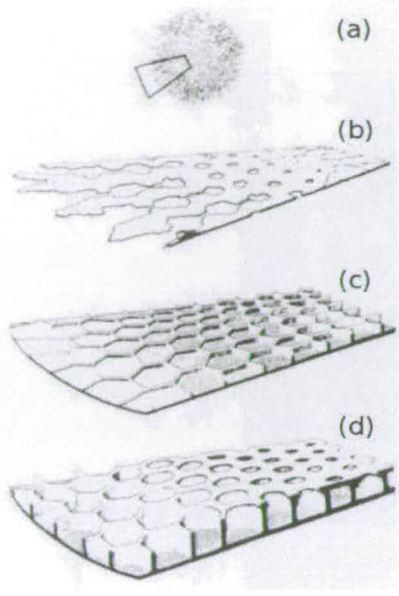

Figure 5.3: Different stages of morphogenesis of diatom skeletons. A base layer made of costae and vesicles is deposited (b); vertical differentiation starts once the base layer is complete (c) and (d). Image adapted from Ref. [3].

5.1.1 Diatom morphogenesis

The formation of amorphous-silica diatom frustule during asexual reproduction has been widely studied during the past years in different time-resolved electron microscopy experiments [38, 76, 77]. Soon after the cell division, silica condenses near the surfaces of the daughter cell in a membrane-bound compartments known as silica deposition vesicle (SDV) [Fig. 5.3 a)]. This process is thought to occur in two separate stages [77]. During the first stage [Fig. 5.3 (b)], a base-layer ($\sim$ 30 nm thick) of silica is deposited. The base-layer possesses an irregular system of radial ribs [3] (called *costae* of which there are typically around 10-50 in centric diatoms) often separated by rafts of organic droplets and/or vesicles [76] which are believed to have played a role in the initial formation of the costae; according to the most accurate morphogenesis models (described later on in this chapter), these radial spokes might have formed as a consequence of diffusion limited aggregation of silica nano-particles [78]. In the

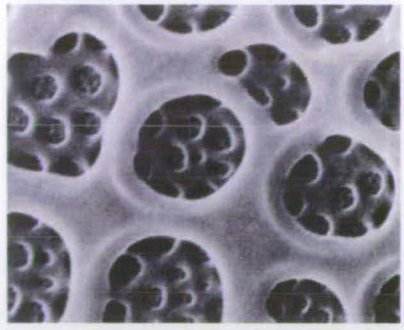

Figure 5.4: The base layer as seen through the larger pores of the final siliceous structure. Image adapted from Ref. [3].

second stage [Fig.5.3 (c) and (d)], the new valve acquires the necessary thickness ($\sim 10 - 100$ nm) by growing perpendicularly to the base-layer (leading to vertical differentiation). It is during this stage that the frustule acquires its final structure and fine details. It is observed that the structure of the base-layer does not necessarily correspond to the structure of the face of the new valve, however, in some species, small pores in the base-layer can still be observed through the larger pores of the final frustule structure (Fig. 5.4) [3]. Interestingly, the two stages described above take different amounts of time to complete; typically, the first stage is completed within $10 - 20$ min whereas the second could take up to several hours [38, 77, 79–81].

It is thought that the growth and patterning of the outermost parts of the frustule are not under direct cellular control, but are dictated only by physico-chemical factors. On the contrary, the deposition of the base layer can be purely attributed to cellular control. In the following sections we will formulate a theoretical model which uses reasonable physico-chemicals arguments to explain the growth and patterning of the outermost portion of the valve in the presence of the base layer.

5.1.2 Previous diatom morphogenesis models

One of the most striking features of diatom frustules are the rib-like costae. The most accurate predictive model of diatom morphogenesis to date is based on diffusion-limited aggregation (DLA) of silica nano-particles [78]. Amorphous silica particles are thought to be transported (possibly via microtubules) to the perimeter of the SDV and then released into it, whereupon they can diffuse and aggregate to form fractal structures growing outwards from the centre of the SDV. Computer simulations of this process (also including the simultaneous sintering of the growing silica) have shown that spoke-like patterns resembling the costae can easily be reproduced. Thus, DLA provides a reasonable physical mechanism for the production of the costae. Nonetheless, as mentioned above, it is clear that the formation of costae and, hence, of the base layer, is likely to be strongly influenced by intracellular factors, either through the positioning of microtubules or prepatterning on the surface by cytoskeletal components.

In diatoms, the usual physical mechanisms that control biomineralisation, such as nucleation phenomena, can be ruled out because the resulting siliceous material is amorphous - at least on the 100 nm scale and above. On the 10 nm scale biosilica structures have been extensively studied in experiments [14] and related to species-specific polypeptides [8] such as silaffins (Chapters 3 and 4) [2, 15, 40, 43]. At lengthscales of 100 nm or more, complex-fluid scaffolding mechanisms, in which self-organised structures direct the deposition of inorganic material [11], might play a vital role in the morphogenesis. Indeed, previous work suggests that organic components in the SDV that avoid co-precipitation with silica become more concentrated as the valves grow reducing the volume available for the organic components [77]. This would lead to the formation of organic vesicles or droplets which might constitute templates

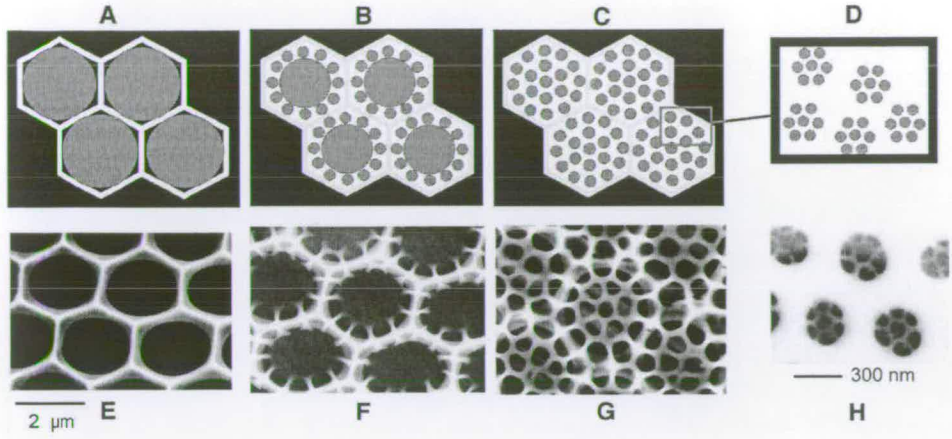

Figure 5.5: According to Sumper, phase separation in diatoms occurs in the following steps. Silica precipitation within organic (generally polyamines) droplets forms a honeycomb-like framework (a); silica "traps" or "consumes" a certain fraction of polyamines leading to a depletion of organic component in solution and hence to the formation of smaller polyamine-rich droplets (b); finally, silica continue precipitating and consuming other fractions of organic component hence generating the self-similar structure observed (c-d) (figure reproduced from Ref. [16]).

for the condensation of silica. The latter hypothesis and the discovery of amphiphilic, long-chain polyamines trapped in silica harvested from a number of diatom species led Sumper to propose a phase separation model that accounts for diatom morphogenesis. In this model, polyamines [2, 39, 44, 49], polypeptides [82], or other organic macromolecules phase separate from water in an aqueous solution upon the base layer to form a two-dimensional, self organised array of droplets / bubbles/ vesicles which are templates for the successive deposition of amorphous silica. A brief description of this model is given in Fig. 5.5. The phase separation model proposed by Sumper, however, is unable to predict all those diatom structures in which silica costae are present. Furthermore, this model represents a qualitative description of diatom morphogenesis which is not based on any rigorous calculations.

5.2 Computer simulations of diatom morphogenesis

There is currently no diatom morphogenesis model that can account for all the aspects of diatom-frustule morphogenesis. The DLA model of costa formation leaves the presence of arrays of pores in the frustules still unexplained [78]. On the other hand, Sumper's model, based on experimental observations, gives only a qualitative description of a possible phase separation process undergoing in the SDV [16]. In this work, we present the first quantitative test of a phase separation mechanism for diatom morphogenesis. As already mentioned above, the basic idea is that an organic component phase separates from an aqueous phase in the presence of the base layer within the SDV to form a quasi-two-dimensional emulsion of droplets around which a silica precursor (e.g. silicilic acid) can condense and form complex-fluid templates. Since the initial formation of organic droplets is seen to be relatively fast compared to the subsequent coalescence to form large droplets[1], we assume that the initial array of droplets provide an essentially static template for the condensation of the silica precursor. Nonetheless, we note that these two processes may be correlated, giving rise to cooperative effects. We therefore show that under these circumstances, our model of a phase-separating fluid in a confined quasi-two-dimensional environment, and in the presence of a certain degree of prepatterning (due to the base layer), is capable of generating templates which resemble almost any centric- or pennate-diatom valve. This will constitute the starting point for future studies, which will include the initial formation of the base layer (by, e.g. DLA [78]) and the coupling of phase separation with silica deposition and sintering (smoothing).

[1]The coalescence of droplets and the formation of large droplets is a an extremely slow process which is of considerable inherent interest [83].

5.2.1 *Physics of the model*

Due to the complexity, diversity, and species-specificity of frustule structures, a detailed physico-chemical description of diatom morphogenesis is precluded *a priori*. Hence, we have sought a generic model of the putative phase separation of a binary mixture in the presence of a prepatterning field.

The system is modelled as a confined quasi-two-dimensional incompressible binary mixture with fixed overall composition. Its dimensions are $L \times L \times l$ with $l \ll L$ and we assume the fluid composition to depend only on the lateral coordinates (x, y). Component o is organic (some organic macromolecules) and its volume fraction will be denoted $\phi_o(x, y)$, where as component a is essentially aqueous and with volume fraction $\phi_a(x, y)$. The order parameter of the system is chosen in the usual way for phase separation problems and corresponds to the local excess volume fraction of the organic material, namely $\phi(x, y) = \phi_o(x, y) - \phi_a(x, y)$, where $-1 \leq \phi(x, y) \leq 1$ at any time. The Hamiltonian of the system is

$$\mathcal{H}[\phi(x,y)] = \frac{l}{v_0}\int_0^L dx \int_0^L dy \left[\epsilon\left(-\frac{1}{2}\phi^2 + \frac{1}{4}\phi^4\right) + \kappa_1|\nabla\phi|^2 + \kappa_2(\nabla^2\phi)^2 + h\phi\right] \tag{5.1}$$

where v_0 represents a molecular volume. The first contribution to the Hamiltonian is the bulk free-energy term $\left(-\frac{1}{2}\phi^2 + \frac{1}{4}\phi^4\right)$ derived from the Landau theory of phase transitions and drives phase separation into coexisting phases with order parameter $\phi = \pm 1$ [23]. The terms multiplied by the factors κ_1 and κ_2 are contributions to the interfacial free-energy as described by Cahn and Hilliard [34, 84, 85]. It is important to point out that κ_1 is not the interfacial tension but is proportional to it, as is shown in Appendix A. In the final term, $h(x, y)$ models a local field arising from the presence of silica prepatterns on the base layer; $h > 0$ provides a repulsive field for the organic component and

$h < 0$ provides a repulsive field for the aqueous component. The dynamical equation for the order parameter is derived from the continuity equation $\partial\phi/\partial t + \nabla \cdot \mathbf{j} = 0$ and is equal to

$$\frac{\partial \phi}{\partial t} = \nabla \cdot (M \nabla \mu) \tag{5.2}$$

where $M(x, y)$ is the local mobility and $\mathbf{j} = -M\nabla\mu$ (Fick's law) is the flux of the order parameter ϕ, generated by gradients in the chemical potential. The local chemical-potential is defined as the functional derivative of the Hamiltonian (5.1)

$$\mu = \frac{\delta \mathcal{H}}{\delta \phi} = \epsilon\phi(\phi^2 - 1) - \kappa_1 \nabla^2 \phi + \kappa_2 \nabla^4 \phi + h. \tag{5.3}$$

Long-lived structures adopted by the fluid driven by the chemical potential (5.3) are generally sensitive to the average excess of organic component which is a conserved quantity measured by

$$\overline{\phi} = \frac{1}{L^2} \int \int \phi(x, y) dx dy. \tag{5.4}$$

With no field ($h = 0$), the phase-separating fluid assumes well known time-dependent structures which are long-lived droplets of organic and aqueous phases when $\overline{\phi} \ll 0$ and $\overline{\phi} \gg 0$ respectively; when $\overline{\phi} \simeq 0$ spinodal patterns emerge (Fig. 1.6).

5.2.2 *Computer methods*

Our simulations were performed by discretising Eq. (5.2) using a simple three-point, finite-difference algorithm [86] on a Cartesian grid 200×200 (or occasionally 300×300) with lattice spacing $\Delta = 1$, time step $dt = 0.01$, and periodic

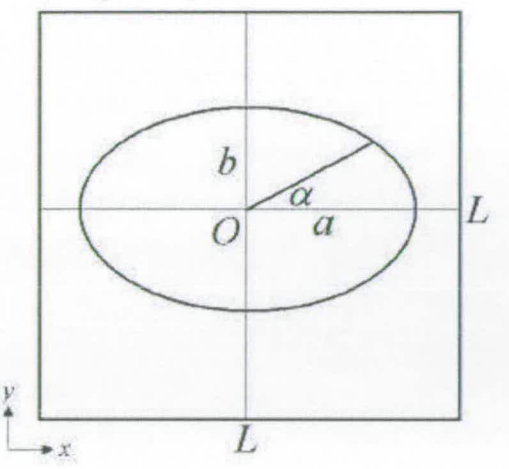

Figure 5.6: Schematic of the simulation cell. L is the box length, O the origin and a and b are the ellipse semi-axes.

boundary conditions [24] applied:

$$\frac{\partial M(x,y)}{\partial x} = \frac{M(x+1,y) - M(x-1,y)}{2\Delta} \tag{5.5}$$

$$\frac{\partial^2 \mu(x,y)}{\partial x^2} = \frac{\mu(x+1,y) - 2\mu(x,y) + \mu(x-1,y)}{\Delta^2} \tag{5.6}$$

$$\phi^{(t+1)}(x,y) = \phi^{(t)}(x,y) + dt\frac{\partial \phi^{(t)}(x,y)}{\partial t}. \tag{5.7}$$

The excess concentrations ϕ at each lattice site were initialised to $\phi = \phi_{\text{in}} \pm \delta\phi$, where $\delta\phi$ is a random number in the range $[-0.01, 0.01]$ and the values ϕ_{in} are shown in Tab. 5.1.

In all simulations, the perimeter of the diatom valve was taken to be an ellipse defined by $(x/a)^2 + (y/b)^2 = 1$, where a and b are the ellipse semi-axes ($a = b$ for centric diatoms). This boundary was established by allowing the mobility to depend on the position, interpolating smoothly between a value M_0 inside

the diatom valve to zero outside. For the mobility we used the convenient [2] "Fermi" expression

$$M(x,y) = \frac{M_0}{[1 + e^{(R-S)/W}]} \tag{5.8}$$

where W controls the width of the boundary, $S = 2a$ is the sum of the distances between any point on the ellipse and its two foci and R is the sum of the distances between a generic point of coordinates (x, y) and the two foci of the ellipse (see Fig 5.6).

[2] Different functions could have been chosen to avoid discontinuities in the mobility at the ellipse boundary.

Figure	Species	L/Δ	ϕ_{in}	ϕ_{ex}	κ_1^*	κ_2^*	a/Δ	b/Δ	W/Δ	$h(x,y)/\epsilon$	t/τ	Web reference
5.8(a)	*Arachnodiscus ehrenbergii*	200	−0.3	+0.0	0.2	-	70	70	1	$0.5\cos^{10}(8\alpha)$	3.00	[4]
5.8(b)	*Surinella linearis v. helvetica*	200	−0.65	−0.65	0.2	0.05	60	25	4	$0.4\cos^{2}(8\alpha)$	1000.00	[87]
5.8(c)	*Actinocyclus confluens*	200	−0.4	−0.2	0.4	-	90	90	1	$0.3\cos^{10}(\beta)$	10.90	[4]
5.7(a)	*Stictodiscus californicus*	200	−0.4	−0.3	0.6	-	40	40	4	-	30.00	[4]
5.7(b)	*Psammodiscus nitidus*	200	−0.4	−0.3	0.43	-	60	50	6	-	18.00	[75]
5.7(c)	*Aulacodiscus argus*	350	−0.3	−0.3	0.4	-	100	100	8	-	8.00	[4]
5.7(d)	*Actinoptychus undulatus*	200	−0.4	−0.4	0.3	-	60	60	6	$0.02\times[0.1+\sin^{2}(4\alpha)]/[0.1+\cos^{2}(4\alpha)]$	10.00	[4]
5.7(e)	*Actinoptychus campanulifer*	200	−0.3	+0.0	0.2	-	60	60	6	$1/[1+10\sin^{2}(3\alpha)]$	2.80	[4]
5.7(f)	*Cyclotella meneghiniana*	200	−0.5	−0.5	0.2	-	60	60	4	$0.4\cos^{2}(18\alpha)$	2800.00	[87]
5.7(g)	*Melosira sol*	200	−0.2	−0.2	0.5	-	60	60	6	$0.18\cos^{2}(26\alpha)$	20.00	[4]
5.7(h)	*Stictodiscus johnsonianus*	200	−0.3	−0.1	0.6	-	60	60	3	$0.06\cos^{2}(12\alpha)$	20.75	[4]
5.7(1)	*Arachnodiscus indicus*	200	−0.5	−0.5	0.4	-	50	50	1	$0.08\cos^{8}(8\alpha)+0.05\cos^{8}(4\beta)$	10.60	[4]
5.7(j)	*Stephanodiscus*	200	−0.5	−0.1	0.3	-	60	60	1	$0.15\sin^{4}(6\alpha)$	13.00	[88]
5.7(k)	*Psammodiscus*	200	−0.6	−0.6	0.1	-	40	40	6	$0.1\cos^{2}(4\alpha)$	50.00	[88]
5.7(l)	*Aulacodiscus kittonii*	200	−0.35	−0.1	0.5	-	70	70	1	$0.05\times[0.1+\cos^{2}(2\alpha)]/[0.1+\sin^{2}(2\alpha)]$	10.70	[4]
5.9(a)	*Cocconeis disculoides*	200	−0.45	−0.1	0.5	0.08	70	38	2.5	-	20.80	[75]
5.9(b)	*Achnanthes parvula*	200	−0.3	−0.3	0.5	0.1	60	5	4	-	35.00	[75]
5.9(c)	*Achnanthes parvula*	200	−0.3	−0.3	0.3	0.06	70	30	2	$0.1\sin^{2}(\alpha)$	9.00	[75]

Table 5.1: Reduced simulation parameters used to generate the structures shown in Figs. 5.7 and 5.9. In the case of concentric fields for centric diatoms, the angle $\beta = 2\pi\sqrt{x^2+y^2}/a$ where $a = b$ is the radius of the circular domain describing the diatom valve. $\overline{\phi}_{in}$ and $\overline{\phi}_{ex}$ are respectively the average order parameters inside and outside the diatom domain (Fig. 5.6).

Real quantity	**Reduced unity**
length	$length/\Delta$
energy	ϵ
time	$\tau = \Delta^2/\epsilon M_0$
interfacial energy parameter 1	$\kappa_1/\epsilon\Delta^2$
interfacial energy parameter 2	$\kappa_2/\epsilon\Delta^4$
prepattern field	$h(x,y)/\epsilon$

Table 5.2: Reduced parameters used in the simulations of the diatom frustule morphogenesis.

All the calculations were performed in dimensionless units (reduced units) as reported in Tab. 5.2. The choice of these units was made purely for computational convenience. In fact, we point out that a different choice could have been made, for instance defining units based on a natural lengthscale, such as the equilibrium width $\sqrt{\kappa_1/\epsilon}$ (Appendix A) of an interface separating coexisting phases.

All the parameters used in the simulations can be found in Tab. 5.1. The dynamical equation (5.2) was discretised using a time-step $dt = 0.01$ able to conserve $\overline{\phi}$ to within 1 part in 10^4.

5.3 Results and discussion

5.3.1 Centric diatoms

Fig. 5.7 shows a wide selection of real and simulated centric-diatom structures. We note that in the experimental images, the frustule colours arise from diffraction effects and are in no way an indication of pigmentation or silica staining. The simulated structures are instantaneous snapshots at times at which the organic patterns (black regions) can be considered as static (Fig. 5.10). The black regions denote high concentrations of organic material ($\phi \gg 0$) and represent possible templates for silica deposition as already mentioned. The white

regions ($\phi \ll 0$), instead, denote the aqueous domains where the silica will condense. In our simulations we observed that by modifying the composition of the fluid such that $\overline{\phi} \sim -0.3$, the organic macromolecules phase separate from the solution to form droplets in water. This situation corresponds to a relatively low volume fraction (~ 0.35) of organic components. As an example, Figs. 5.7 (a)-(c) show observed and simulated centric-diatom structures in which a disordered array of organic droplets are visible in absence of prepatterning field. The key variables here are the overall concentration of organic material $\overline{\phi}$, and the diameter of the circular domain a. These structures are, by themselves, not so surprising, but these images serve to illustrate complementarity of the pore structure of the diatom valve and the droplet structure of the fluid template.

5.3.2 *Pennate diatoms*

Fig. 5.9 includes some examples of pennate-valve diatoms. Pennate diatoms are often characterised by parallel rows of pores which go along the major axes of the frustule [77]. We found that these features could be reproduced by the inclusion of a weak $(\nabla^2\phi)^2$ term in the Hamiltonian in Eq. (5.1). These results are not at all surprising, because it is well known that in models of three-dimensional oil-water-surfactants mixtures the presence of a $(\nabla^2\phi)^2$ term stabilises modulated cubic (bicontinuous) phases [84, 85, 89, 90]. Similarly, in two dimensions, this term might (regulated by the parameter κ_2 in Tab. 5.1) be expected to favour the "square" arrays of pores shown in our simulated pennate structures. Experimentally, the presence of κ_2 in Eq. (5.1) may require the addition of an amphiphile to the organic and aqueous components in our model.

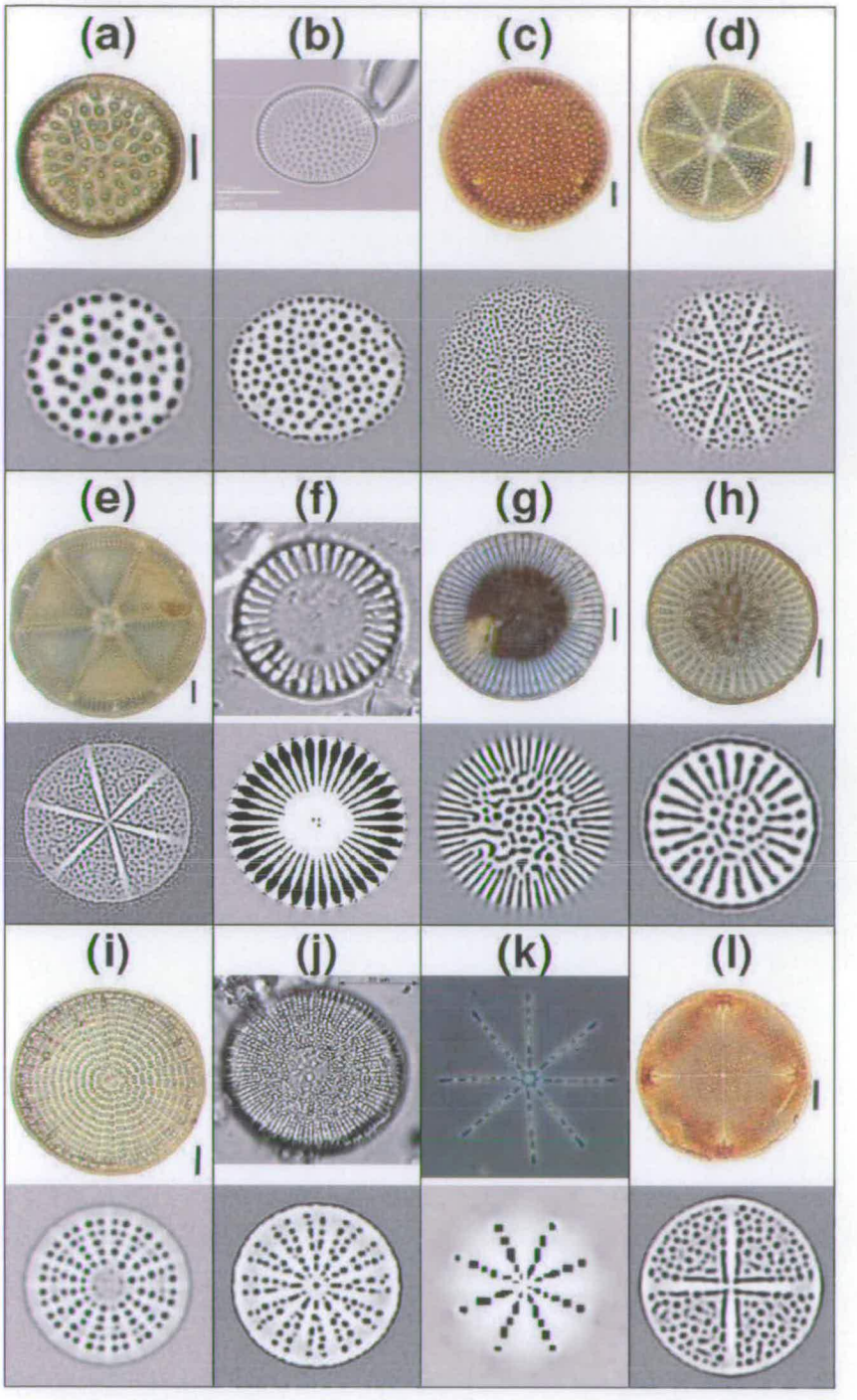

Figure 5.7: Experimental (upper) and simulated (lower) structures of centric diatoms: (a) *Stictodiscus californicus*, (b) *Psammodiscus nitidus*, (c) *Aulacodiscus argus*, (d) *Actinoptychus undulatus*, (e) *Actinoptychus campanulifer*, (f) *Cyclotella meneghiniana*, (g) *Melosira sol*, (h) *Stictodiscus johnsonianus*, (i) *Arachnodiscus indicus*, (j) *Stephanodiscus*, (k) *Psammodiscus*, (l) *Aulacodiscus kittonii*.In the simulated images, the dark regions correspond to organic-rich domains. Scale bars are 10 μm, except in (j) which is 20 μm. Experimental images are reproduced with permission from Refs. [4, 75, 87, 88].

5.3.3 *Prepatterns*

Fig. 5.8 shows some real and simulated diatom valves along with the corresponding prepatterning field $h(x, y)$ due to the base layer. Diatom-structures in Figs. 5.7 (d)-(l) clearly require radial prepatterning. In the prepatterning images of Fig. 5.8, the brighter regions denote higher free-energy for the organic component, and are therefore organic-poor regions. Figs. 5.7 (g) and (h) require additional comments. In these species - *Melosira sol* and *Stictodiscus johnsonianus*, respectively - the pore structure switches over from the droplets near the centre to spokes near the valve boundary. This crossover was seen to arise spontaneously in the simulations; near the centre the spacing between minima in the prepatterning field is small compared to the typical droplet size, and hence it is more favourable for the droplets to remain intact than for them to break up and drift into the minima. Near the perimeter, instead, the free-energy can be lowered by the droplets coalescing in the minima to form spokes[3].

Fig. 5.7 (i) represents a simulation snapshot for the species *Arachnodiscus indicus*, in which a concentric organization of pores is observed. This was mimicked in the simulations by adding an additional concentric field measured in terms of the parameter denoted as β in Tab. 5.1. Referring to Fig. 5.6, $\beta = 2\pi\sqrt{x^2 + y^2}/a$, where $a = b$ is the radius of the centric-diatom valve.

5.3.4 *Time dependence*

The majority of the simulated images presented in this chapter are "snapshots" of the fluid template at some particular late stage of the simulation. Fig. 5.10 shows the morphogenesis of *Melosira sol* captured at different time-steps during the simulation. In the figure, the diatom valve is seen to develop at different rates. Figure 5.10 (a) shows the initial, homogeneous state. At very short times

[3]The characteristic droplet size varies with the time by increasing like $t^{1/3}$ [83, 91].

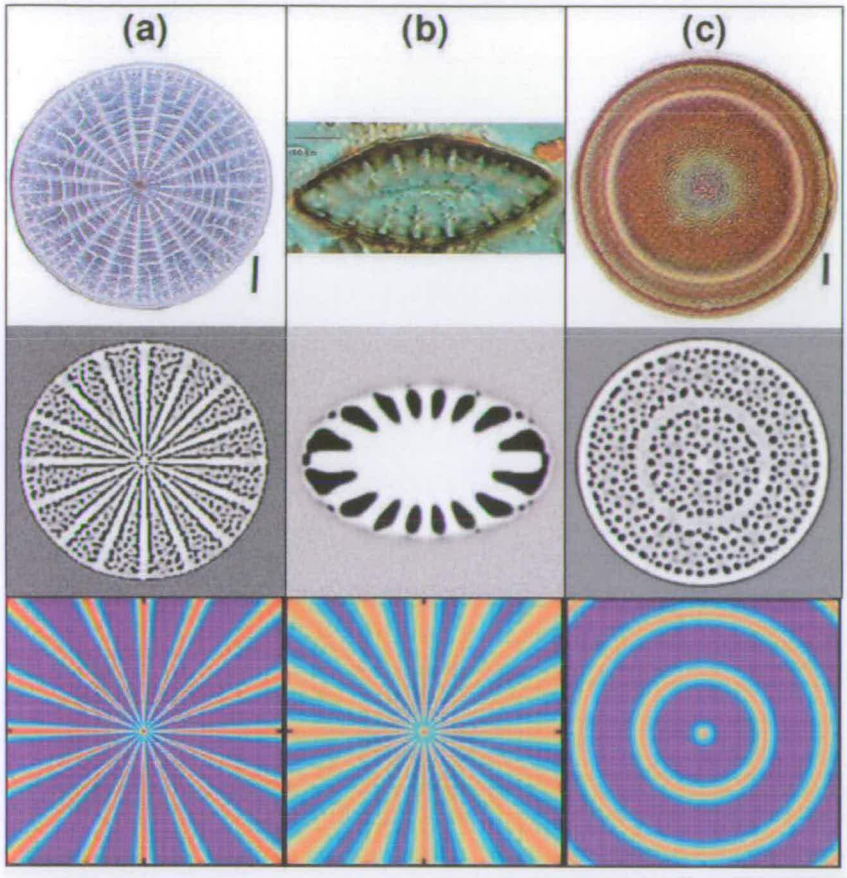

Figure 5.8: Experimental (top) and simulated (middle) images of diatom structures, and the prepattern field $h(x, y)$ (bottom) used into simulate each structure: (a) *Arachnodiscus ehrenbergii*, (b) *Surinella linearis v. helvetica*, (c) *Actinocyclus confluens*. In the simulated images, the dark regions correspond to organic-rich domains. Scale bars are 10 μm. Experimental images are reproduced with permission from Refs. [4, 87].

[Fig. 5.10 (b) and (c)], the inner part of the circular domain appears still homogeneous, though some spokes start appearing near the perimeter. At $t/\tau \sim 5$, two distinct regions are visible in the cell: spokes near the perimeter and vesicles in the interior. These fluid structures persist up to times beyond $t/\tau \sim 10$, and at times beyond $t/\tau \sim 20$ they appear to be essentially static. They therefore constitute a quasi-static template for a guided deposition of silica.

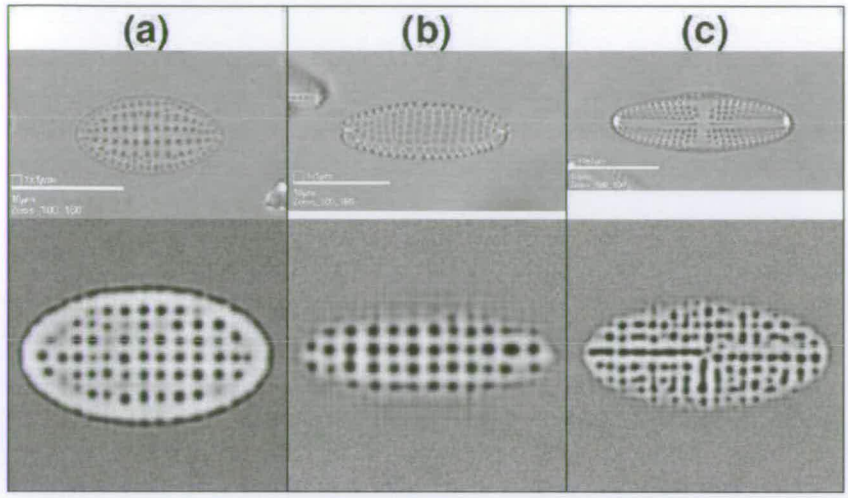

Figure 5.9: Experimental (upper) and simulated (lower) structures of pennate diatoms: (a) *Cocconeis disculoides*, (b) *Achnanthes parvula*, (c) *Achnanthes parvula*. In the simulated images, the dark regions correspond to organic-rich domains. Scale bars are 10 μm. Experimental images are reproduced with permission from Ref. [75].

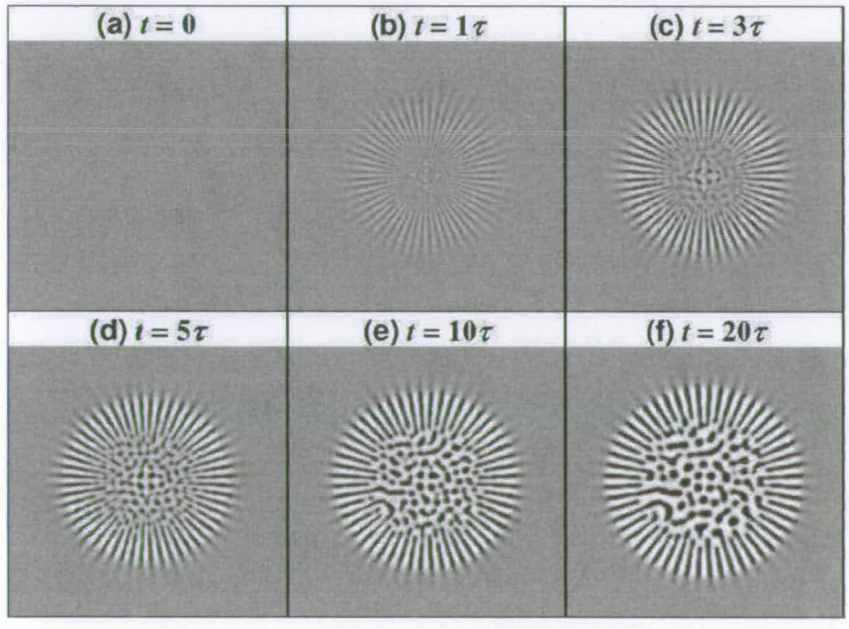

Figure 5.10: Simulation snapshots of the diatom *Melosira sol* at times (a) $t = 0$, (b) $t = 1\tau$, (c) $t = 3\tau$, (d) $t = 5\tau$, (e) $t = 10\tau$, and (f) $t = 20\tau$.

5.3.5 *Real parameters*

The simulation parameters in Tab. 5.1 were tuned heuristically to yield fluid structures mimicking a number of siliceous diatom patterns. Nonetheless, care

was taken in choosing reasonable physical values. As an example, we now estimate a typical real value for the parameter κ_1. Since $\sim 10^2$ grid points are typically used to represent a diatom dimension of ~ 10 μm, the grid spacing in real units is

$$\Delta \sim 10^{-7} \text{ m}. \tag{5.9}$$

The interfacial tension γ for typical immiscible fluids is normally several millijoules per square-metre [92] and the molecular volume v_0 can be roughly estimated considering organic macromolecules of dimensions of ~ 10 Å. Finally, the energy factor ϵ is unlikely to be much greater than $0.1\ k_BT$ where k_B is Boltzmann's constant and T is the temperature. The relationship between κ_1^* and γ is (as we show in Appendix A)

$$\kappa_1^* = \left(\frac{3\gamma v_0}{4\epsilon\Delta}\right)^2 \tag{5.10}$$

and combining the order-of-magnitude estimates reported above in Eq. (5.10), we obtain $\kappa_1^* \sim 0.5$, which is very close to the values chosen for our simulations (Tab. 5.1). It is strongly emphasised, however, that these are very rough estimates with the purpose of showing only that the reduced simulation parameters employed in this study can correspond to reasonable physical numbers.

The typical strength of the prepatterning field used in all the simulations can be deduced as the difference between the maximum and minimum field in Tab. 5.1, and is less than $0.5\ \epsilon$. With the assumption made above for ϵ, its value should be around $0.05\ k_BT$, which is extremely weak. As to the estimate of the typical time needed for the production of the patterns observed, we note that the Stokes-Einstein relationship for a spherical solute of radius $R \sim 10$ Å in a water-like solvent with viscosity $\eta \sim 10^{-3}$ Pa s, gives $D = k_BT/6\pi\eta R \sim 10^{-10}$ m^2 s^{-1}. Taking into account the previously estimated values for l and ϵ, we find

the basic unit of time $\tau \sim 10^{-3}$ s. The simulation times in Tab. 5.1, hence, corresponds to real times from tens to thousands of milliseconds. These underestimate experimental values probably due to macromolecular crowding within the SDV, and the effect of confinement which increases the mobility. However, for smaller values of the mobility M_0 , the basic unit of time $\tau \sim 1/M_0$ (Tab. 5.2) increases, making the reduced times reported in Tab. 5.1 correspond to biologically relevant timescales (seconds and minutes).

5.4 Conclusions

We have shown that a key stage of diatom morphogenesis can be described by a simple model of a phase-separating fluid in the presence of a weak prepatterning field, $h(x, y)$, mimicking the base layer observed in experiments. From a material-science perspective, it may be neither possible nor necessarily desirable to mimic the precise details of every diatom structure, therefore our model was chosen to be as simple as possible, although it captured the essential physico-chemical factors that drive pattern formation in diatoms. Nonetheless, our model is in no way specific to diatoms; on the contrary, it describes pattern formation as a result of phase separation in confined fluid mixtures and might serve as a generic model to help devise new strategies for synthesising porous nano-materials. For instance, fluid phase-separation could be carried out on lithographically etched surfaces, and the resulting patterned emulsion used as a template for the deposition of solid materials.

The examples in Figs. 5.8 - 5.9 show that the basic structural features of the diatom valve might be templated by long-lived domains in confined phase-separating fluids, controlled by the overall concentration of organic material, the interfacial tension γ (through the parameter κ_1 in Tab. 5.1), and a mild degree of prepatterning (mimicking the base layer). We emphasise that, where

present, the magnitude of the prepatterning field $h(x, y)$ needs be only about one tenth of the energy scale ϵ, and that the required values of κ_1 used in the simulations correspond to physically-reasonable values for the interfacial tension γ (Appendix A). We also observe that the square array of pores visible for the pennate diatoms in Fig. 5.9 was found favoured by the $(\nabla^2\phi)^2$ term in Eq. (5.1).

We stress again that the model here proposed describes a particular stage of diatom morphogenesis, however it is not specific at all to diatoms; the model, in fact, corresponds to a very general physical situation, that is the phase separation of immiscible fluids under confinement and local external fields. Hence, the predictions made by this model can be tested by experiments in which porous structures resembling those of diatom frustules can be reproduced in the laboratory.

From the biological perspective, this work is only a preliminary study. Future work should focus on combining the phase-separation process presented here, along with the diffusion-limited aggregation of silica nanoparticles thought to be responsible for the formation of the costae in the underlying base layer. Furthermore, the thickening of the frustule (vertical differentiation) and the condensation of silica should be accounted for simultaneously with phase separation. This work relies on the basic assumption that phase separation and silica condensation occur on distinct timescales, and that the fluid forms organic templates that are essentially static on the timescale for silica condensation. The assumption of a static fluid template is justified by experiments which suggest that the base layer is formed within minutes while vertical differentiation can take up to hours. Nonetheless, it should be possible to model these processes simultaneously without making any strong assumptions *a priori*.

Some diatom valves present hexagonal "close packed" arrays of pores [3]. It would be interesting to study the processes involved in the formation of these features. In Thompson's classic work *On Growth and Form* [93], the hexagonal array of pores is attributed to "electromagnetic vibrations" on the surface of the cell. There are other mechanisms by which these arrays might arise [77]: in two dimensions these have been observed in three-component, phase-separating, *reactive* fluids [94, 95] and phase-separating adsorbates [96].

The model was inspired by the results of experimental observations of diatom morphogenesis and by previous morphogenesis models. In particular, we have performed the first quantitative test of a phase-separation mechanism in the hope of shedding some light on a specific stage of the morphogenesis. On the other hand, our model does not offer any insight on the nature and extent of cellular control (such as the deposition of the base layer). To conclude, we mention that a mechanisms (based on a reaction-diffusion equation [97]) similar to the one which explains, for example, leopards' rosettes and tigers' stripes can be excluded *a priori* in the case of diatoms, because the structure of frustules within a given diatom-species colony are essentially identical, at least on the 100 nm scale.

It is hoped that this theoretical contribution will stimulate and devise new experiments in material an biological science to shed some light on diatom morphogenesis.

CHAPTER 6

Ensemble dependence of heat capacity in the 3D Ising model

6.1 Introduction

So far we have reported studies of self-assembly and phase-separation in the context of biomineralisation and used them to derive new theories and strategies for the controlled production of mesoporous materials. We employed different computer simulation techniques and we did not have to consider the effects of the statistical mechanical ensemble (Section 2.3) in which the simulations were carried out. For instance, in Chapter 3, we reported Brownian dynamics simulations of the self-assembly of small polypeptides called silaffins, implicated in the formation of silica structures in biominerals. These simulations were carried out in a constant-temperature, constant-volume ensemble, namely the canonical (NVT) ensemble. If the simulations had been run in different ensembles, we would have obtained the same results to within a precision of $\mathcal{O}(1/N)$, where N is the number of molecules.

There are situations in which simulations performed in different ensembles lead to more pronounced differences in the results. For example, a strong dependence of the simulation results on the ensemble has been observed in studies of finite-size systems near the vapour-liquid critical point [98–100]. It is important to recall, however, that the ensemble differences should vanish at the thermodynamic limit ($N \rightarrow \infty$) where all the ensembles lead to equivalent results [101]. We anticipate, however, that our simulation results point out a different scenario.

Daub *et al.* observed very strong finite-size effects in the constant-volume heat capacity in fluids with long-range interactions [98]. Monte Carlo simulations showed that grand-canonical (μVT) and canonical (NVT) calculations give very different heat capacity curves in the vicinity of the critical point. The grand-canonical curves exhibit very strong peaks near the critical temperature, whereas the canonical curves show no trace of peaks in the critical region. This effect is intuitively easy to understand if one considers that in the canonical ensemble the energy fluctuations are very small (and consequently C_V is small) because the local particle density does not fluctuate enough in the presence of long-range interactions. In the case of the grand-canonical ensemble, the number of particles is allowed to fluctuate and therefore the local particle density fluctuates enough to let the energy fluctuations become large enough to generate peaks in the heat capacity curves near the critical point [98]. Simulations of fluids with short-range interactions [99] and ionic fluids also showed the importance of the ensemble in which the simulations of finite-size systems are performed [102–104].

In order to help rationalise the results already seen in fluids, we will perform Monte Carlo simulations of the three-dimensional Ising model (Section 6.4) in

QUANTITY	CRITICAL EXPONENT	
Susceptibility	$\chi \sim t^{-\gamma}$	$t > 0$
Heat capacity	$C_V \sim t^{-\alpha}$	$t > 0$
Correlation length	$\xi \sim t^{-\nu}$	$t > 0$
Order parameter	$M \sim \lvert t \rvert^{\beta}$	$t < 0$

Table 6.1: Definition of the critical exponents. To each thermodynamic quantity is associated a critical exponent which describes that quantity near the critical point. $t = (T - T_c)/T_c$ is the reduced temperature.

a cubic lattice of finite size L. We will carry out a systematic finite-size scaling study of the constant-volume heat capacity C_V in the canonical and grand-canonical ensemble, and estimate the ensemble difference $\Delta C_V = C_V^{\mu VT} - C_V^{NVT}$. Furthermore, we will derive a finite-size scaling law for ΔC_V. The universality (Section 6.2) ensures that our results are applicable to any systems belonging to the same universality class.

6.2 Critical exponents and universality

In the vicinity of a critical second-order phase transition, most of the thermodynamic quantities can be described by a set of simple power laws. These laws are characterised by exponents called *critical exponents*. Tab. 6.1 defines the critical exponents associated with different thermodynamic quantities. According to the renormalization-group theory the values of the critical exponents should depend only on the spatial dimension, the symmetry of the order parameter, and the symmetry and range of interactions, but not on the detailed form and magnitude of the interactions [23, 105]. It is therefore possible to define *universality classes* which group all the second-order transitions characterised by the same values of the critical exponents. For instance, all three-dimensional systems in which the order parameter is scalar (e.g. the 3D Ising model) should have the same critical exponents. The values of the critical exponents for the different universality classes can be found in standard text books [21, 22].

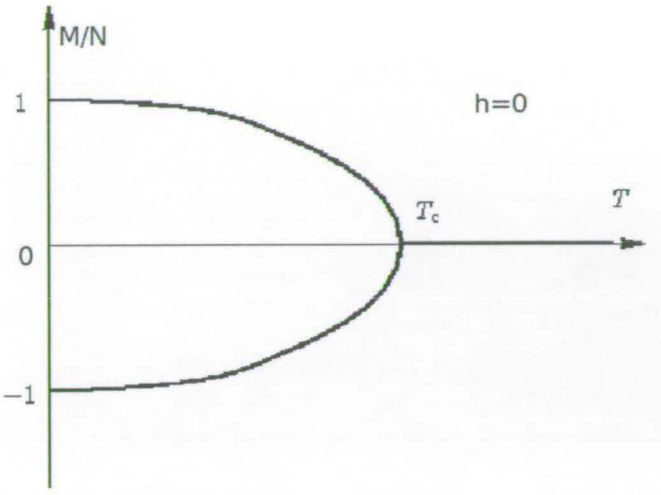

Figure 6.1: Schematic phase diagram of the Ising model (see Section 6.4) with no magnetic field applied ($h = 0$). The order parameter is defined as the magnetisation per spin $\phi = M/\mathcal{N}$ and the temperature is denoted by T. The critical point is at the apex of the bell-shaped curve (T_c), and corresponds to the value $M = 0$ of the magnetisation.

Furthermore, not all of the critical exponents are independent. For example, the susceptibility critical exponent γ is always of order of 2ν (where ν is the correlation length critical exponent), $\alpha+2\beta+\gamma = 2$ [21–23, 105], and $\nu d = 2-\alpha$, where d is the spatial dimensionality.

6.3 Finite-size effects and the heat capacity

The study of phase transitions involve the identification of the system order parameter, ϕ. In infinite-size systems (which are only theoretically possible), ϕ would not fluctuate and its distribution function could be effectively considered as a δ-function. This means that if the system was in a state defined by a certain value of ϕ, it would stay in the same state for long long time. In finite-size systems (real systems), the order parameter ϕ fluctuates (near the critical point the fluctuations become even as large as the order parameter) and so there is a non-trivial function $p(\phi)$ that can describe its probability function.

This means that in finite-size systems there are always states available that connect two ordered phases and through which the system can go to pass from one phase to the other. By increasing the system-size L, the probability of finding these connecting states gets lower and lower until it disappears at the thermodynamic limit [106].

In computer simulations and in experiments, the system size must, for practical reasons, be finite, and finite-size effects cannot be avoided. Far away from the critical point (that is for $L \gg \xi$, where ξ is the correlation length), at $T \neq T_c$, the distribution $p(\phi)$ is well approximated by a gaussian (or a number of connected gaussian peaks). Near the critical point ($T \simeq T_c$), the gaussian approximation is no longer valid and the function $p(\phi)$ becomes non-trivial. A solution to this "problem" is given by the finite-size scaling (FSS) theory [107].

According to the FSS theory, the probability function $p(\phi)$ assumes a universal form dictated by the ratio L/ξ, namely [107]

$$p(\phi, \xi, L) = L^{\beta/\nu} \overline{p}[\phi L^{\beta/\nu}, (L/\xi)^{1/\nu}] \tag{6.1}$$

where β and ν are the critical exponents defined in Tab. 6.1. In this way, it is possible to study critical phenomena even in small systems, calculate bulk thermodynamic properties, such as the critical temperature, and study the behaviour of important functions (such as the heat capacity C_V) near the critical point.

In what follows, we define the heat capacity and report its FSS scaling law at the critical point along with the FSS relation to extrapolate the critical temperature T_c from the position of the peaks of the heat capacity.

The heat capacity at constant volume is defined as the energy necessary to increase the system temperature by a certain temperature interval, namely

$$C_V = \left(\frac{\partial U}{\partial T}\right)_V . \tag{6.2}$$

If we define the reduced temperature as $t \equiv (T - T_c)/T_c$ (which is small in the proximity of T_c), according to the FSS theory, and similarly to (6.1), the heat capacity C_V scales like [21, 22, 106, 107]

$$C_V = L^{\alpha/\nu}\overline{C}[(L/\xi)^{1/\nu}] = L^{\alpha/\nu}\overline{C}(tL^{1/\nu}) \tag{6.3}$$

where $\overline{C}$ is the universal scaling function. In the Ising model (Section 6.4), the scaling function $\overline{C}$ can be derived from the probability distribution of the energy per spin. According to Eq. (6.3), the heat capacity calculated in finite-size systems presents a peak in the vicinity of T_c [107, 108]. Upon increasing the dimensions of the system, the position of the peak (signaling an "apparent" finite-size critical temperature, $T_c^{(L)}$) should shift towards the bulk critical temperature $T_c^{(\infty)}$ and the height of the peak should diverge according to well-known scaling laws. The value of the apparent critical temperature $T_c^{(L)}$, where L is the dimension of the system, deviates from the "bulk" critical temperature $T_c^{(\infty)}$ according to the following scaling law [106]

$$T_c^{(L)} - T_c^{(\infty)} \sim L^{-1/\nu} \tag{6.4}$$

where ν is the appropriate correlation-length exponent (see Tab. 6.1). The relation (6.4) is intuitively easy to understand. By recalling that in a finite-size system the critical point is characterised by the condition ($\xi \sim L$), and that $\xi \sim t^{-\nu}$, we can write

$$t = \frac{T_c^{(L)} - T_c^{(\infty)}}{T_c^{(\infty)}} \sim L^{-1/\nu} \tag{6.5}$$

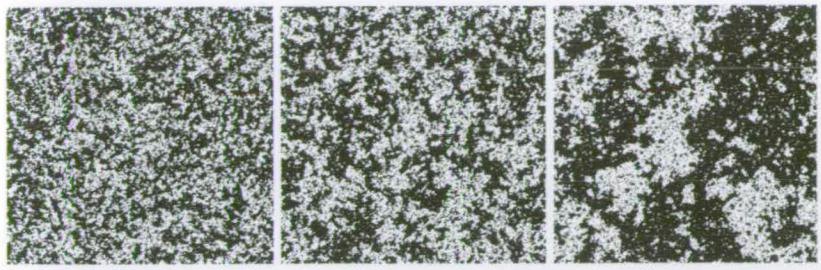

Figure 6.2: Simulation snapshots of a 3D ferromagnetic Ising model at different temperatures $\beta = 1/k_B T$. From left to right: $\beta = 0.2$ ($T \gg T_c$), $\beta = 0.21$ ($T > T_c$), and $\beta = 0.219$ ($T \simeq T_c$). Images reproduced from Ref. [110].

which is equivalent to Eq. 6.4. For three-dimensional Ising-like critical points $\nu = 0.630$ [21, 109]. A detailed description of the critical exponents and finite-size scaling analysis is given in Refs. [21, 22, 106, 107].

6.4 3D Ising model

The Ising model is defined on a discrete cubic lattice made of $\mathcal{N}$ sites each of them carrying a variable called *spin* (s_i) which can take on the value $+1$ or -1. The sum of all the spins ($M = \sum_{i=1}^{\mathcal{N}} s_i$) is called the magnetisation, and the order parameter is defined as $\phi = M/\mathcal{N}$. The spins s_i interact with nearest neighbors. The Hamiltonian of the system in the absence of an external magnetic field h is [18]

$$\mathcal{H} = -J \sum_{\langle i,j \rangle} s_i s_j, \tag{6.6}$$

where J is the coupling constant and $\langle i, j \rangle$ denotes a sum extended only to nearest-neighbors. If $J > 0$, the model is *ferromagnetic* (it is energetically favorable for neighboring spins to be aligned), whereas $J < 0$ defines an *antiferromagnetic* Ising model. $J = 0$ defines non-interacting spins. In order to describe the Ising model, let us consider the ferromagnetic case ($J > 0$) and its phase diagram in Fig. 6.1. At temperatures much higher than the critical temperature ($T \gg T_c$), all the spins are randomly oriented (the clusters of like spins

ISING MODEL	*3D FLUID*
T (temperature)	T (temperature)
M (magnetisation)	N (number of particles)
$\mathcal{N}$ (number of lattice sites)	V (volume)
h (external magnetic field)	μ (chemical potential)
E (energy)	E (energy)

Table 6.2: Comparison between thermodynamic quantities in a 3D Ising model and in a 3D fluid.

are very small), there is no order, and hence the order parameter $\phi = M/\mathcal{N}$ is zero (Fig. 6.2). At the temperature $T \simeq T_c$ (where T_c is the critical temperature), there is an order-disorder phase transition (there is a broad distribution of clusters). At this point some order sets in so that for temperatures $T < T_c$ the order parameter is different from zero (Figs. 6.1 and 6.2). At very low temperatures ($T \simeq 0$), all the spins are aligned and the system is in one of the ordered states described by the order parameter $\phi \pm 1$ (Fig. 6.1) [18, 23, 32].

While the thermodynamic functions of the systems described by the Hamiltonian in Eq. (6.6) can be found easily in one dimension [24, 27], the two-dimensional Ising model requires a very complicated solution which was given in 1944 by Onsager [26]. The three-dimensional Ising model has not yet been solved exactly, although accurate approximations are available [24, 27].

We recall that the results obtained for the 3D Ising model are applicable to a simple three-dimensional fluid provided it belongs to the same universality class, because at the critical point the correlation length ξ diverges (Tab. 6.1) and hence the microscopic details (such as the lattice spacing or atomic dimensions) become irrelevant (Section 6.2). In Tab. 6.2 we associate to each thermodynamic quantity in the 3D Ising model, a corresponding quantity in a 3D fluid. All the universal critical properties that will be devised from a detailed study of the 3D Ising model, will therefore be valid for a simple 3D fluid.

Throughout this chapter, on the basis of Tab. 6.2, the canonical ensemble for an Ising model will be denoted $M\mathcal{N}T$, whereas the grand-canonical ensemble will be denoted $h\mathcal{N}T$.

6.4.1 Heat capacities in the Ising model

Let us consider a specific configuration of spins $\Gamma = \{s_1, s_2, ..., s_{\mathcal{N}}\}$. The grand-canonical ($h\mathcal{N}T$) heat capacity can be written as

$$C_{h\mathcal{N}T} = k_B\beta^2 \left[\langle \mathcal{H}^2 \rangle - \langle \mathcal{H} \rangle^2\right] \tag{6.7}$$

where $\beta = 1/k_BT$ (not to be confused with the order-parameter exponent) and $\mathcal{H}$ is the Hamiltonian (6.6). Considering the grand-canonical partition function

$$\Xi = \sum_{\Gamma} \exp(-\beta\mathcal{H}) \tag{6.8}$$

and the standard thermodynamic equation [21]

$$\langle \mathcal{H} \rangle = -\frac{\partial \ln \Xi}{\partial \beta}, \tag{6.9}$$

the heat capacity (6.7) can be rewritten in the following way

$$C_{h\mathcal{N}T} = k_B\beta^2 \frac{\partial^2 \ln \Xi}{\partial \beta^2}. \tag{6.10}$$

Similarly, the heat capacity in the canonical ensemble or "constant magnetization" ($M\mathcal{N}T$) ensemble is

$$C_{M\mathcal{N}T} = k_B\beta^2 \frac{\partial^2 \ln Q}{\partial \beta^2}, \tag{6.11}$$

where

$$Q = \sum_{\Gamma} \delta(M, 0) \exp(-\beta \mathcal{H}) \tag{6.12}$$

is the canonical partition function, for which the sum over Γ includes only those configurations for which $M = 0$ [1]. The canonical partition function (6.12) can be related to the grand-canonical one (6.8) according to

$$Q = \frac{\sum_{\Gamma} \delta(M, 0) \exp(-\beta \mathcal{H})}{\sum_{\Gamma} \exp(-\beta \mathcal{H})} \cdot \sum_{\Gamma} \exp(-\beta \mathcal{H}) = p_{h\mathcal{N}T}(0) \cdot \Xi, \tag{6.13}$$

where $p_{h\mathcal{N}T}(0)$ represents a particular value of the magnetisation probability distribution function. Substituting (6.13) into (6.11) we can calculate the ensemble difference in the heat capacity per spin, that is

$$\Delta C_V = \frac{C_{h\mathcal{N}T} - C_{M\mathcal{N}T}}{L^3 k_B} = \frac{\beta^2}{L^3} \cdot \frac{\partial^2 \ln p_{h\mathcal{N}T}(0)}{\partial \beta^2}. \tag{6.14}$$

This result is a significant one, because $p_{h\mathcal{N}T}(M)$ is a universal function [106, 111, 112] at the critical point (Section 6.3); that is, it has got a scaling form from which the dependence of the system size L can be factored out. Taking into account this latter observation, in the next section we will derive a scaling form for the difference ΔC_V.

6.4.2 *Scaling expression for ΔC_V*

The magnetisation probability distribution function $p(M, L, t)$ near the critical point of a finite-size system has the well-known scaling form [111]

$$p(M, L, t) = L^{\beta/\nu} \overline{p}(M L^{\beta/\nu}, t L^{1/\nu}), \tag{6.15}$$

[1] The value $M = 0$ corresponds to the critical magnetisation. This is the analogue of the critical isochore in fluids (see Fig. 6.1).

where $\overline{p}(ML^{\beta/\nu}, tL^{1/\nu})$ is a universal scaling function[2] depending only on the boundary conditions, and β and ν are the magnetisation and correlation-length critical exponents, respectively [22, 111]. Substituting Eq. (6.15) into Eq. (6.14) we obtain

$$\Delta C_V = \frac{\beta^2}{L^3} \cdot \frac{\partial^2}{\partial \beta^2} \left[\ln L^{\beta/\nu} \overline{p}(0, tL^{1/\nu}) \right] \tag{6.16}$$

where the exponent β of the dimension L is the magnetisation critical exponent and it is not to be confused with $\beta = 1/k_B T$ appearing in the derivatives. The derivative in Eq. (6.16) is therefore equivalent to

$$\Delta C_V = \frac{\beta^2}{L^3} \cdot \frac{\partial^2}{\partial \beta^2} \ln \overline{p}(0, tL^{1/\nu}) \tag{6.17}$$

because the term proportional to $L^{\beta/\nu}$ is independent of temperature. To proceed, we define the variable $x = tL^{1/\nu}$, where $t = \beta_c/\beta - 1$ is the reduced temperature. The first derivative of the natural logarithm of the scaling function $\overline{p}$ is

$$\frac{\partial}{\partial \beta} \ln \overline{p}(0, x) = \frac{\partial t}{\partial \beta} \frac{\partial x}{\partial t} \frac{\partial \ln \overline{p}(0, x)}{\partial x}. \tag{6.18}$$

In Eq. (6.18), the term

$$\overline{p_1} = \frac{\partial \ln \overline{p}(0, x)}{\partial x} \tag{6.19}$$

being a function only of x, is a universal scaling function in the vicinity of the critical point. The first derivative (6.18), by an appropriate substitution of variables, can hence be rewritten

$$\frac{\partial}{\partial \beta} \ln \overline{p}(0, tL^{1/\nu}) = -\frac{\beta_c}{\beta^2} L^{1/\nu} \overline{p}_1(0, tL^{1/\nu}). \tag{6.20}$$

[2]It is important to note that $tL^{1/\nu} \propto (L/\xi)^{1/\nu}$, and provides a physically meaningful measure of the "distance" from criticality. The critical point in finite-size systems is characterised by the condition $\xi \sim L$.

Similarly, the second derivative of the natural logarithm of the scaling function $\overline{p}$ is

$$\frac{\partial^2}{\partial\beta^2}\ln\overline{p}(0,x) = \frac{2\beta_c}{\beta^3}L^{1/\nu}\overline{p}_1(0,x) - \frac{\beta_c}{\beta^2}L^{1/\nu}\frac{\partial t}{\partial\beta}\frac{\partial x}{\partial t}\frac{\partial\ln\overline{p}_1(0,x)}{\partial x} \tag{6.21}$$

where

$$\overline{p}_2 = \frac{\partial\ln\overline{p}_1(0,x)}{\partial x} \tag{6.22}$$

is a universal scaling function in the vicinity of the critical point. By substituting Eq. (6.21) into Eq. (6.17) and by appropriately changing the variables, the heat capacity difference can be rewritten as

$$\Delta C_V = 2\left(\frac{\beta_c}{\beta}\right)\overline{p}_1(0,tL^{1/\nu})L^{1/\nu-3} + \left(\frac{\beta_c}{\beta}\right)^2\overline{p}_2(0,tL^{1/\nu})L^{2/\nu-3}. \tag{6.23}$$

In Eq. (6.23) the dependence from L can be factored out to obtain a scaling function for the heat capacity difference ΔC_V, that is

$$\Delta C_V \approx a_1\, L^{1/\nu-3} + a_2\, L^{2/\nu-3}. \tag{6.24}$$

The term $L^{1/\nu-3}$ should vanish as the system size L becomes infinite, and hence the difference (6.23) becomes

$$\Delta C_V \approx \left(\frac{\beta_c}{\beta}\right)^2\overline{p}_2(0,tL^{1/\nu})L^{2/\nu-3}. \tag{6.25}$$

The universal scaling function $\overline{p}_2$ is

$$\overline{p}_2(0,tL^{1/\nu}) = \frac{\Delta C_V}{L^{2/\nu-3}}\left(\frac{\beta}{\beta_c}\right)^2 \tag{6.26}$$

and hence plots of the left-hand side versus $tL^{1/\nu}$ for different L should collapse on to a single curve near $t = 0$. Incidentally, the exponent $2/\nu-3$ is very close to

the value of the critical exponents ratio α/ν [22]. Eqs. (6.25) and (6.26) are true as long as the system size L is relatively large. These assumptions are tested in Section 6.6.

6.5 Computer techniques

The MC algorithm employed in our simulations samples uniformly a number of discrete values of temperatures in the range of interest (e.g. near criticality) to collect ensemble averages at each temperature separately [113]. In a similar fashion to the parallel tempering MC scheme [113, 114], this method uses two types of moves: an energy move (by spin flipping) at a fixed temperature and a temperature move at a fixed energy, allowing the exploration of all the thermal states in a single simulation run. This method therefore efficiently enhances the exploration of phase space of a system especially in the presence of configurations separated by high free-energy barriers.

We point out that our simulations could have also been run using the general Wang-Landau [25] algorithm, instead of the MC scheme to be described below. However, previous works [115, 116] suggest that the Wang-Landau algorithm requires a long convergence time for large systems making the simulations very long. Furthermore, the Wang-Landau method does not improve on the statistical error after the factor f has reached a certain value. This could constitute a problem when simulating large systems. Alternatively, a standard Metropolis algorithm could have also been employed in this study, but different simulations at different temperatures would be required making the study less efficient.

6.5.1 Uniform sampling of β

In this section we show how to obtain a biased MC scheme [27, 113, 116] that samples the inverse temperature β uniformly for the Ising model (6.4) in the grand-canonical ensemble. Let us consider a specific configuration of spins $\Gamma = \{s_1, s_2, ..., s_{\mathcal{N}}\}$ at the temperature $\beta = 1/k_B T$, and denote $p(\Gamma, \beta)$ the corresponding probability distribution function. If the grand-canonical partition function is

$$\Xi(h, \mathcal{N}, \beta) = \sum_{\Gamma} \exp\left[-\beta \mathcal{H}(\Gamma)\right], \tag{6.27}$$

then the probability of observing a configuration Γ at the inverse temperature β is [18]

$$p(\Gamma, \beta) = \frac{\exp\left[-\beta \mathcal{H}(\Gamma)\right]}{\Xi(h, \mathcal{N}, \beta)}. \tag{6.28}$$

Now consider an ensemble where β is allowed to fluctuate. Its partition function can be written as

$$\Psi(h, \mathcal{N}) = \sum_{\Gamma} \sum_{\beta} \exp\left[-\beta \mathcal{H}(\Gamma)\right], \tag{6.29}$$

and the probability of a microstate is

$$p(\Gamma, \beta) = \frac{\exp\left[-\beta \mathcal{H}(\Gamma)\right]}{\Psi(h, \mathcal{N})}. \tag{6.30}$$

The macrostate probability of observing a particular state characterised by the inverse temperature β irrespective of the configuration Γ is obtained by summing Eq. (6.30) over all possible configurations, namely

$$p(\beta) = \sum_{\Gamma} p(\Gamma, \beta) = \sum_{\Gamma} \frac{\exp\left[-\beta \mathcal{H}(\Gamma)\right]}{\Psi(h, \mathcal{N})} = \frac{\Xi(h, \mathcal{N}, \beta)}{\Psi(h, \mathcal{N})}. \tag{6.31}$$

The biased microstate probability which gives rise to uniform sampling of all the inverse temperatures is the ratio of Eqs. (6.30) and (6.31)

$$p_{\text{bias}}(\Gamma,\beta) = \frac{p(\Gamma,\beta)}{p(\beta)} = \frac{\exp\left[-\beta\mathcal{H}(\Gamma)\right]}{\Xi(h,\mathcal{N},\beta)} \tag{6.32}$$

because then

$$p_{\text{bias}}(\beta) = \sum_{\Gamma} p_{\text{bias}}(\Gamma,\beta) = 1. \tag{6.33}$$

The detailed balance condition that accounts for the microstate probability (6.32) is [27]

$$p_{\text{bias}}(\Gamma_o,\beta_o)\text{acc}(o\to n) = p_{\text{bias}}(\Gamma_n,\beta_n)\text{acc}(n\to o), \tag{6.34}$$

where (Γ_o,β_o) and (Γ_n,β_n) are the old state and the new state (generated without bias) respectively, and $\text{acc}(o\to n)$ is the probability of accepting a trial move from state o to state n. The Metropolis solution to Eq. (6.34) is

$$\text{acc}(o\to n) = \min\left[1, \frac{p_{\text{bias}}(\Gamma_n,\beta_n)}{p_{\text{bias}}(\Gamma_o,\beta_o)}\right]. \tag{6.35}$$

or equivalently

$$\text{acc}(o\to n) = \min\left[1, \frac{\Xi(h,\mathcal{N},\beta_o)}{\Xi(h,\mathcal{N},\beta_n)}\cdot\frac{\exp\left[-\beta_n\mathcal{H}(\Gamma)\right]}{\exp\left[-\beta_o\mathcal{H}(\Gamma)\right]}\right]. \tag{6.36}$$

We performed Metropolis Monte Carlo simulations of the three-dimensional Ising model in which the ratio of the partition functions Ξ in Eq. (6.36) is estimated on the fly via a Wang-Landau scheme as explained in detail in Section 6.5.2. The scheme reported above allows one to estimate the grand-canonical heat capacity $C_V^{h\mathcal{N}\beta}$ with great accuracy as shown in Section 6.6. Similarly, the constant-magnetisation heat capacity $C_V^{M\mathcal{N}\beta}$, and hence the difference ΔC_V, can be calculated by replacing Eq. (6.27) with the appropriate partition function.

6.5.2 The Monte Carlo algorithm

The MC algorithm employed in this study implements the acceptance-rejection rule (6.36) by performing a random walk in the β-space at fixed energy [113]. During the random walk a histogram $H(\beta)$ is accumulated to keep track of the states visited making sure that each possible thermal state has been visited approximately the same number of times. The value of the partition function $\Xi(\beta)$ is then modified by a multiplicative factor f and used to re-perform a random walk in the inverse-temperature space[3]. For each inverse-temperature visited, independent ensemble averages are calculated.

The scheme is as follows:

- the system is prepared in a random spin configuration;
- a discrete inverse-temperature range in which to carry out the simulation is chosen;
- at the outset, the value of the partition function $\Xi(\beta)$ is unknown, so we need to make an initial guess for it. The simplest choice is $\Xi(\beta) = 1\ \forall(\beta)$ in the chosen range;
- an initial value for the modification factor f_0 is chosen;
- a spin is picked randomly and its state changed. The trial flip is accepted with probability

$$p(E_o \rightarrow E_n) = \min\left(1, \exp\left[-\beta(E_n - E_o)\right]\right), \tag{6.37}$$

  where E_o and E_n are respectively the energies before and after the spin-flip. In other words, if $E_n \leq E_o$, the new state E_n is always accepted, otherwise, it is accepted conditionally with probability $\exp\left[-\beta(E_n - E_o)\right]$;
- the procedure is repeated for all spins (this constitutes a MC cycle);

[3] $\Xi(\beta)$ is the abbreviation of $\Xi(h, \mathcal{N}, \beta)$ for $h = 0$ and $\mathcal{N} = L^3$.

- every MC cycle a temperature swap ($\beta_o \rightarrow \beta_n$) at the current energy is attempted and the move accepted with probability (6.36);
- if the new state is accepted, the partition function $\Xi(\beta_n)$ is updated by multiplying it by a factor $f > 1$ (namely $\Xi(\beta_n) \rightarrow \Xi(\beta_n) \times f$) and the histogram H is also modified to the value $H(\beta_n) \rightarrow H(\beta_n) + 1$;
- alternatively, if the trial move is rejected, the existing partition function is modified according to $\Xi(\beta_o) \rightarrow \Xi(\beta_o) \times f$, along with the corresponding entry in the histogram H, namely $H(\beta_o) \rightarrow H(\beta_o) + 1$;
- these steps are repeated till the histogram $H(\beta)$ is flat;
- if H is flat, the the modification factor f is reduced ($f \rightarrow \mathcal{F}(f)$, where $\mathcal{F}$ is an arbitrary decreasing function of f) and H reset to zero;
- a new MC cycle is started;
- statistical averages (and therefore C_V) are calculated only when f reaches an arbitrary final value f_{final};
- the procedure is repeated for a large number of MC cycles.

Monte Carlo simulations in the canonical ($M\mathcal{N}T$) ensemble were performed according to the same scheme, but flipping two opposite spins per time in order leave the magnetisation unchanged, and equal to zero.

A number of observations on the steps mentioned above need to be made. In the simulations, it is always preferable to work with small numbers[4], so what we actually store in the computer is the logarithm of the value of the partition function, namely $\ln \Xi(\beta)$, which implies a modified update expression that reads $\ln \Xi(\beta) \rightarrow \ln \Xi(\beta) + \ln f$. The choice of the initial modification factor f_0 and of the function $\mathcal{F}$ is also important. If f_0 is too small, the system will spend a very long time visiting all the possible configurations. On the other hand, a large value of f_0 might lead to prematurely "converged" results and large

[4]The value of the partition function can easily become large leading to arithmetic overflow.

statistical errors. The function $\mathcal{F}$ is chosen arbitrarily as long as it decreases monotonically. A good function would be $\mathcal{F} = f^{1/n}$, where n is chosen according to the accuracy we want to obtain and the available CPU time. Finally, it is important to check periodically the flatness of the histogram H. This task is achieved by making sure that every entry in the histogram H has been filled not less than $x\%$ of the average $\langle H(\beta) \rangle$. The percentage x is chosen according to the accuracy needed in the simulations. In our simulations we chose $x = 98\%$.

6.6 Results and discussion

This section is organised as follows. In the first part we report a standard finite-size scaling (FSS) analysis of a three-dimensional Ising model in cubic boxes of side $L = 20, 30, 40, 50$, and 60 in order to test the algorithms reported in Section 6.5. In the second part, we analyse the ensemble difference ΔC_V and test its universal scaling function at the critical temperature as predicted in Section 6.4.2.

6.6.1 Finite-size scaling (FSS) analysis

We performed independent Monte Carlo simulations of the 3D Ising model in the grand-canonical ensemble ($h\mathcal{N}T$) and in the canonical ensemble ($M\mathcal{N}T$). In this latter case the simulations were carried out by flipping two randomly chosen opposite spins per time in order to leave the magnetisation unchanged after the move. In this case, the simulations were conducted at the critical magnetisation, $M = 0$.

An important quantity to analyse in FSS is the fourth-order Binder cumulant [117]. The fourth-order magnetisation cumulant is defined as

$$P_M = 1 - \frac{\langle M^4 \rangle}{3\langle M^2 \rangle^2} \tag{6.38}$$

and its value at the critical point does not depend on the system size L but assumes a non-trivial value [106]. Thus, the behavior of the cumulant P_M makes it very useful for obtaining estimates of T_c, which can be read at the intersection point of the cumulant curves in a graph where we plot P_M against the temperature T for different system sizes. In this work, we calculate the fourth-order energy cumulant P_E [117] instead, because the computation of P_M in the constant-magnetisation ensemble would make no sense.

The fourth-order energy cumulant [117] is defined by

$$P_E = 1 - \frac{\langle E^4 \rangle}{3\langle E^2 \rangle^2}. \tag{6.39}$$

This quantity was originally introduced to discriminate between a first and a second-order phase transition since it assumes a non-trivial value at a first-order transition [118–120]. At a second-order transition in a finite-size system, the cumulant presents a minimum at the apparent critical temperature $T_c^{(L)}$ whose depth should tend to $\frac{2}{3}$ at the thermodynamic limit. Away from the critical point, P_E should tend to $\frac{2}{3}$ [117, 118].

In Fig. 6.3 we show the fourth-order energy cumulants (6.39) for systems of different size L in the grand-canonical ensemble. Fig. 6.4 shows the fourth-order energy cumulant as calculated via computer simulations in the canonical ensemble. The canonical curves present different features compared to their grand-canonical counterparts: the apparent critical temperatures seem to be reduced as well as the depth of the minima. This discrepancy is mainly due to the small dimension of the simulation boxes employed in this study. The difference should vanish as the box size L approaches infinity. In Fig. 6.5, we plot the depths of the Binder-cumulant minima as functions of the box length. As stated before, these curves tend to the trivial value $\frac{2}{3}$ because of the presence of a second-order transition.

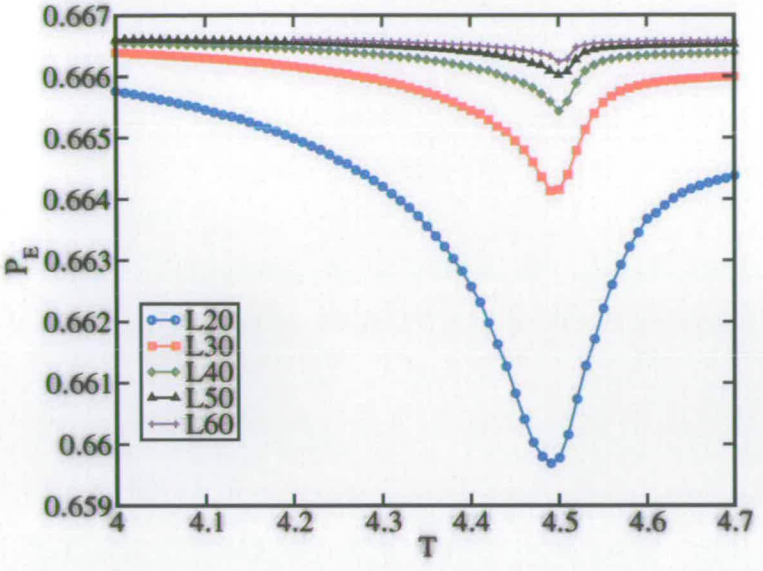

Figure 6.3: Fourth-order Binder cumulant for systems of different size L in the grand-canonical ensemble. The curves present a minimum at the apparent critical temperature $T_c(L)$. As the dimension L of the system increases, the value of $P_E(T_c)$ tends to 2/3 as predicted for a second-order transition.

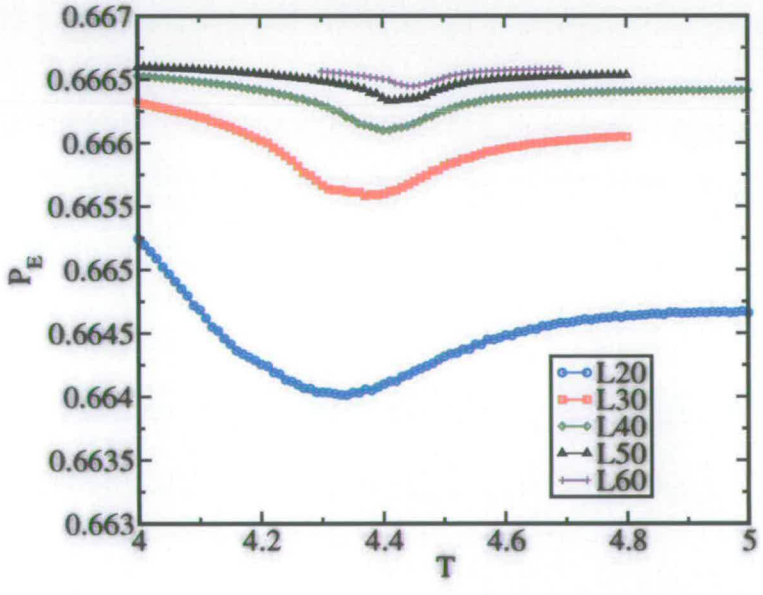

Figure 6.4: Fourth-order Binder cumulant for systems of different size L in the canonical ensemble. The curves present a minimum at the apparent critical temperature $T_c(L)$. As the dimension L of the system increases, the value of $P_E(T_c)$ tends to 2/3 as predicted for a second-order transition.

The apparent critical temperatures corresponding to the positions of the minima in the Binder cumulants follow the scaling relation (6.4). This relation

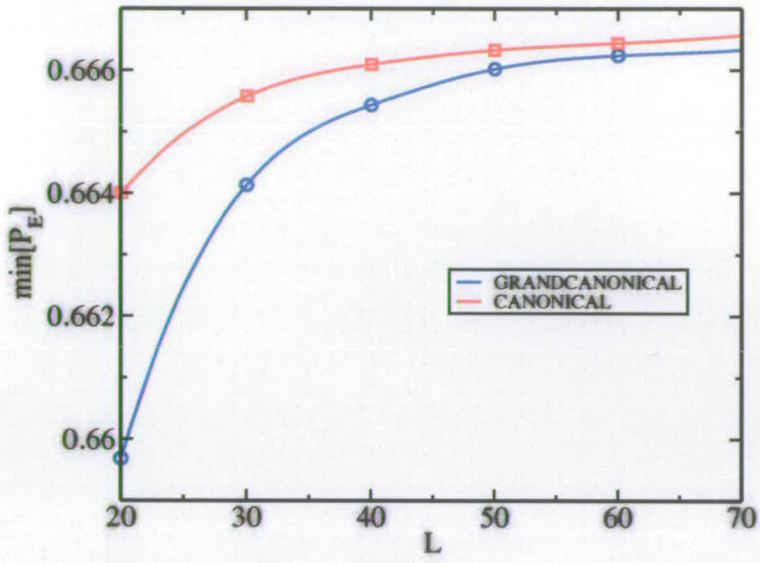

Figure 6.5: Fourth order cumulant minima as a function of the box length L. The curves tend to the value 2/3 at a second-order transition. The continuous lines are best fits of the experimental points.

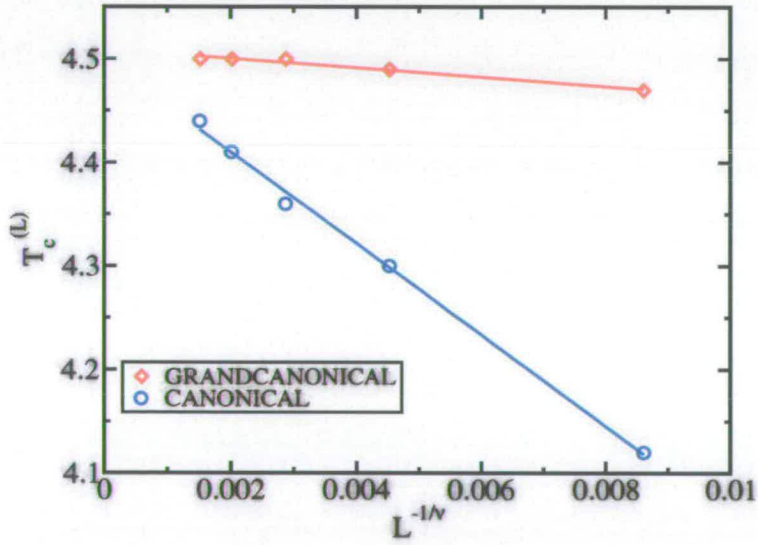

Figure 6.6: Estimation of the bulk critical temperature from the heat capacity. The red squares are simulation results for the apparent critical temperature in the grand-canonical ensemble; the blue circles are estimations in the canonical ensemble. The lines are best-fit curves of the experimental points. The y-intercepts of these lines give an estimation of the bulk critical temperatures in both ensembles.

is tested in Fig. 6.6 by plotting $T_c^{(L)}$ obtained from the heat capacity calculations (Fig. 6.7) against $L^{-1/\nu}$. The y-intercept gives a reasonable estimate of the bulk critical temperature $T_c^{(\infty)}$. From Fig. 6.6 we can extrapolate the value

$T_c^{(\infty)} = 4.5095 \pm 0.0021$ for the grand-canonical ensemble and the value $T_c^{(\infty)} = 4.4982 \pm 0.0068$ for the canonical ensemble. The two ensemble estimates are in agreement with each other and both values are close to the literature value $T_c^{(\infty)} = 4.5114 \pm 0.0001$ [109, 121].

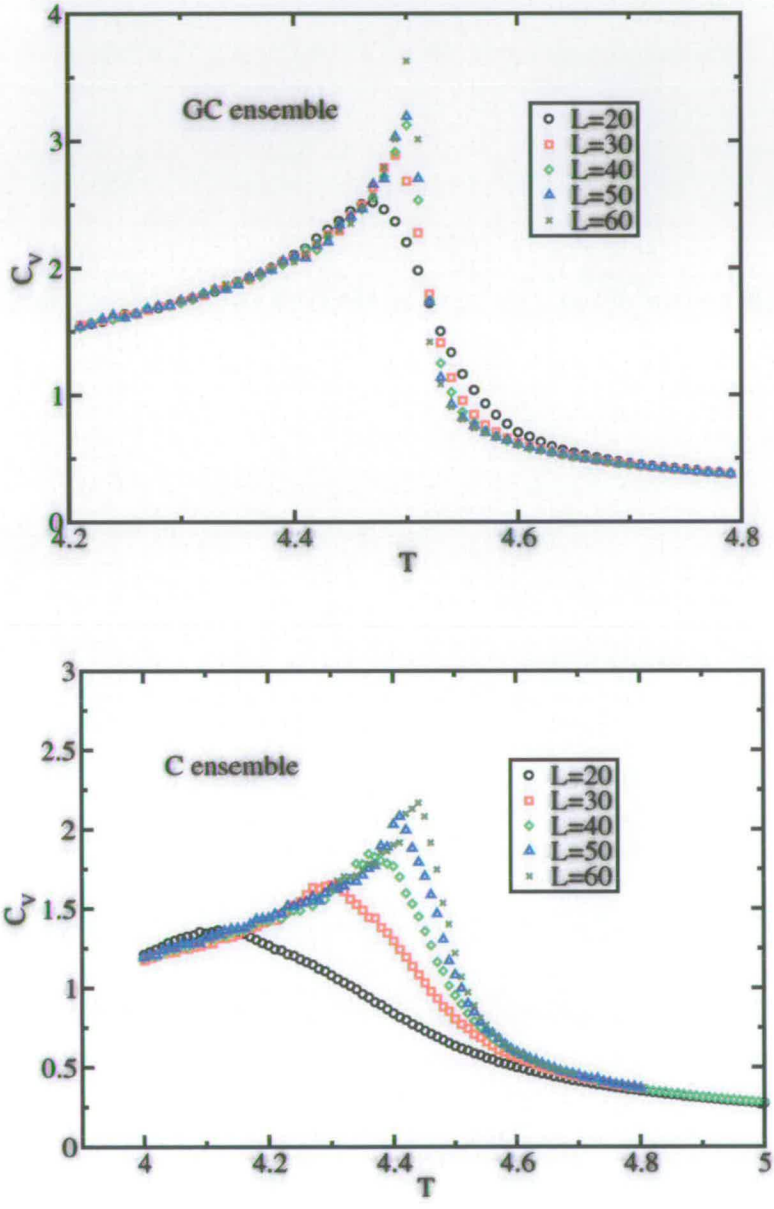

Figure 6.7: The heat capacities C_V calculated in the grand-canonical ensemble (top) and in the canonical ensemble (bottom). The curves present a peak at the apparent critical temperature $T_c^{(L)}$.

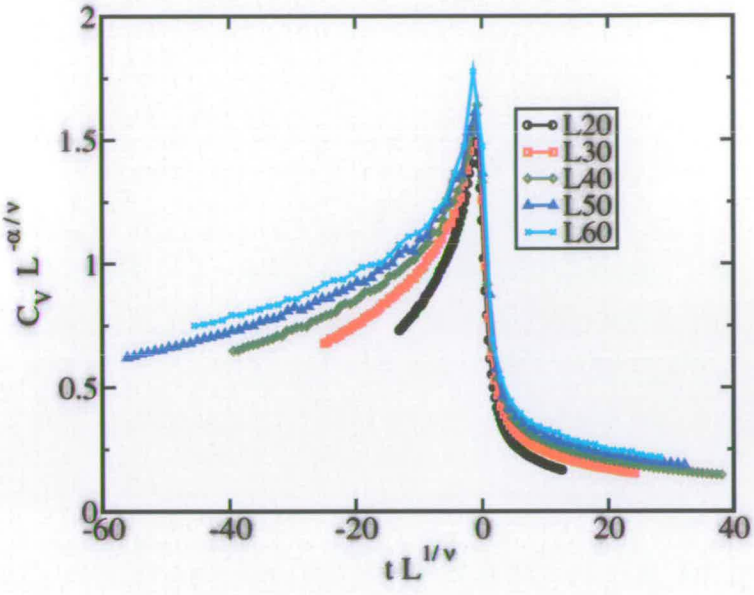

Figure 6.8: Test of the universal scaling law for the constant-volume heat capacity in the grand-canonical ensemble. At the critical point, the curves relative to different sizes L collapse on a single universal curve.

To further test our simulation results, we verify the scaling relation (6.3) as shown in Fig. 6.8 for the grand-canonical ensemble. With the right choice of coordinates, the heat-capacities calculated in different sized systems should collapse to the same universal curve in the vicinity of the critical point. In the next section, we will test a similar scaling behaviour for the ensemble difference ΔC_V of the heat-capacities.

6.6.2 *Ensemble dependence of the heat capacity*

Fig. 6.9 (top) shows the estimated ensemble difference of the heat-capacities near the critical temperature in the standard coordinates (ΔC_V versus T), whereas the figure at the bottom gives a visual confirmation of the universal scaling law for ΔC_V derived in Section 6.4.2. As anticipated, in the vicinity of the critical point, all of the curves collapse on to a single curve which is a universal

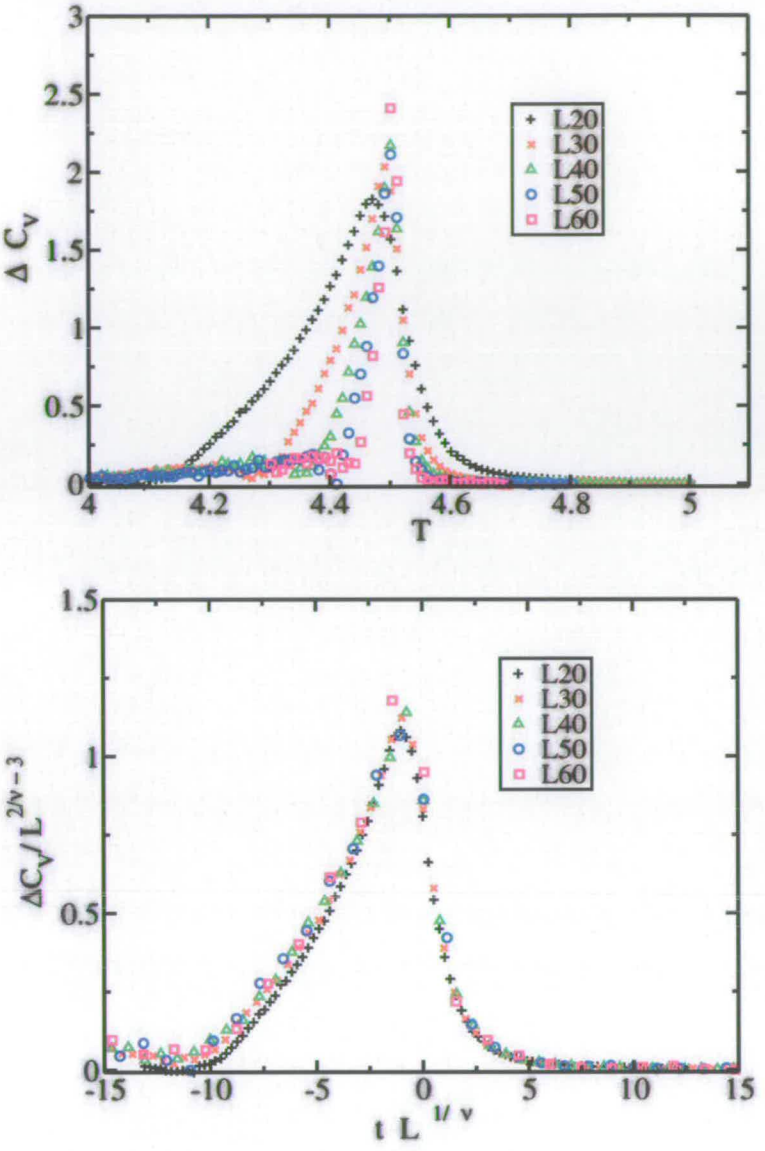

Figure 6.9: Top: constant-volume heat capacity ensemble difference ΔC_V in the standard coordinates. Bottom: universal scaling law for the ensemble difference ΔC_V.

function of $tL^{1/\nu}$. As predicted by Eq. (6.25), the ensemble difference

$$\Delta C_V = \frac{C_V^{\mathcal{NVT}} - C_V^{\mathcal{MVT}}}{k_B L^3} \tag{6.40}$$

grows with L, signalling the inequivalence of the two ensembles at the thermodynamic limit.

6.7 Conclusions

In this chapter we have studied the constant volume heat capacity C_V and its dependence on the simulation ensemble. We used a combination of Wang-Landau simulation techniques and the standard Metropolis algorithm to characterise the ensemble difference ΔC_V and estimate it in a 3D Ising model.

To test the MC scheme proposed in Section 6.5, we have reported FSS analysis of the Ising model in both canonical and grand-canonical ensembles, and derived its critical temperature. The two ensemble estimates were seen to be in agreement with each other and with previous estimates.

In the last part of this chapter, we have derived a universal scaling function for the heat capacity ensemble difference and compared it against our simulation results. These are consistent with each other. Interestingly (and incidentally), the constant-volume heat capacity ensemble difference at the critical temperature follows the same size-dependence as the heat capacity itself. This means that at the critical temperature the difference ΔC_V grows with the system dimension L signalling, as expected, that at the thermodynamic limit C_V diverges. Away from the critical temperature, the difference ΔC_V should instead decrease with increasing the dimension L.

CHAPTER 7

Conclusions

This thesis is divided into two parts. The first part contains three different computer simulation studies on biomineralisation, whereas the second part deals with critical phenomena.

In the first computer simulation study we tried to rationalise the presence of silica nanospheres ($\sim$ 70 nm) which constitute the elementary building blocks of many species of biominerals. Being biomineralisation a broad and complex phenomenon, we focused our study on a specific example. We concentrated on diatom (small marine organisms) silica walls which exhibit the granular nano-structure made of silica spheres typical of many biominerals. Besides of being of inherent interest, the possibility of understanding the molecular-scale processes involved in biomineralisation can help reproduce complex porous architectures useful for a myriad of nanotechnological applications. Diatoms themselves, for instance, are equipped with highly organised mesoporous silica skeletons.

We considered some important experimental results and used them as a starting point for our investigation. The cell walls of the diatom *Cylindrotheca fusiformis*,

for examples, were found to contain a significant amount of organic material. The prevalent organic component has been extracted from the silica and associated to small proteins called *silaffins*. Silaffins consist of a polar (hydrophilic) backbone made of fifteen amino acids and two long polyamine chains whose length is comparable to that of the backbone. In Chapter 3, we speculated on the possibility that silaffins self-assemble due to an effective attraction between the two polyamine chains. The self-assembled structures would then serve as templates for the subsequent deposition of silica. We tested these assumptions with the ultimate goal of explaining the presence of the silica granularity on the nanoscale.

We ran Brownian dynamics computer simulations of model silaffins in which the hydrophilicity of the backbone and the inherent attraction between the tails was explicitly considered. The simulation results show that the dimensions of the structural features that characterise the fluid correlate really well with the experimental results. We measured structure factors, cavity-distribution functions, and main separation between clusters and saw as these quantities, although calculated independently, lead to similar results which are consistent with the experimental observations.

The templating mechanism of biomineralisation proposed in Chapter 3 has been further tested in Chapter 4 in which we adopted a similar computer model to study simple diamines (*putrescine*) and their role in silica deposition and, hence, in biomineralisation. Brownian dynamics simulations of the model putrescine show a series of results in agreement with the experimental results.

The first part of this thesis is concluded with the study of pattern formation in diatoms. The symmetrical siliceous structures that often characterise diatom skeletons are still a puzzling product of biomineralisation. These structures

span over the whole surface of the skeletons which are typically tens of micrometres in diameter. The complexity of these structures, and their dimensions, makes the problem unapproachable by molecular computer simulation techniques. In this chapter, we use a continuum simulation method based on a Ginzburg-Landau description of the free energy. We hypothesise that at the characteristic lengthscales of diatoms (tens of μm) pattern formation can be explained as a consequence of a phase-separation mechanisms occurring at the early stages of diatom morphogenesis. We therefore study a phase-separation model of a binary mixture of an organic component (which could be the silaffins studied in Chapter 3) and an aqueous component (containing a silica precursor), and observe the structures forming as a result of phase separation. In particular we speculate on the possibility that these structures can act as templates for the deposition of silica. The model proposed is able to reproduce the siliceous patterns of many diatom species.

In the last part of the thesis we focus on critical phenomena which regard physical systems near the critical point. We study the ensemble dependence of the constant-volume heat capacity in a finite three-dimensional Ising model via Monte Carlo computer simulations. We employ a computer algorithm based on modern flat-histogram MC techniques (such as the Wang-Landau method) and the standard Metropolis algorithm. We perform a systematic finite-size scaling analysis of our results (to test the algorithm adopted), and estimate the heat-capacity difference ΔC_V in the vicinity of the critical point for the canonical and the grand-canonical ensemble.

APPENDIX A

Interfacial tension γ

Consider the simple case of a planar interface in the $y-z$ plane centered at $x=0$, separating the two phases in a cubic box of side L. According to the now classic work by Cahn and Hilliard [34], the Helmholtz free-energy is

$$\mathcal{H} = \frac{L^2}{v_0}\int_{-L/2}^{L/2}\left[\epsilon\left(-\frac{1}{2}\phi^2+\frac{1}{4}\phi^4\right)+\kappa_1\left(\frac{d\phi}{dx}\right)^2\right]dx. \tag{A.1}$$

The order parameter that minimise this equation is found using the calculus of variations [122]. The resulting Euler-Lagrange equation can be written as

$$-\epsilon\phi+\epsilon\phi^3-\frac{\partial}{\partial x}\left(2\kappa_1\frac{\partial\phi}{\partial x}\right)=0 \tag{A.2}$$

or equivalently

$$\frac{\partial^2\phi}{\partial x^2}=\frac{\epsilon}{2\kappa_1}(\phi^3-\phi) \tag{A.3}$$

and yields the result

$$\phi(x)=\tanh\left(\frac{x}{2\xi}\right)=\frac{\exp(x/2\xi)-\exp(-x/2\xi)}{\exp(x/2\xi)+\exp(-x/2\xi)} \tag{A.4}$$

where $\xi=\sqrt{\kappa_1/\epsilon}$ is the interfacial width.

The difference in free-energy, $\Delta\mathcal{H}$, between the case of two isolated pure phases ($\phi = \pm 1$ and $d\phi/dx = 0$) and the case of the same two phases with a shared interface, is related to the interfacial tension γ, namely

$$\gamma = \frac{\mathcal{H}_{inter.}}{L^2} - \frac{\mathcal{H}_{no\ inter.}}{L^2} \tag{A.5}$$

or equivalently

$$\gamma = \frac{1}{v_0}\int_{-L/2}^{L/2}\left[\epsilon\left(-\frac{1}{2}\phi^2 + \frac{1}{4}\phi^4\right) + \kappa_1\left(\frac{d\phi}{dx}\right)^2 - \left(-\frac{1}{4}\epsilon\right)\right]dx \tag{A.6}$$

The solution of this integral with the prescribed form of $\phi(x)$ (Eq. A.4), is

$$\gamma = \frac{4\sqrt{\kappa_1}\epsilon}{3v_0}. \tag{A.7}$$

Finally, the relations between the energy parameter κ_1 and the interfacial tension γ either in real or in reduced units are

$$\kappa_1 = \frac{9\gamma^2 v_0^2}{16\epsilon} \tag{A.8}$$

$$\kappa_1^* = \left(\frac{3\gamma v_0}{4\epsilon\Delta}\right)^2 \tag{A.9}$$

The parameters κ_1^* used in the simulations are tabulated in Tab. 5.1.

APPENDIX B

Papers published

- L. Lenoci and P. J. Camp, "Self-assembly of peptide scaffolds in biosilica formation: Computer simulations of a coarse-grained model", J. Am. Chem. Soc. **128**, 10111-10117 (2006)
- L. Lenoci and P. J. Camp, "Diatom structures templated by phase-separated fluids", Langmuir **24**, 217-223 (2007)

These are bound at the end of the thesis.

References

[1] H. A. Lowenstam and S. Weiner. *On Biomineralization*. Oxford University Press, Oxford, 1989.

[2] M. Sumper and N. Kröger. Silica formation in diatoms: the function of long-chain polyamines and silaffins. *J. Mat. Chem.*, 14:2059–2065, 2004.

[3] F. E. Round, R. Crawford, and D. G. Mann. *The Diatoms: Biology and Morphology of the Genera*. Cambridge University Press, Cambridge, 1990.

[4] Diatoms from South China Sea. http://life.xmu.edu.cn.

[5] S. Albeck, J. Aizenberg, L. Addadi, and S. Weiner. Interactions of various skeletal intracrystalline components with calcite crystals. *J. Am. Chem. Soc.*, 115:11691–11697, 1993.

[6] B. Devouard, M. Posfai, X. Hua, D. A. Bazylinski, R. B. Frankel, and P. R. Buseck. Magnetite from magnetotactic bacteria; size distributions and twinning. *American Mineralogist*, 83:1387–1398, 1998.

[7] A. Berman, L. Addadi, and S. Weiner. Interactions of sea-urchin skeleton macromolecules with growing calcite crystals - A study of intracrystalline proteins. *Nature*, 331:546–548, 1988.

[8] L. Lenoci and P. J. Camp. Self-assembly of peptide scaffolds in biosilica formation: Computer simulations of a coarse-grained model. *J. Am. Chem. Soc.*, 128:10111–10117, 2006.

[9] Sea urchins: A chemical perspective. http://reefkeeping.com/issues/2004-08/rhf/index.php.

[10] R. J. P. Williams. An introduction to biominerals and the role of organic molecules in their formation. *Philosophical Transactions of the Royal Society of London*, 304:411–424, 1984.

[11] D. M. Dabbs and I. A. Aksay. Self-assembled ceramics produced by complex-fluid templation. *Annu. Rev. Phys. Chem.*, 51:601–622, 2000.

[12] J. S. Beck, J. C. Vartuli, W. J. Roth, M. E. Leonowicz, C. T. Kresge, K. D. Schmitt, C. T.-W. Chu, D. H. Olson, E. W. Sheppard, S. B. McCullen, J. B. Higgins, and J. L. Schlenker. A new family of mesoporous molecular-sieves prepared with liquid-crystal templates. *J. Am. Chem. Soc.*, 114:10834–10843, 1992.

[13] C. T. Kresge, M. E. Leonowicz, W. J. Roth, J. C. Vartuli, and J. S. Beck. Ordered mesoporous molecular-sieves synthesized by a liquid-crystal template mechanism. *Nature*, 359:710–712, 1992.

[14] F. Noll, M. Sumper, and N. Hampp. Nanostructure of diatom silica surfaces and of biomimetic analogues. *Nano. Letters*, 2:91–95, 2002.

[15] N. Kröger, S. Lorenz, E. Brunner, and M. Sumper. Self-assembly of highly phosphorylated silaffins and their function in biosilica morphogenesis. *Science*, 298:584–586, 2002.

[16] M. Sumper. A phase separation model for the nanopatterning of diatom biosilica. *Science*, 295:2430–2433, 2002.

[17] T. A. Witten and P. A. Pincus. *Structured fluids*. Oxford University Press Inc., Oxford, 2004.

[18] David P. Landau and K. Binder. *Monte Carlo simulations in statistical physics*. Cambridege University Press, Cambridge, 2nd edition, 2005.

[19] S. C. Glotzer. Computer simulations of spinodal decomposition in polymer blends. *Annual Review of Computational Physics*, 2:1–47, 1995.

[20] Phase transition. http://en.wikipedia.org/wiki/Phase_change.

[21] J-P. Hansen and I. R. McDonald. *Theory of simple liquids*. Academic Press, London, 1986.

[22] I. Herbut. *A modern approach to critical phenomena*. Cambridge University Press, Cambridge, 2007.

[23] P. M. Chaikin and T. C. Lubensky. *Principles of condensed matter physics*. Cambridge University Press, Cambridge, 1995.

[24] M. P. Allen and D. J. Tildesley. *Computer simulation of liquids*. Clarendon Press, Oxford, 1987.

[25] Wang F and D. P. Landau. Efficient, multiple-range random walk algorithm to calculate the density of states. *Phys. Rev. Lett.*, 86:2050–2054, 2001.

[26] L. Onsager. *Physical Review*, 65:117, 1944.

[27] D. Frenkel and B. Smit. *Understanding Molecular Simulations*. Academic Press, London, 2002.

[28] K. Binder and G. Ciccotti, editors. *Theory of phase transitions beyond mean field theory*, Bologna, 1996. Italian Physical Society.

[29] L. M. Ghiringhelli, C. Valeriani, E. J. Meijer, and D. Frenkel. Local structure of liquid carbon controls diamond nucleation. *Phys. Rev. Lett.*, 99:055702, 2007.

[30] Steve O. Nielsen, Carlos F. Lopez, Goundla Srinivas, and Michael L. Klein. Coarse grain models and the computer simulation of soft materials. *J. Phys.: Condens. Matter*, 16:R481–R512, 2004.

[31] P. D. Duncan. *Computer simulation of two-dimensional condensed matter systems*. PhD thesis, School of Chemistry, University of Edinburgh, 2006.

[32] D. Chandler. *Introduction to modern statistical mechanics*. Oxford University Press, Oxford, 1987.

[33] L. D. Landau. Clarendon Press, Oxford, 1938.

[34] J. W. Cahn and J. E. Hilliard. Free energy of a nonuniform system. i. interfacial free energy. *J. Chem. Phys.*, 28:258–267, 1958.

[35] M. L. Chiappino and B. E. Volcani. Studies on biochemistry and fine-structure of silicia shell formation in diatoms .7. Sequential cell-wall development in pennate navicula-pelliculosa. *Protoplasma*, 93:205–221, 1977.

[36] E. J. Cox. Variation in patterns of valve morphogenesis between representatives of six biraphid diatom genera (bacillariophyceae). *J. Phycol.*, 35:1297–1312, 1999.

[37] S. A. Crawford, M. J. Higgins, P. Mulvaney, and R. Wetherbee. Nanostructure of the diatom frustule as revealed by atomic force and scanning electron microscopy. *J. Phycol.*, 37:543–554, 2001.

[38] A. M. M. Schmid and D. Schulz. Wall morphogenesis in diatoms - Deposition of silica by cytoplasmic vesicles. *Protoplasma*, 100:267–288, 1979.

[39] N. Kröger, R. Deutzmann, C. Bergsdorf, and M. Sumper. Species-specific polyamines from diatoms control silica morphology. *Proc. Natl. Acad. Sci. (USA)*, 97:14133–14138, 2000.

[40] N. Kröger, R. Deutzmann, and M. Sumper. Polycationic peptides from diatom biosilica that direct silica nanosphere formation. *Science*, 286:1129–1132, 1999.

[41] N. Kröger and R. Wetherbee. Pleuralins are involved in theca differentiation in the diatom cylindrotheca fusiformis. *Protist*, 151:263–273, 2000.

[42] W. H. van de Poll, E. G. Vrieling, and W. W. C. Gieskes. Location and expression of frustulins in the pennate diatoms cylindrotheca fusiformis, navicula pelliculosa, and navicula salinarum (bacillariophyceae). *J. Phycol.*, 35:1044–1053, 1999.

[43] N. Poulsen, M. Sumper, and N. Kröger. Biosilica formation in diatoms: Characterization of native silaffin-2 and its role in silica morphogenesis. *Proc. Natl. Acad. Sci. (USA)*, 100:12075–12080, 2003.

[44] E. Brunner, K. Lutz, and M. Sumper. Biomimetic synthesis of silica nanospheres depends on the aggregation and phase separation of polyamines in aqueous solution. *Phys. Chem. Chem. Phys.*, 6:854–857, 2004.

[45] S. Mann. Biomineralization: the form(id)able part of bioinorganic chemistry! *J. Chem. Soc. Dalton Trans.*, pages 3953–3961, 1997.

[46] S. Mann, S. A. Davis, S. R. Hall, M. Li, K. H. Rhodes, W. Shenton, S. Vaucher, and B. Zhang. Crystal tectonics: Chemical construction and self-organization beyond the unit cell. *J. Chem. Soc. Dalton Trans.*, pages 3753–3763, 2000.

[47] A. De Robertis, C. Foti, O. Giuffrè, and S. Sammartano. Dependence on ionic strength of polyamine protonation in NaCl aqueous solution. *J. Chem. Eng. Data*, 46:1425–1435, 2001.

[48] S. Dixit, J. Crain, W. C. K. Poon, J. L. Finney, and A. K. Soper. Molecular segregation observed in a concentrated alcohol-water solution. *Nature*, 416:829–832, 2002.

[49] K. Lutz, C. Gröger, M. Sumper, and E. Brunner. Biomimetic silica formation: Analysis of the phosphate-induced self-assembly of polyamines. *Phys. Chem. Chem. Phys.*, 7:2812–2815, 2005.

[50] R. A. Rana, V. S. Murthy, J. Yu, and M. S. Wong. Nanoparticle self-assembly of hierarchically order microcapsule structures. *Adv. Mater.*, 17:1145–1150, 2005.

[51] G. S. Grest, M.-D. Lacasse, K. Kremer, and A. M. Gupta. Efficient continuum model for simulating polymer blends and copolymers. *J. Chem. Phys.*, 105:10583–10594, 1996.

[52] K. H. Kim, S. H. Kim, J. Huh, and W. H. Jo. Micellization behavior of pi-shaped copolymers in a selective solvent: A Brownian dynamics simulation approach. *J. Chem. Phys.*, 119:5705–5710, 2003.

[53] L. Guo and E. Luijten. Reversible gel formation of triblock copolymers studied by molecular dynamics simulation. *J. Polym. Sci. B*, 43:959–969, 2005.

[54] P. K. Maiti, Y. Lansac, M. A. Glaser, and N. A. Clark. Self-assembly in surfactant oligomers: A coarse-grained description through molecular dynamics simulations. *Langmuir*, 18:1908–1918, 2002.

[55] P. J. Camp and P. E. Barran. Studying self-assembly and nanopatterning in biological materials by computer simulation. Personal communication, 2004.

[56] J. D. Weeks, D. Chandler, and H. C. Andersen. Role of repulsive forces in determining the equilibrium structure fo simple liquids. *J. Chem. Phys.*, 54:5237–5247, 1971.

[57] G. S. Grest and K. Kremer. Molecular dynamics simulation for polymers in the presence of a heat bath. *Phys. Rev. A*, 33:3628–3631, 1986.

[58] K. Lum, D. Chandler, and J. D. Weeks. Hydrophobicity at small and large length scales. *J. Phys. Chem. B*, 103:4570–4577, 1999.

[59] S. Bhattacharya and K. E. Gubbins. Modeling triblock surfactant-templated mesostructured cellular foams. *J. Chem. Phys.*, 123:134907, 2005.

[60] B. Smit, P. A. J. Hilbers, L. A. M. Rupert, and N. M. van Os. Structure of a water/oil interface in the presence of micelles: A computer simulation study. *J. Phys. Chem.*, 95:6361–6368, 1991.

[61] F. K. von Gottberg, K. A. Smith, and T. A. Hatton. Stochastic dynamics simulation of surfactant self-assembly. *J. Chem. Phys.*, 106:9850–9857, 1997.

[62] J. Israelachvili. Self-assembly in two dimensions: Surface micelles and domain formation in monolayers. *Langmuir*, 10:3774–3781, 1994.

[63] D. Belton, S. V. Patwardhan, and C. C. Perry. Putrescine homologues control silica morphogenesis by electrostatic interactions and the hydrophobic effect. *Chem. Comm.*, pages 3475–3477, 2005.

[64] S. V. Patwardhan, S. J. Clarson, and C. C. Perry. On the role(s) of additives in bioinspired silicification. *Chem. Comm.*, pages 1113–1121, 2005.

[65] D. Belton, S. V. Patwardhan, and C. C. Perry. Spermine, spermidine and their analogues generate tailored silica. *J. Mater. Chem.*, pages 4629–4638, 2005.

[66] D. S. Goodsell. Inside a living cell. *Trends in Biological Sciences*, 16:203–206, 1991.

[67] S. Salaniwal, S. K. Kumar, and A. Z. Panagiotopoulos. Competing ranges of attractive and repulsive interactions in the micellization of model surfactants. *Langmuir*, 19:5164–5168, 2003.

[68] Spicule. http://en.wikipedia.org/wiki/Spicule.

[69] S. Mann and G. A. Ozin. Synthesis of inorganic materials with complex form. *Nature*, 382:313–318, 1996.

[70] Christian Gröger, Katharina Lutz, and Eike Brunner. Biomolecular self-assembly and its relevance in silica biomineralization. *Cell Biochemistry and Biophysics*, 2007.

[71] Putrescine homologues and silica formation. Unpublished results.

[72] P. Ungerer, C. Beauvais, J. Delhommelle, A. Boutin, B. Rousseau, and A. H. Fuchs. Optimization of the anisotropic united atoms intermolecular potential for n-alkanes. *J. Chem. Phys.*, 112:5499–5510, 2000.

[73] Close-packing. http://en.wikipedia.org/wiki/Close-packing.

[74] D. Werner. *Biology of Diatoms*. Blackwell Science Ltd, Oxford, 1977.

[75] Algae world. http://rbg-web2.rbge.org.uk/algae.

[76] A. M. M. Schmid and B. E. Volcani. Wall morphogenesis in coscinodiscus wailesii gran and angst. i. valve morphology and development of its architecture. *J. Phycol.*, 19:387–402, 1983.

[77] R. Gordon and R. W. Drum. The chemical basis of diatom morphogenesis. *Int. Rev. Cytol.*, 150:243–372, 1994.

[78] J. Parkinson, Y. Brechet, and R. Gordon. Centric diatom morphogenesis: a model based on a dla algorithm investigating the potential role of microtubules. *Biochimica et Biophysica Acta*, 1452:89–102(14), 13 October 1999.

[79] R. W. Eppley, R. W. Holmes, and E. Paasche. Periodicity in cell division and physiological behavior of ditylum brightwellii, a marine planktonic diatom during growth in light-dark cycles. *Arch. Mikrobiol.*, 56:305–323, 1967.

[80] W. M. Darley, C. W. Sullivan, and B. E. Volcani. Studies on the biochemistry and fine structure of silica shell formation in diatoms: division cycle and chemical composition of navicula pelliculosa during light-dark synchronized growth. *Planta*, 130:159–167, 1976.

[81] C. W. Sullivan and B. E. Volcani. *Silicon and Siliceous Structures in Biological Systems*. Springer-Verlag, New York, 1981.

[82] R.E. Hecky, K. Mopper, P. Kilham, and E. T. Degens. The amino acid and sugar composition of diatom cell-walls. *Marine Biology*, 19:323–331, 1973.

[83] A.J. Bray. Theory of phase ordering kinetics. *Adv. Phys.*, 43:357–459, 1994.

[84] M. Teubner and R. Stray. Origin of the scattering peak in microemulsions. *J. Chem. Phys.*, 87:3195–3200, 1987.

[85] G. Gompper and M. Schick. *Self-assembling amphiphilic systems*, volume 16. Academic Press, London, 1994.

[86] T. Pang. *An Introduction to Computational Physics*. Cambridge University Press, Cambridge, 1st edition, 1997.

[87] Bgsu center for algae microscopy and image digitization. http://www.bgsu.edu/departments/biology/facilities/algae/index.html.

[88] Eureka: Diatoms - nature's gems. http://hjs.geol.uib.no/diatoms.

[89] S. Komura and H. Kodama. Two-order-parameter model for an oil-water-surfactant system. *Phys. Rev. E*, 55:1722–1727, 1997.

[90] M. Ruggeri and G. Gonnella. Rheological behavior of microemulsions. *Phys. Rev. E*, 66:031506, 2002.

[91] D. A. Huse. Corrections to late-stage behavior in spinodal decomposition: Lifshitz-Slyozov scaling and Monte Carlo simulations. *Phys. Rev. B*, 34:7845–7850, 1986.

[92] D. J. Donahue and F. E. Bartell. The boundary tension at water-organic liquid interfaces. *J. Phys. Chem.*, 56:480–484, 1952.

[93] D. W. Thompson. *On Growth and Form*. Cambridge University Press, Cambridge, 1917.

[94] T. Okuzono and T. Ohta. Self-propulsion of cellular structures in chemically reacting mixtures. *Phys. Rev. E*, 64:045201(R), 2001.

[95] S. Sugiura, T. Okuzono, and T. Ohta. Time-modulated oscillatory structures in phase-separating reactive mixtures. *Phys. Rev. E*, 66:066216, 2002.

[96] J. Verdasca, P. Borckmans, and G. Dewel. Chemically frozen phase separation in an adsorbed layer. *Phys. Rev. E*, 52:R4616–R4619, 1995.

[97] J. D. Murray. *Mathematical biology*. Springer-Verlag, Berlin, 1989.

[98] C. D. Daub, P. J. Camp, and G. N. Patey. The constant-volume heat capacity of near-critical fluids with long-range interactions: A discussion of different Monte Carlo estimates. *J. Chem. Phys.*, 118:4164–4168, 2003.

[99] C. D. Daub, P. J. Camp, and G. N. Patey. Constant-volume heat capacity in a near-critical fluid from Monte Carlo simulations. *J. Chem. Phys.*, 121, 2004. 8956-8959.

[100] P. J. Camp, C. D. Daub, and G. N. Patey. Liquid-vapor criticality in coulombic and related fluids: What can be learned from computer simulations? In D. Henderson, M. Holovko, and A. Trokhymchuk, editors, *Ionic Soft Matter: Modern trends in theory and applications*, volume NATO Science Series II: Mathematics, Physics and Chemistry Vol. 206, pages 181–197, Dordrecht, 2005. Springer.

[101] T. L. Hill. *Statistical mechanics: Principles and selected applications*. Dover Publications, Inc., New York, 1987.

[102] J. Valleau and G. Torrie. Heat capacity of the restricted primitive model near criticality. *J. Chem. Phys.*, 108:5169–5172, 1998.

[103] J. Valleau and G. Torrie. Further remarks on the heat capacity of the restricted primitive model. *J. Chem. Phys.*, 117:3305–3309, 2002.

[104] E. Luijten, M. E. Fisher, and A. Z. Panagiotopoulos. Universality class of criticality in the restricted primitive model electrolyte. *Phys. Rev. Lett.*, 88:185701, 2002.

[105] M. E. Fisher. The renormalization group in the theory of critical behavior. *Rev. Mod. Phys.*, 46:597, 1974.

[106] K. Binder and G. Ciccotti, editors. *Monte Carlo and Molecular Dynamics of Condensed Matter Systems*, Bologna, 1996. Italian Physical Society.

[107] V. V. Privman. *Finite size scaling and numerical simulation of statistical systems*. World Scientific, London, 1990.

[108] M. N. Barber. Finite-size scaling. In C. Domb and J. L. Lebowitz, editors, *Phase Transitions and Critical Phenomena*, volume 8, pages 146–268, London, 1983. Academic Press.

[109] A. M. Ferrenberg and D. P. Landau. Critical behavior of the three-dimensional Ising model: A high-resolution Monte Carlo study. *Phys. Rev. B*, 44:5081–5091, 1991.

[110] Xising. http://seehuhn.de/pages/xising.

[111] R. Hilfer and N. B. Wilding. Are critical finite-size scaling functions calculable from knowledge of an appropriate critical exponent? *J. Phys. A: Math. Gen.*, 28:L281–L286, 1995.

[112] R. Hilfer. Absence of hyperscaling violations for phase transitions with positive specific heat exponent. *Z. Phys. B.*, 96:63–77, 1994.

[113] C. Zhang and J. Ma. Simulation via direct computation of partition functions. *Phys. Rev. E*, 76:036708, 2007.

[114] David. J. Earl and Michael W. Deem. Parallel tempering: Theory, applications, and new perspectives. *Phys. Chem. Chem. Phys.*, 7:3910–3916, 2005.

[115] M. S. Shell, P. G. Debenedetti, and A. Z. Panagiotopoulos. *J. Chem. Phys.*, 119:9406, 2003.

[116] Georg Ganzenmüller and Philip. J. Camp. Applications of Wang-Landau sampling to determine phase equilibria in complex fluids. *J. Chem. Phys.*, 127:154504, 2007.

[117] K. Binder. Finite size scaling analysis of Ising model block distribution functions. *Z. Phys. B*, 43:119–140, 1981.

[118] G.-M. Zhang and C.-Z. Yang. Numerical determination of the order of phase transition of the two-dimensional Potts model with multispin interactions. *J. Phys. A: Math. Gen.*, 26:4907–4910, 1993.

[119] Murty S. S. Challa, D. P. Landau, and K. Binder. Finite-size effects at temperature-driven first-order transitions. *Phys. Rev. B*, 34:1841–1852, 1986.

[120] Jooyoung Lee and J. M. Kosterlitz. Finite-size scaling and Monte Carlo simulations of first-order phase transitions. *Phys. Rev. B*, 43:3265, 1991.

[121] K. Binder and E. Luijten. Monte Carlo tests of renormalization-group predictions for critical phenomena in Ising models. *Phys. Rep.*, 344:179–253, 2001.

[122] H. Goldstein. *Classical mechanics*. Addison-Wesley, London, 2nd edition, 1980.

J|A|C|S
ARTICLES
Published on Web 07/13/2006

Self-Assembly of Peptide Scaffolds in Biosilica Formation: Computer Simulations of a Coarse-Grained Model

Leonardo Lenoci and Philip J. Camp*

Contribution from the School of Chemistry, University of Edinburgh, West Mains Road, Edinburgh EH9 3JJ, United Kingdom

Received February 20, 2006; E-mail: philip.camp@ed.ac.uk

Abstract: The self-assembly of model peptides is studied using Brownian dynamics computer simulations. A coarse-grained, bead−spring model is designed to mimic silaffins, small peptides implicated in the biomineralization of certain silica diatom skeletons and observed to promote the formation of amorphous silica nanospheres in vitro. The primary characteristics of the silaffin are a 15 amino acid hydrophilic backbone and two modified lysine residues near the ends of the backbone carrying long polyamine chains. In the simulations, the model peptides self-assemble to form spherical clusters, networks of strands, or bicontinuous structures, depending on the peptide concentration and effective temperature. The results indicate that over a broad range of volume fractions (0.05−25%) the characteristic structural lengthscales fall in the range 12−45 nm. On this basis, we suggest that self-assembled structures act as either nucleation points or scaffolds for the deposition of 10−100 nm silica−peptide building blocks from which diatom skeletons and synthetic nanospheres are constructed.

1. Introduction

One of the major goals in materials chemistry is to devise methods for the controlled fabrication of complex structures from simple inorganic materials. Aside from being of considerable inherent interest, the ability to construct architectures on the nanoscale would provide a means of producing devices for technological applications. In developing appropriate synthetic strategies, it is becoming commonplace to look for inspiration from Nature and how she controls biomineralization.[1] The most abundant biominerals are calcium carbonate and silica, with most siliceous materials being found in marine single-cell organisms such as diatoms and radiolaria.[2,3] Diatom cell walls (frustules) exhibit a variety of complex porous architectures on the 10 nm to 10 μm lengthscale, made from composites of hydrated SiO_2 and biopolymers. Atomic force and scanning electron microscope images of diatom frustules indicate that the fundamental building blocks are tightly packed spheres, with diameters in the region of 10−100 nm.[4−8]

At this early stage in the study of biomineralization at the molecular scale, it is necessary to focus on some specific examples before attempting to identify connections between seemingly disparate systems. There is a vast number of diatom species to survey, but the past decade has seen some significant advances. Therefore, for the purpose of this article, we can give only a brief summary of a particular set of experiments. In a series of exciting papers, Sumper and co-workers have explored the detailed structure and properties of biosilica extracted from a range of diatom species. For example, the frustule of the diatom *Cylindrotheca fusiformis* was found to contain significant amounts of organic material which includes characteristic proteins called "silaffins",[9] and long-chain polyamines (LCPAs).[10] There are other components present, but these are known to associate with biosilica only after deposition is complete.[11,12] Three main silaffin fractions were identified with molecular weights of 4 kDa (silaffin 1A), 8 kDa (silaffin 1B), and 17 kDa (silaffin 2). Silaffin 1A itself was found to consist of a mixture of two peptides—designated $1A_1$ and $1A_2$—with very similar primary structures. The primary structure of silaffin $1A_1$ contains serine (S), lysine (K), glycine (G), and tyrosine (Y) residues: SSKKSGSYSGSKGSK. The serines are phosphorylated, whereas the lysines at positions 3 and 15 are each posttranslationally modified with a polyamine tail containing 5−10 *N*-methylpropylamine [$-(CH_2)_3 - N(CH_3)-$] units connected to the backbone by a link of propylamine [$-(CH_2)_3 - NH-$] units; see Figure 1c of ref 13.

Silaffins are implicated in the formation of the complex porous structures in diatom frustules, and so it was of interest to find out whether silaffins can promote silica formation in vitro from a suitable precursor. The addition of silaffin 1A (0.1−

(1) Mann, S.; Ozin, G. A. *Nature* **1996**, *382*, 313−318.
(2) Volcani, B. E.; Simpson, T. L. *Silicon and siliceous structures in biological systems*; Springer: Berlin, 1981.
(3) Lowenstam, H. A.; Weiner, S. *On Biomineralization*; Oxford University Press: Oxford, 1989.
(4) Chiappino, M. L.; Volcani, B. E. *Protoplasma* **1977**, *93*, 205−221.
(5) Schmid, A. M. M.; Schulz, D. *Protoplasma* **1979**, *100*, 267−288.
(6) Cox, E. J. *J. Phycol.* **1999**, *35*, 1297−1312.
(7) Crawford, S. A.; Higgins, M. J.; Mulvaney, P.; Wetherbee, R. *J. Phycol.* **2001**, *37*, 543−554.
(8) Noll, F.; Sumper, M.; Hampp, N. *Nano Lett.* **2002**, *2*, 91−95.
(9) Kröger, N.; Deutzmann, R.; Sumper, M. *Science* **1999**, *286*, 1129−1132.
(10) Kröger, N.; Deutzmann, R.; Bergsdorf, C.; Sumper, M. *Proc. Natl. Acad. Sci. U.S.A.* **2000**, *97*, 14133−14138.
(11) van de Poll, W. H.; Vrieling, E. G.; Gieskes, W. W. C. *J. Phycol.* **1999**, *35*, 1044−1053.
(12) Kröger, N.; Wetherbee, R. *Protist* **2000**, *151*, 263−273.
(13) Kröger, N.; Lorenz, S.; Brunner, E.; Sumper, M. *Science* **2002**, *298*, 584−586.

10.1021/ja061211s CCC: $33.50

0.5 mM) to ~1 M silicilic acid at pH > 3 yields a precipitate of silica spheres with diameters in the range 400−700 nm.[9,13] These dimensions are not biologically relevant, but time-resolved studies suggest that the early stages of biosilica formation lead to a moldable silica−silaffin composite from which large spheres emerge as a result of subsequent artificial processes.[13] Silaffin 2 appears to play a regulatory role,[14] whereas LCPAs from a range of biological species are known to promote nanopatterned silica formation.[10,15] In the case of the genus *Coscinodiscus*, the formation of a hierarchical hexagonal silica frustule is thought to be driven by the phase separation and droplet formation of LCPAs in water, which would suggest that the LCPAs are somewhat hydrophobic.[16] (A separate computational test of this "phase-separation" model is currently in progress.) Recent work indicates that the self-assembly of LCPAs might be promoted by specific anionic additives—such as phosphates—providing bridges between (protonated) nitrogen centers.[17,18] The roles of amine groups in the acid−base chemistry of silica condensation have also been noted.[19] A review of experiments on silaffins and LCPAs in the context of silica formation can be found in ref 20.

At this point we briefly mention that silica deposition can also be effected by a silaffin-type peptide without the post-translational, polyamine tail modification.[9,21−23] Nonmodified peptide R5 is made up of 19 amino acids, forming the silaffin $1A_1$ backbone plus two arginines (R), an isoleucine (I), and a leucine (L) appended to the C-terminus. The RRIL motif has been shown to be crucial for silica deposition and to the formation of aggregates.[23] It has been suggested that the close proximity of the charged arginine residues to the hydrophobic isoleucine and leucine residues leads to the self-assembly of micelle-like structures; the R5 backbone without the RRIL motif shows almost no silica deposition and no aggregate formation.[23] This indicates that the polyamine tails on silaffins are crucial for aggregate formation.

In this article, we make the first simulation-led attack on the problem of how silaffins alone might promote the formation of 10−100 nm silica−peptide composites. As with all such phenomena, it is tempting to speculate that the peptides self-assemble to form some sort of scaffold around which an (as yet unknown) precursor can deposit silica.[24−27] Indeed, the analogies between the formation of porous biominerals, and the synthetic templating of microporous and mesoporous solids,[28,29] appear all too obvious. The fact that silaffin 1A alone can precipitate silica suggests that it possess an inherent ability to self-assemble.[13] The silaffin peptide backbone comprises polar amino acids, and the serines are phosphorylated; hence, this will be a strongly hydrophilic unit due to the opportunity for electrostatic and hydrogen-bonding interactions with water. We propose that self-assembly is driven by an effective attraction between the polyamine tails, arising either from a solubility mismatch between the tails and the backbone or from a phosphate-bridging mechanism, as explained below.

The tertiary amine groups—once protonated—represent the only hydrophilic components of the polyamine tails. The pK_a for the conjugate acid of an isolated tertiary amine group is usually around 9,[30] but the close proximity of other protonation sites within the polyamine tails will significantly reduce the probability of many sites on the same tail being protonated under near-neutral conditions. To get an idea of the magnitude of this effect, consider *N*,*N*,*N*′,*N*′-tetramethyl-1,3-propanediamine, $(CH_3)_2N(CH_2)_3N(CH_3)_2$, for which the pK_a of the singly protonated molecule is 9.76 and that of the doubly protonated molecule is 7.53.[31] Assessing the degree of protonation at anything but infinite dilution is not straightforward due to the role of activity coefficients, but this effect combined with the presence of the absolutely hydrophobic propyl and methyl units may limit the extent to which the polyamine tails can compete with the peptide backbone for contact with the solvent. (Indeed, a protonated propylamine unit by itself may possess amphiphilic characteristics; even small polar molecules, such as methanol and ethanol, do not fully mix with water on the molecular scale.[32]).

Phosphate-bridging mechanisms have also been proposed to explain the apparent tendency for polyamine chains to aggregate.[15,17,18] Experiments on polyallylamines with molecular weights in the region of 15 kDa show that the formation of aggregates is strongly dependent on the concentration of phosphate anions[15] and on the pH.[18] Different anions do not facilitate aggregation, and so it is likely that there is a specific hydrogen-bonding mechanism for the cross-linking of the polyamine tails. Similar observations have been made with dephosphorylated silaffins[13] and poly(L-lysine).[17] Returning to silaffins, it is therefore possible that the phosphorylated backbone provides the necessary bridging phosphate groups to mediate an effective attraction between the polyamine tails. In ref 13, Kröger et al. "conclude that the numerous phosphate groups in [natural silaffin 1A] serve as an intrinsic source of anions required for silica formation by diatoms".

In summary, experiments on silaffins, and on pure polyamines, suggest that there is an effective attraction between the polyamine units, driving self-assembly and hence scaffold formation. To explore the implications of these effects, it would be preferable to obtain simulation results for an atomistically detailed representation of silaffins in solution. For the sizes of molecules under consideration here, and the lengthscales (up

(14) Poulsen, N.; Sumper, M.; Kröger, N. *Proc. Natl. Acad. Sci. U.S.A.* **2003**, *100*, 12075−12080.
(15) Brunner, E.; Lutz, K.; Sumper, M. *Phys. Chem. Chem. Phys.* **2004**, *6*, 854−857.
(16) Sumper, M. *Science* **2002**, *295*, 2430−2433.
(17) Rana, R. K.; Murthy, V. S.; Yu, J.; Wong, M. S. *Adv. Mater.* **2005**, *17*, 1145−1150.
(18) Lutz, K.; Gröger, C.; Sumper, M.; Brunner, E. *Phys. Chem. Chem. Phys.* **2005**, *7*, 2812−2815.
(19) Patwardhan, S. V.; Clarson, S. J.; Perry, C. C. *Chem. Commun.* **2005**, 1113−1121.
(20) Sumper, M.; Kröger, N. *J. Mater. Chem.* **2004**, *14*, 2059−2065.
(21) Brott, L. L.; Naik, R. R.; Pikas, D. J.; Kirkpatrick, S. M.; Tomlin, D. W.; Whitlock, P. W.; Clarson, S. J.; Stone, M. O. *Nature* **2001**, *413*, 291−293.
(22) Naik, R. R.; Whitlock, P. W.; Rodriguez, F.; Brott, L. L.; Glawe, D. D.; Clarson, S. J.; Stone, M. O. *Chem. Commun.* **2003**, 238−239.
(23) Knecht, M. R.; Wright, D. W. *Chem. Commun.* **2003**, 3038−3039.
(24) Mann, S. *J. Chem. Soc., Dalton Trans.* **1997**, 3953−3961.
(25) Mann, S.; Davis, S. A.; Hall, S. R.; Li, M.; Rhodes, K. H.; Shenton, W.; Vaucher, S.; Zhang, B. *J. Chem. Soc., Dalton Trans.* **2000**, 3753−3763.
(26) Dabbs, D. M.; Aksay, I. A. *Annu. Rev. Phys. Chem.* **2000**, *51*, 601−622.
(27) Patwardhan, S. V.; Mukherjee, N.; Steinitz-Kannan, M.; Clarson, S. J. *Chem. Commun.* **2003**, 1122−1123.
(28) Kresge, C. T.; Leonowicz, M. E.; Roth, W. J.; Vartuli, J. C.; Beck, J. S. *Nature* **1992**, *359*, 710−712.
(29) Beck, J. S.; Vartuli, J. C.; Roth, W. J.; Leonowicz, M. E.; Kresge, C. T.; Schmitt, K. D.; Chu, C. T.-W.; Olson, D. H.; Sheppard, E. W.; McCullen, S. B.; Higgins, J. B.; Schlenker, J. L. *J. Am. Chem. Soc.* **1992**, *114*, 10834−10843.
(30) De Robertis, A.; Foti, C.; Giuffrè, O.; Sammartano, S. *J. Chem. Eng. Data* **2001**, *46*, 1425−1435.
(31) Näsänen, R.; Tilus, P.; Teikari, T. *Finn. Chem. Lett.* **1974**, 263−265.
(32) Dixit, S.; Crain, J.; Poon, W. C. K.; Finney, J. L.; Soper, A. K. *Nature* **2002**, *416*, 829−832.

to hundreds of nanometers) being probed in experiments, this is not a realistic proposition. We therefore seek a coarse-grained model that includes the essential characteristics of real molecules and ignores any irrelevant molecular detail. We might model the silaffins as polyelectrolytes, but in the absence of concrete evidence about the degree and pattern of protonation on the polyamine tails, not to mention the possibility that "covalent" bonding may be important, it would seem premature to follow this path. On the basis of the physical arguments offered above, we have constructed model silaffins consisting of strongly hydrophilic peptide backbones, decorated with mutually attractive flexible tails. The coarse-grained model is obtained from a "bead−spring" approach, which originated in simulations of polymer blends and block copolymers.[33] Each "bead" represents the average shape of a group of atoms, and the beads are connected with "springs" in such a way as to mimic the essential structural characteristics of the molecule. Bead−spring models continue to find application in a vast range of complex-fluid problems, including block copolymers, surfactants, polypeptides, and polyelectrolytes. The model we describe in section 2 resembles those of certain gemini amphiphiles and (bio)-polymers[34−36] which have been studied with coarse-graining approaches.

Given the coarse-grained bead−spring model, we use Brownian dynamics (BD) simulations to assemble and characterize molecular aggregates that might be formed and therefore identify putative structural templates for biosilica spheres. In what follows, we will show that the characteristic lengthscales of the self-assembled structures are in the range 12−45 nm, i.e., comparable to the sizes of natural biosilica building blocks.[4−8] Encouraged by the accord of our simulation results with experimental observations, we then go on to speculate as to the role of structure-directing peptides, such as silaffins, in the formation of biosilica.

This article is organized as follows. Details of the model and the simulation methodology will be presented in section 2. Results are presented and discussed in section 3, and section 4 concludes the paper.

2. Model and Simulation Methods

The silaffin backbone consists of 15 amino acids. In *crystals*, the average spacing between amino acids in an elongated β-strand is ~0.35 nm. Due to the high concentration of phosphorylated serine residues, it is unlikely that the backbone will form a more compact α-helix in solution; thus, for the order-of-magnitude calculations presented below, we estimate that the length of the backbone is ~6 nm. We represent the backbone with three hydrophilic "head" (H) beads, linked by finitely extensible nonlinear elastic (FENE) springs[37] to be defined below. The silaffin tails typically consist of ~10 propylamine units. Assuming C−C and C−N bond lengths of ~0.15 nm, the length of a tail will be roughly comparable with the length of the backbone. Hence, we represent each chain by three tail (T) beads, again linked by FENE springs. The resulting molecular structure is illustrated in Figure 1. For purposes of comparison with experimental parameters below, the bead diameter is roughly equal to 2 nm.

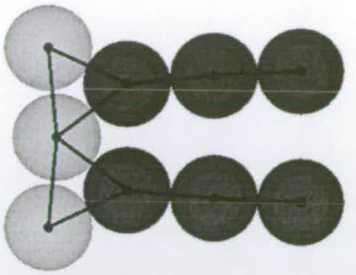

Figure 1. Molecular model considered in this work. The yellow beads represent the peptide backbone, and the blue beads represent the polyamine tails. The FENE springs are shown as black lines connecting the beads.

The bead−bead interactions are defined in terms of the Lennard-Jones (LJ) potential

$$u_{\mathrm{LJ}}(r) = 4\epsilon\left[\left(\frac{\sigma}{r}\right)^{12} - \left(\frac{\sigma}{r}\right)^{6}\right] \tag{1}$$

where ϵ is the well depth, and σ is the bead diameter. The head−head (HH) interaction potential is taken to be

$$u_{\mathrm{HH}}(r) = \begin{cases} u_{\mathrm{LJ}}(r) - u_{\mathrm{LJ}}(r_0) & r \le r_0 \\ 0 & r > r_0 \end{cases} \tag{2}$$

where $r_0 = 2^{1/6}\sigma$ is the position of the minimum in the LJ potential. The potential coincides with the Weeks−Chandler−Andersen potential.[38] It is purely repulsive, and in this case reflects the assumption that the components of the hydrophilic backbone are ambivalent toward solvation and mutual interaction. The tail−tail (TT) interaction potential must include an attractive portion, to promote aggregation:

$$u_{\mathrm{TT}}(r) = \begin{cases} u_{\mathrm{LJ}}(r) - u_{\mathrm{LJ}}(r_c) & r \le r_c \\ 0 & r > r_c \end{cases} \tag{3}$$

The cutoff distance is taken to be $r_c = 2.5\sigma$; the resulting cut-and-shifted potential is almost identical with the full LJ potential, and is continuous at $r = r_c$. The head−tail (HT) interaction potential is taken to be the same as that for the HH interaction, i.e., $u_{\mathrm{HT}}(r) = u_{\mathrm{HH}}(r)$ (2). The FENE spring potential linking each bead to its neighbor(s) is

$$u_{\mathrm{FENE}}(r) = -\frac{1}{2}kR_0^2 \ln\left[1 - \left(\frac{r}{R_0}\right)^2\right] \tag{4}$$

where $k = 30\epsilon\sigma^{-2}$ is the spring constant and $R_0 = 1.5\sigma$ is the maximum allowable separation between bonded beads.[37]

With a cutoff distance of $r_c = 2.5\sigma$, the range of $u_{\mathrm{TT}}(r)$ is comparable with the bead diameter. At first glance, this situation appears somewhat unrealistic because each bead (representing several functional groups) has dimension ~2 nm, while direct interatomic forces are limited to the subnanometer range. It must be remembered, however, that coarse-grained "potentials" are really free energies, resulting from an integration over the solvent degrees of freedom, with the beads held fixed. Therefore, the interaction range is not restricted to those of interatomic forces; it should be extended to accommodate longer-range, solvent-mediated effects such as hydrophobic attraction.[39]

BD simulations[40] of $N_m = 300$ or $N_m = 600$ molecules (corresponding to $N_b = 2700$ and $N_b = 5400$ beads, respectively) were carried out in a cubic simulation cell of volume $V = L^3$ with periodic boundary conditions applied. The masses of all beads were set equal to m.

(33) Grest, G. S.; Lacasse, M.-D.; Kremer, K.; Gupta, A. M. *J. Chem. Phys.* **1996**, *105*, 10583−10594.
(34) Maiti, P. K.; Lansac, Y.; Glaser, M. A.; Clark, N. A. *Langmuir* **2002**, *18*, 1908−1918.
(35) Kim, K. H.; Kim, S. H.; Huh, J.; Jo, W. H. *J. Chem. Phys.* **2003**, *119*, 5705−5710.
(36) Guo, L.; Luijten, E. *J. Polym. Sci. B* **2005**, *43*, 959−969.
(37) Grest, G. S.; Kremer, K. *Phys. Rev. A* **1986**, *33*, 3628−3631.
(38) Weeks, J. D.; Chandler, D.; Andersen, H. C. *J. Chem. Phys.* **1971**, *54*, 5237−5247.
(39) Lum, K.; Chandler, D.; Weeks, J. D. *J. Phys. Chem. B* **1999**, *103*, 4570−4577.
(40) Allen, M. P.; Tildesley, D. J. *Computer simulation of liquids*; Clarendon Press: Oxford, 1987.

The equation of motion of bead i is

$$m\ddot{\mathbf{r}}_i = -\nabla_i U - m\xi\,\dot{\mathbf{r}}_i + \mathbf{R}_i \qquad (5)$$

where $\mathbf{r}_i$ is the position vector of bead i, U is the potential energy (given by an appropriate sum over pairs of beads and bonds), ξ is the friction coefficient, and $\mathbf{R}_i$ is a stochastic force, representing the influence of the solvent. The latter term is represented by Gaussian white noise, subject to the fluctuation–dissipation relation $\langle \mathbf{R}_i(t)\cdot\mathbf{R}_j(t')\rangle = 6mk_BT\xi\delta_{ij}\delta(t - t')$. The equations of motion were integrated using a velocity-Verlet-like algorithm.[40] The reduced time step was set equal to $\delta t = 0.01\tau$, where $\tau = \sqrt{m\sigma^2/\epsilon}$ is the basic unit of time. The reduced friction coefficient was $\xi = 5\tau^{-1}$, which represents damped dynamics appropriate to the large chemical units being represented by each bead. The reduced bead density is $\rho^* = N_b\sigma^3/V$, and the volume fraction is $\phi = \pi\rho^*/6$. The strength of the bead–bead interaction is measured by the reduced temperature $T^* = k_BT/\epsilon$, where k_B is Boltzmann's constant. On thermodynamic grounds, T^* must be at most on the order of 1 for self-assembly to occur so that the effective attraction may overcome the entropy penalty associated with clustering.

For each state point considered, we carried out equilibration and production runs consisting of $\sim 10^5$ time steps. Equilibration was assessed by comparing energies and cluster distribution functions (section 3.2) from four independent runs with different initial configurations and random-number generator seeds (for the stochastic force part). For low densities $\rho^* \leq 0.1$, systems of $N_m = 300$ molecules were sufficiently large to accommodate the self-assembled structures that emerged. At higher densities ($\rho^* = 0.3$, 0.5) systems of $N_m = 600$ molecules were studied in addition to check for finite-size effects (which were found to be insignificant). In each case, initial configurations were well equilibrated at high temperature ($T^* \sim 5$).

3. Results and Discussion

Test runs at high temperatures $T^* > 1$ showed no significant signs of self-assembly. Runs at low temperatures $T^* < 0.5$ exhibited self-assembled structures, but the equilibration and relaxation were extremely sluggish, and required prohibitively long simulations. We therefore concentrated on two temperatures between these extremes, $T^* = 0.5$ and $T^* = 0.8$. We first describe the qualitative aspects of self-assembly in the model system (section 3.1). We then characterize cluster formation at low densities (section 3.2), and other structural aspects at higher densities as evidenced by the static structure factor and transient (silaffin-free) cavities in the model fluid (section 3.3).

3.1. Self-Assembly. In Figure 2 we show final configurations at a representative selection of densities, and at temperatures of $T^* = 0.5$ and $T^* = 0.8$. At low densities ($\rho^* \leq 0.1$) distinct aggregates resembling micelles are in evidence. An analysis of the cluster distribution is presented in section 3.2. At higher densities ($\rho^* = 0.3$, 0.5) the fluid is characterized by extended networks of elongated structures that locally resemble bilayers or wormlike micelles, with the polyamine tails interdigitated. The overall gel-like structure possesses numerous cavities, which of course would be occupied by solvent and silica precursor in the real system. These structures are vaguely reminiscent of those observed in simulations of gemini surfactants,[34] and the extended networks of triblock-surfactant templates.[41] The characteristic structural lengthscale, and the distribution of cavity sizes, will be considered in section 3.3. Self-assembled structures are essentially absent at temperatures above $T^* = 1$, and at densities above $\rho^* = 0.5$.

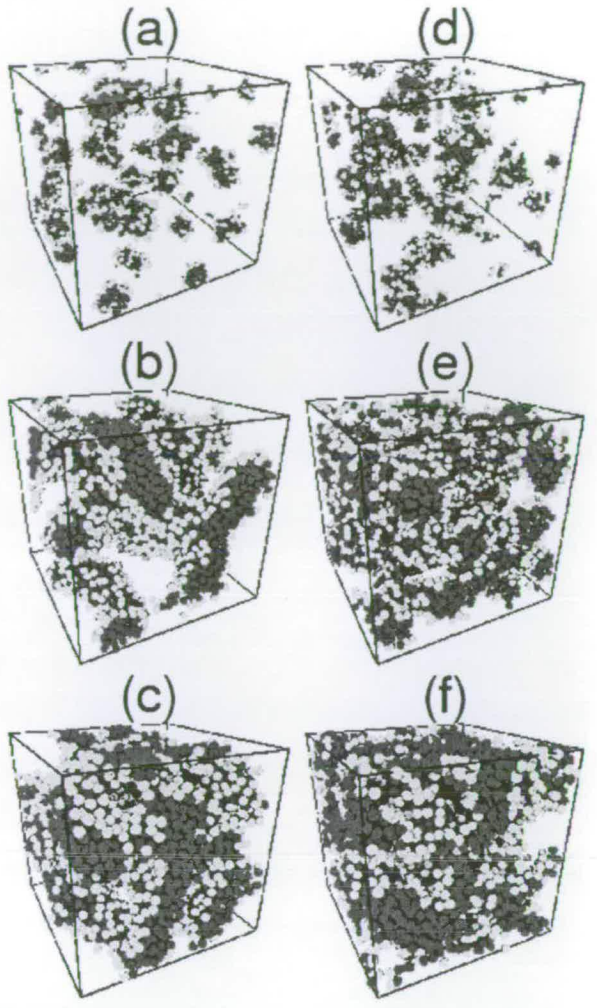

Figure 2. Simulation configurations after equilibration: (a) $T^* = 0.5$, $\rho^* = 0.06$; (b) $T^* = 0.5$, $\rho^* = 0.3$; (c) $T^* = 0.5$, $\rho^* = 0.5$; (d) $T^* = 0.8$, $\rho^* = 0.06$; (e) $T^* = 0.8$, $\rho^* = 0.3$; (f) $T^* = 0.8$, $\rho^* = 0.5$. System sizes at $\rho^* = 0.06$ are $N_m = 300$ molecules, while those at $\rho^* = 0.3$ and $\rho^* = 0.5$ are $N_m = 600$ molecules.

3.2. Structure at Low Density ($\rho^* \leq 0.1$). Cluster formation at low densities ($\rho^* \leq 0.1$) was explored by computing the volume fraction of clusters containing n molecules, ϕ_n. If any two mutually attracting tail beads on two different molecules were within a cutoff distance $r_{tail} = 1.5\sigma$, then those two molecules were deemed to belong to the same cluster.[42,43] (An alternative cluster criterion will be discussed below.) The overall degree of aggregation at a given temperature was monitored by plotting the volume fraction of free molecules (ϕ_1) against the total volume fraction (ϕ), as shown in Figure 3. At very low concentrations, we see that $\phi_1 \approx \phi$, as should be expected when there is little or no aggregation. At $T^* = 0.5$ the free-molecule concentration reaches a peak at a total volume fraction $\phi \simeq 0.008$, while at $T^* = 0.8$ the peak occurs at $\phi \simeq 0.01$; we loosely identify the positions of these peaks as the critical 'micelle' concentrations.[44] At higher concentrations, the clusters

(41) Bhattacharya, S.; Gubbins, K. E. *J. Chem. Phys.* **2005**, *123*, 134907.

(42) Smit, B.; Hilbers, P. A. J.; Esselink, K.; Rupert, L. A. M.; van Os, N. M.; Schlijper, A. G. *J. Phys. Chem.* **1991**, *95*, 6361–6368.

(43) von Gottberg, F. K.; Smith, K. A.; Hatton, T. A. *J. Chem. Phys.* **1997**, *106*, 9850–9857.

(44) Israelachvili, J. *Langmuir* **1994**, *10*, 3774–3781.

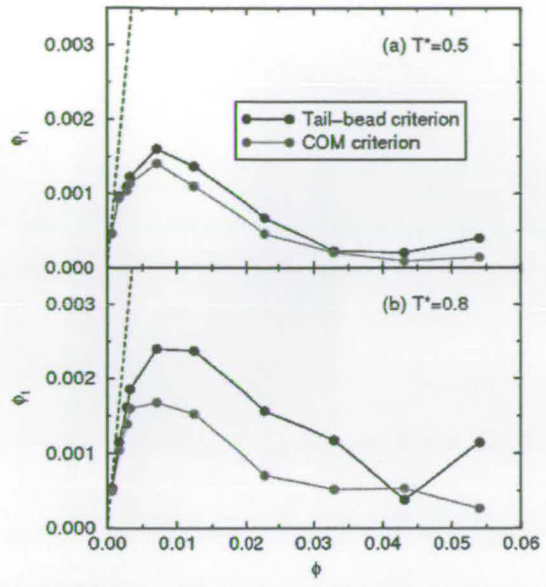

Figure 3. Volume fraction of free monomers (ϕ_1) against total volume fraction (ϕ) at temperatures (a) $T^* = 0.5$ and (b) $T^* = 0.8$. The black points represent the tail-bead distance criterion, and the red points represent the molecular center-of-mass distance criterion (see text). The dashed lines represent the asymptotic, low-density dependence $\phi_1 = \phi$.

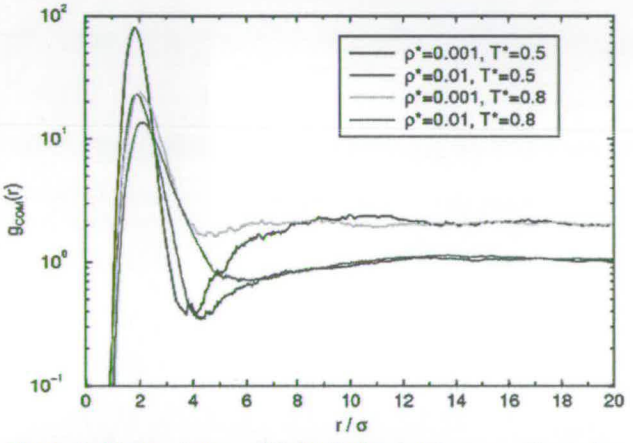

Figure 4. Center-of-mass radial distribution functions, $g_{COM}(r)$ at $\rho^* = 0.001$, $T^* = 0.5$ (black); $\rho^* = 0.01$, $T^* = 0.5$ (red); $\rho^* = 0.001$, $T^* = 0.8$ (green); and $\rho^* = 0.01$, $T^* = 0.8$ (blue). The curves for $\rho^* = 0.001$ (green and black) approach $g_{COM}(r) = 1$ at $r >> 20\sigma$ (not shown).

coalesce to form larger aggregates, and ultimately structures that span the simulation cell.

An important technical question is how to identify clusters unambiguously, and in a physical meaningful way. Thus far, our definition has been based on a tail-bead distance criterion, in line with earlier work.[42,43] In the case of molecules with very long tails, however, this criterion becomes necessary but not sufficient to identify two monomers belonging to the same aggregate; just two beads in close proximity may not be sufficient to bind the molecules together. We therefore tested an alternative criterion based on the separation of the molecular centers-of-mass (COMs). To establish a suitable cutoff distance, we first computed the center-of-mass radial distribution function, $g_{COM}(r)$.[40] In Figure 4 we plot $g_{COM}(r)$ for systems at various densities and temperatures. The peaks centered at $r \simeq 2\sigma$ signal aggregated pairs of molecules. Minima occur in the range $r = 4-6\sigma$ and provide natural criteria for discriminating between aggregated and free pairs of molecules. We implemented the COM cluster criterion with a cutoff of $r_{COM} = 5\sigma$; the results for ϕ_1 versus ϕ are compared with those using the conventional tail-bead criterion in Figure 3. The two criteria yield very similar results at low concentrations, which is comforting because there the clusters are quite distinct (see Figure 2). At higher concentrations, the COM criterion yields a smaller number of free monomers, particularly so at the higher temperature ($T^* = 0.8$). One explanation is that at high concentrations and high temperatures, the centers-of-mass of two molecules can be in close proximity simply due to confinement, and without the tail-beads being within interaction range. Despite this minor discrepancy, the general trends in Figure 3 are insensitive to the cluster criterion, and hence our estimates of the critical micelle concentrations are unaltered.

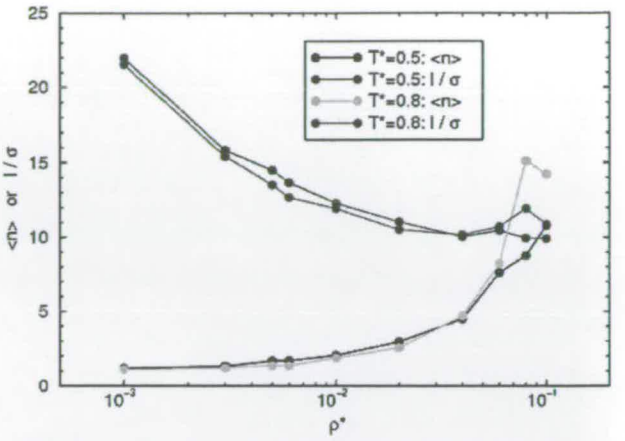

Figure 5. Average number of molecules per cluster ($\langle n \rangle$) and average cluster separation (l/σ) at $T^* = 0.5$ (black and red, respectively) and $T^* = 0.8$ (green and blue, respectively).

One of the objectives of this study is to identify characteristic structural lengthscales that might correlate with the sizes of the silica building blocks found in diatom skeletons. In the low-density regime currently under consideration, one key dimension is the average separation between neighboring clusters, which we denote by l. We first need to calculate the average cluster density: since there are 9 beads per molecule, this quantity is equal to $\rho^*/9\langle n \rangle$, where $\langle n \rangle$ is the average number of molecules per cluster. In reduced units, l is then given by

$$\frac{l}{\sigma} = \left(\frac{9\langle n \rangle}{\rho^*}\right)^{1/3} \tag{6}$$

In Figure 5 we show $\langle n \rangle$ (from the tail-bead criterion) and l/σ as functions of density along the isotherms $T^* = 0.5$ and $T^* = 0.8$. The average cluster size $\langle n \rangle$ grows with increasing concentration, and above $\rho^* = 0.1$ all molecules in the system belong to the same aggregate. The mean separation between clusters decreases monotonically with increasing density and then appears to level off at around 10σ. In this density regime, it is tempting to ask whether the formation of silica spheres is initiated on the surfaces of clusters or even, at very low densities, from a single peptide. In this scenario, the silica spheres might grow out radially from spherical nuclei until they come in contact, and so the sphere size would be dictated by the mean separation between neighboring clusters. From Figure 5 we see

that over a wide range of volume fraction ($0.05\% \leq \phi \leq 5\%$), the mean separation varies relatively little; with $\sigma \simeq 2$ nm, the silica-sphere diameter would be between 20 and 45 nm. This is in excellent agreement with the dimensions of the silica building blocks seen in experiments;[4-8] however, without knowing the real volume fraction of peptide in diatom cells, it is impossible to tell whether this nucleation mechanism is reasonable. It would be very useful to know how the organic components are distributed within the silica building blocks found in diatom skeletons; this might provide valuable clues about the mechanism.

3.3. Structure at High Density ($\rho^* > 0.1$). We now consider the characteristic structural lengthscales that develop in the model systems at moderate densities, $\rho^* > 0.1$. Of primary interest is the characteristic dimension of the cavities, that is to say, the spaces between the molecules, because this is where silica condensation would be most likely to occur. To gauge the dimensions of the cavities, we computed the static structure factor, which is sensitive to variations in density, and is accessible in scattering experiments.[45] The low-wavevector behavior of $S(q)$ was monitored by a direct calculation using the relation

$$S(\mathbf{q}) = \frac{1}{N_b}\langle \rho_{\mathbf{q}}\rho_{-\mathbf{q}}\rangle \tag{7}$$

where

$$\rho_{\mathbf{q}} = \sum_{j=1}^{N_b} \exp(-i\mathbf{q}\cdot\mathbf{r}_j) \tag{8}$$

is a Fourier component of the bead density, and $\mathbf{q}$ is a wavevector commensurate with the cubic periodic boundary conditions. Contributions with equal $q = |\mathbf{q}|$ were averaged.

In Figure 6 we show $S(q)$ at two densities ($\rho^* = 0.3$ and $\rho^* = 0.5$) and two temperatures ($T^* = 0.5$ and $T^* = 0.8$). At $\rho^* = 0.3$ and at both temperatures, peaks in $S(q)$ are visible in the region of $q \simeq 0.5\sigma^{-1}$. At $\rho^* = 0.5$ and $T^* = 0.5$, $S(q)$ continues to rise down to the lowest accessible wavevector ($q = 2\pi/L$) signaling that there is structure which spans the simulation cell. At $\rho^* = 0.5$ and $T^* = 0.8$, a peak is apparent at $q \simeq 1\sigma^{-1}$. $S(q)$ is a measure of inhomogeneity in the bead density on the lengthscale $2\pi/q$, and so the peaks in $S(q)$ signal the presence of structural features with that characteristic dimension. As we will confirm below, these structural features are the *voids*. With $\sigma \simeq 2$ nm, peaks in $S(q)$ at $q = 0.5-1\sigma^{-1}$ correspond to real-space dimensions in the range 13−25 nm. These dimensions are the same order of magnitude as those of the silica building blocks found in diatom skeletons.[4-8]

We now characterize the structure further by measuring a probability density of cavity sizes, $Q(r)$: the probability that the nearest bead to a randomly chosen point is at a distance between r and $r + dr$ is $Q(r)dr$. (We note that $Q(r)$ is related to the excess chemical potential of a hard sphere immersed in the fluid.[46,47]) Every 20 time steps in the BD simulations, N randomly selected points within the simulation cell were chosen, and a histogram of $Q(r)$ was accumulated.

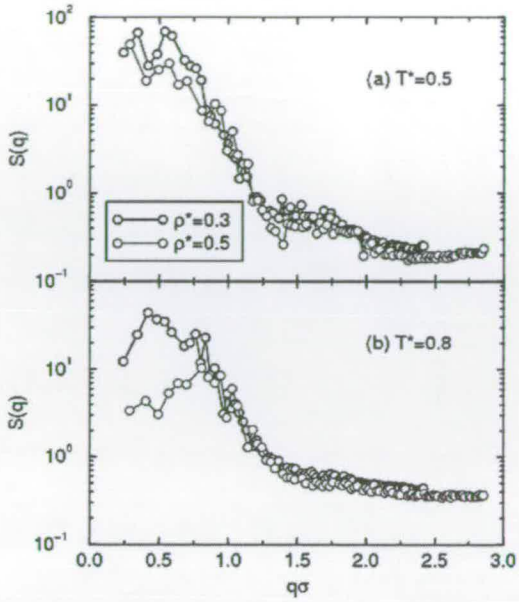

Figure 6. Bead static structure factor, $S(q)$, at temperatures (a) $T^* = 0.5$ and (b) $T^* = 0.8$. The black points are at density $\rho^* = 0.3$, and the red points are at $\rho^* = 0.5$.

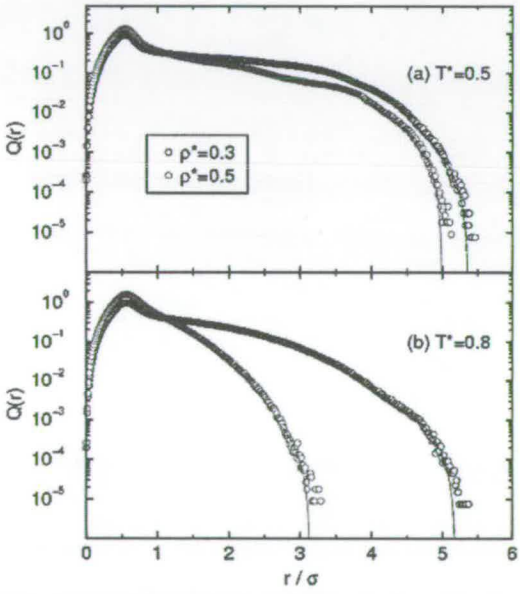

Figure 7. Cavity-radius probability distribution function, $Q(r)$, at temperatures (a) $T^* = 0.5$ and (b) $T^* = 0.8$. The black points are at density $\rho^* = 0.3$, and the red points are at $\rho^* = 0.5$. The solid lines are fits to the assumed asymptotic form at large r, $Q(r) \propto (r_{max} - r)^2$, where r_{max} is the maximum cavity radius.

A selection of results at densities $\rho^* > 0.1$, and temperatures $T^* = 0.5$ and $T^* = 0.8$, are shown in Figure 7. At all densities and temperatures, there are peaks in $Q(r)$ at $r \simeq 0.5\sigma$, which correspond to small cavities within regions of closely associated molecules. More significantly, peaks and shoulders at larger values of r reflect the dimensions of the voids apparent in the simulation snapshots (Figure 2). We suggest that the most relevant lengthscale for biomineralization is the value of r above which $Q(r)$ is essentially zero, since this should reflect the

(45) Chaikin, P. M.; Lubensky, T. C. *Principles of condensed matter physics;* Cambridge University Press: Cambridge, 1995.
(46) Pohorille, A.; Pratt, L. R. *J. Am. Chem. Soc.* **1990**, *112*, 5066−5074.
(47) Pratt, L. R.; Pohorille, A. *Proc. Natl. Acad. Sci. U.S.A.* **1992**, *89*, 2995−2999.

maximum dimensions of the cavities; to highlight the decay of $Q(r)$ at large r, the plots in Figure 7 are on linear−log scales. If the cavities are roughly spherical, then the probability of picking a point such that the distance from the inner surface of the cavity is between r and $r + dr$ should scale like $4\pi(r_{max} - r)^2 dr$, i.e., $Q(r) \propto (r_{max} - r)^2$ as $r \rightarrow r_{max}$. This function was fitted to the data near r_{max}; the fits are included in Figure 7. As is clear from the figure, the values of r_{max} lie in the range $3-6\sigma$, which corresponds to cavity diameters in the range 12−24 nm. These values match up very closely with those determined from $S(q)$ above, which shows that $S(q)$ and $Q(r)$ provide consistent measures of the cavity dimensions.

At these relatively high volume fractions (15−25%) silica growth would be controlled by the available space between the organic molecules. Hence, the cavities represent a kind of template. The resulting composite of silica and peptide might be the "moldable biosilica" from which certain (nonporous) structural elements of diatom skeletons are made.[20]

4. Conclusions

In this article, we have studied the structure of model peptides in aqueous solution using coarse-grained, Brownian dynamics computer simulations. The model peptides were constructed to mimic silaffins comprising 15 hydrophilic amino acids and two pendant long-chain polyamine tails. Effective attractive forces operated between the tails to represent either hydrophobic interactions (possibly more relevant to high-pH conditions) or phosphate-bridging between protonated nitrogen centers.

At low volume fractions (≤5%) distinct clusters are in evidence, with the mean separation between clusters being in the range 20−45 nm, depending on concentration. A gel-like structure emerges at a volume fraction of 15% in which a network of self-assembled strands spans the simulation cell, whereas at a volume fraction of 25%, the strands merge to form a more concentrated bicontinuous structure. The characteristic feature of these denser phases is the presence of cavities, with dimensions in the range 12−25 nm. The simulations are performed using reduced units, so there are uncertainties in our estimates of real dimensions. Nonetheless, despite the primitive nature of the peptide model, the characteristic structural length-scales are directly comparable with the dimensions of the moldable silica building blocks that fuse together to form diatom skeletons.

We suggest two different scenarios for the production of the moldable silica−peptide composite, each relevant to a different range of peptide concentration. At low peptide volume fractions (<5%) distinct aggregates could provide nucleation surfaces from which amorphous silica spheres might expand radially. A similar scenario has been put forward already by Patwardhan et al.[27] Roughly speaking, the apparent silica-sphere diameter would be delimited by the mean cluster separation. At higher volume fractions (>5%) growing amorphous silica blocks would be confined by the surrounding peptide network. To discriminate between the two scenarios, it is crucial to know how peptides are distributed within biosilica, and at what concentrations; this might be achieved using high-resolution microscopies (AFM, SEM, TEM). In the low-density nucleation scenario, the peptide would be concentrated in the cores of the silica blocks. In the high-density confinement picture, the peptide would be distributed more evenly, like a scaffold. We note here that, as a general rule, the volume fraction of macromolecules in a typical biological cell is of the order of 10%.[48] Alternatively, a volume fraction of ∼10% might be representative of the *local* peptide concentration in the interior of large aggregates, or indeed a compartment of the cell. During the growth process, the silica would eventually envelope the underlying peptide matrix, possibly resulting in a moldable composite with superior mechanical properties; knock-on effects of the growing silica on the templating peptide have not been examined here, but this may be examined in future work. The general principles suggested in this work may also apply to other systems, such as peptide R5[9,21−23] and poly(L-lysine).[27,17] Simulations might also be directed toward the effects of peptide conformation on the deposition of silica. Recent experiments show that poly(L-lysine) assembled into α-helices can pack into hexagonal sheets and hence template the formation of hexagonal silica platelets.[49] If converted to a β-sheet conformation, however, poly(L-lysine) deposits networks of silica spheres. To tackle these types of problems, a less coarse-grained simulation model is required to render variations in hydrophobicity and hydrophilicity within, say, a peptide backbone. We are currently working on calculations along these lines.

Finally, we speculate more generally on the roles of long-chain polyamines and silaffins in biomineralization. Long-chain polyamines in water likely form microemulsions of small droplets; indeed, this is the basis for the "phase separation" model proposed by Sumper.[16] Although this might lead to hierarchical patterning, it does not necessarily explain the fine structure of biosilica on the 10−100 nm scale. It is therefore conceivable that the role of the peptide backbones in silaffins is to frustrate microphase separation of the polyamine tails, and to promote local ordering on the molecular scale. This could be tested by analyzing silica deposition as a function of polyamine chain length and/or backbone hydrophilicity; longer chains and less-repulsive backbone groups should favor phase separation over self-assembly.[50]

This discussion is necessarily speculative. Nonetheless, we have made some concrete predictions which could be tested in a relatively straightforward way. In addition, we hope that our suggestions motivate a rational approach to designing silaffin analogues with useful structure-directing properties.

Acknowledgment. We thank Drs. Perdita Barran and David Dryden for discussions and critical readings of the draft manuscript, and the School of Chemistry at the University of Edinburgh for the provision of a studentship to L.L.

JA061211S

(48) Goodsell, D. S. *Trends Biol. Sci.* **1991**, *16*, 203−206.
(49) Patwardhan, S. V.; Maheshwari, R.; Mukherjee, N.; Kiick, K. L.; Clarson, S. J. *Biomacromolecules* **2006**, *7*, 491−497.
(50) Salaniwal, S.; Kumar, S. K.; Panagiotopoulos, A. Z. *Langmuir* **2003**, *19*, 5164−5168.

Diatom Structures Templated by Phase-Separated Fluids

Leonardo Lenoci and Philip J. Camp*

School of Chemistry, University of Edinburgh, West Mains Road, Edinburgh EH9 3JJ, United Kingdom

Received July 27, 2007. In Final Form: September 28, 2007

An experimentally motivated model is proposed for the formation of fluid-phase templates corresponding to the porous silica skeletons of diatoms, single-cell organisms found in marine and freshwater environments. It is shown that phase-separation processes on a planar surface may give rise to a quasi-static mold that could direct the deposition of condensing silica to form complex arrays of pores. Calculations show that appropriate fluid templates can be generated for a wide variety of diatom species. The results could be of some biological relevance, but the most significant advance may be the identification of a synthetic strategy for generating complex porous architectures from simple, amorphous materials.

1. Introduction

Diatoms are unicellular, photosynthetic organisms found in marine and freshwater environments.[1] The diatom cell is encapsulated in a porous, symmetrical shell (or *frustule*) fashioned from amorphous silica that is comprised of two valves that fit together much like a petri dish and its lid. The faces of the valves are commonly either circular (as in centric diatoms) or elongated (as in pennate diatoms) in shape, with typical dimensions in the range of 1−100 μm. The silica valves possess complex and often highly ordered arrays of nanometer- to micrometer-scale pores and slits characteristic of the diatom species (of which there are thought to be in excess of 100,000). Diatoms are so numerous that they account for around 25% of the world's turnover of silica. It is a major goal to understand, or at least mimic, biomineralization in organisms such as diatoms in order that complex microstructures may be fashioned in the laboratory.[2] In this work, a theoretical model is proposed that incorporates processes identified in experimental investigations of diatom morphogenesis, namely, the roles of templating by cellular structures and by complex-fluid structures under physicochemical control. It is shown that, with a mild degree of prepatterning (mimicking the effects of cellular structures), a fluid phase-separation mechanism can generate suitable templates for the deposition of solid materials into forms resembling a wide range of diatom structures. This process may provide a means of assembling complex, porous architectures from simple inorganic materials for technological applications.

To appreciate the widespread fascination with diatom structures, one need only glance at the small selection of optical and transmission electron microscopy images shown in Figures 2−4. The porous structures are species specific and are therefore central to taxonomic classifications.[3] The formation of amorphous-silica diatom valves during asexual reproduction has been studied in a variety of time-resolved, electron-microscopy experiments[4,5] from which the following general picture emerges.[6,7] After cell division, silica deposition occurs near the freshly exposed surfaces of the daughter cells in membrane-bound compartments called silica deposition vesicles (SDVs); the process seems to occur in two distinct stages.[7] In the first stage, a thin (~30 nm) base-layer of silica is deposited possessing "an irregular system of ribs"[3] (or *costae*) of silica emanating from near the center of the new valve. Between newly formed costae are found rafts of organic droplets and/or vesicles,[5] which may have had a role in directing the initial formation of the costae. In the second stage, silica growth proceeds normal to the base layer (leading to vertical differentiation) until the valve has acquired the necessary thickness (~10−100 nm), and the fine details of the porous structures are complete. Interestingly, the structure of the base layer does not necessarily correspond to the pore structure on the external face of the new valve; in some species, small pores in the base layer can be observed directly through the large pores in the external surface.[3] In general, the first stage of silica deposition to form the base layer is completed within 10−20 min, while the second stage of vertical differentiation can take up to several hours.[4,7−10] It would be inappropriate to summarize all of the experimentally observed variations here, but suffice to say that, depending on the diatom species, vertical differentiation has been observed to proceed in both directions normal to the base layer.[6,7]

The rib-like costae represent some of the most striking features of diatom frustules. The number of costae depends on the diatom species, but, in centric diatoms, there are typically around 10−50 emanating symmetrically from the center of the frustule. The most accurate predictive model of diatom morphogenesis to date is based on the diffusion-limited aggregation (DLA) of silica nanoparticles.[11] Amorphous particles with diameters of 1−10 nm are thought to be transported to the perimeter of the SDV (possibly via microtubules) and then released, whereupon they diffuse and aggregate to form a structure growing outward from the center of the SDV. Computer simulations of the DLA process, including the effects of simultaneous sintering (smoothing) of the growing silica structure, show that spoke-like patterns can be formed. Depending on the choice of parameters within the DLA model, the spokes may also bifurcate, leading to branched

* Corresponding author. E-mail: philip.camp@ed.ac.uk.

(1) Werner, D. *Biology of Diatoms*; Blackwell Science Ltd.: Oxford, 1977.
(2) Mann, S.; Ozin, G. A. *Nature* **1996**, *382*, 313−318.
(3) Round, F. E.; Crawford, R.; Mann, D. G. *The Diatoms: Biology and Morphology of the Genera*; Cambridge University Press: Cambridge, U.K., 1990.
(4) Schmid, A. M. M.; Schulz, D. *Protoplasma* **1979**, *100*, 267−288.
(5) Schmid, A. M. M.; Volcani, B. E. *J. Phycol.* **1983**, *19*, 387−402.
(6) Pickett-Heaps, J. D.; Schmid, A. M. M.; Edgar, L. A. *Prog. Physiol. Res.* **1990**, *7*, 1−168.
(7) Gordon, R.; Drum, R. W. *Int. Rev. Cytol.* **1994**, *150*, 243−372.
(8) Eppley, R. W.; Holmes, R. W.; Paasche, E. *Arch. Mikrobiol.* **1967**, *56*, 305−323.
(9) Darley, W. M.; Sullivan, C. W.; Volcani, B. E. *Planta* **1976**, *130*, 159−167.
(10) Sullivan, C. W.; Volcani, B. E. Silicon in the cellular metabolism of diatoms. In *Silicon and Siliceous Structures in Biological Systems*; Simpson, T. L., Volcani, B. E., Eds.; Springer-Verlag: New York, 1981.
(11) Parkinson, J.; Brechet, Y.; Gordon, R. *Biochim. Biophys. Acta* **1999**, *1452*, 89−102.

10.1021/la702278f CCC: $40.75
Published on Web 11/28/2007

structures resembling those found in certain diatom species. Thus, the spoke-like structures seen in many centric diatom valves can be reproduced with a physical mechanism. Nonetheless, it is clear that the formation of costae is likely to be strongly influenced by intracellular factors, either through the positioning of microtubules and nanoparticle "release" sites throughout the SDV, or through some sort of templating or prepatterning on the cell surface by cytoskeletal components.

In diatoms, the usual physical mechanisms of biomineralization, such as crystal nucleation and directed crystal-growth, can be ruled out since the resulting siliceous material can be considered amorphous, at least above the 10 nm scale. The structure of biosilica on the 10 nm scale has been characterized in experiments[12] and may be explained by considering the self-assembly of species-specific polypeptides[13] such as silaffins[14−17] At length scales of 100 nm or more, however, a templating mechanism may operate in which a self-assembled complex-fluid "mold" directs the deposition of inorganic material.[18] It has been suggested that organic components in the SDV that avoid coprecipitation with silica should become more concentrated as the valve thickens and occupies the volume.[7] This could lead to droplets of organic material that would form a template for the pores and the cross-costae (the ribs bridging between radial costae). Helmcke proposed a "bubble" model in which gas-filled vesicles produce a foamy structure that acts as a template for silica condensation.[19] In experiments, Schmid observed rafts of liquid-filled "spacer vesicles",[5] with diameters of about 1 μm,[20,21] that appeared to guide the growth of silica. Sumper and co-workers found amphiphilic, long-chain polyamines trapped in silica harvested from a number of diatom species,[17,22−24] which led to the proposal of a phase separation model of pore formation in diatom shells.[25] In all of these models, the organic components, which might be polyamines,[17,22−24] polypeptides,[26] or other organic macromolecules, are considered to phase separate from water onto the base layer to form a two-dimensional, self-organized array of droplets/bubbles/vesicles that acts as a template or guide for the subsequent deposition of amorphous silica.

An exact theoretical treatment of diatom morphogenesis is not yet possible because of the sheer complexity of the problem and its diverse phenomenologies. It is safe to say that, at present, there is no single model that can reproduce or explain all aspects of diatom-frustule morphology. The DLA model of Parkinson et al. goes a long way to explain the formation of radial costae,[11] but the complex and often symmetrical arrays of pores are, as yet, unexplained. Sumper's model of pore formation is based on experimental observations and a *qualitative* description of the phase-separation process.[25] In this work, we present the first quantitative test of a phase-separation mechanism for the formation of porous, siliceous structures resembling diatom valves. The central idea is that an organic component phase separates from an aqueous phase on the surface of the base layer within the SDV to form a quasi-two-dimensional emulsion of small droplets, around which a silica precursor (such as silicilic acid) in the aqueous phase can diffuse and condense to form a cast of the complex-fluid template. The initial formation of droplets is seen to be relatively fast, but the subsequent coalescence to form larger droplets, and ultimately a macroscopic interface, is an extremely slow process. The long-time dynamics of such processes are of considerable inherent interest.[27] There is likely to be coupling, and possibly cooperativity, between the processes of template formation and silica deposition, but, in this preliminary investigation, we consider these processes to occur on distinct time scales. The structure of the organic template is assumed to be essentially static over the time required for silica-precursor diffusion and condensation/aggregation; in other words, the initial array of organic droplets can be considered as a static template for the silica deposition. Under these assumptions, we show that a model of fluid phase separation in confined, two-dimensional environments, including the effects of "prepatterning" by the silica costae in the base layer, is capable of generating feasible templates for a large number of centric- and pennate-diatom valves. This will provide a starting point for future studies, which will incorporate the initial formation of the base layer (by, e.g., DLA[11]) and the coupling of phase separation with silica deposition and sintering.

The aim of this work was to explain a specific stage of diatom morphogenesis, but the resulting model corresponds to a very general physical situation, namely, the phase separation of immiscible fluids under the influences of confinement and local external fields. Therefore, the results of this work should be tested directly by a well-controlled experiment, which could then lead to a means of producing complex inorganic microstructures resembling those in diatom frustules. Some comments on the experimental relevance of the work will be presented toward the end of the article, but for now we note that analogous methods for preparing porous materials using surfactant templates[28] are already well-known and widely exploited. Transient "target" templates in phase separating complex fluids have also been described and exploited before, most commonly in polymer blends.[29−31] Finally, "surfactant-free" routes have been identified in which the precursor of an inorganic material may, in essence, self-organize to direct the deposition.[32]

The rest of this article is organized as follows: In section 2, the model and computational methods are detailed. Simulation results for specific centric and pennate diatoms are presented in section 3, and section 4 concludes the paper.

2. Model and Methods

The complexity, diversity, and species-specificity of diatom structures preclude a detailed chemical account of morphogenesis, so instead we seek a generic model of the putative phase-separation mechanism. The system is modeled as a quasi-two-

(12) Noll, F.; Sumper, M.; Hampp, N. *Nano Lett.* **2002**, *2*, 91−95.
(13) Lenoci, L.; Camp, P. J. *J. Am. Chem. Soc.* **2006**, *128*, 10111−10117.
(14) Kröger, N.; Deutzmann, R.; Sumper, M. *Science* **1999**, *286*, 1129−1132.
(15) Kröger, N.; Lorenz, S.; Brunner, E.; Sumper, M. *Science* **2002**, *298*, 584−586.
(16) Poulsen, N.; Sumper, M.; Kröger, N. *Proc. Natl. Acad. Sci. U.S.A.* **2003**, *100*, 12075−12080.
(17) Sumper, M.; Kröger, N. *J. Mater. Chem.* **2004**, *14*, 2059−2065.
(18) Dabbs, D. M.; Aksay, I. A. *Annu. Rev. Phys. Chem.* **2000**, *51*, 601−622.
(19) Helmcke, J. G. *Recent Adv. Bot.* **1959**, *1*, 216−221.
(20) Schmid, A. M. M. Schalenmorphogenese in diatomeen. In *Diatomeen I, Schalen in Natur and Technik*; Bach, K., Burkhardt, B., Eds.; Cramer Verlag: Stuttgart, Germany, 1984.
(21) Schmid, A. M. M. Wall morphogenesis in *Coscinodiscus wailesii* Gran et Angts. II. Cytoplasmic events of valve morphogenesis. In *Proceedings of the Eighth International Symposium on Living and Fossil Diatoms*; Ricard, M., Ed.; O. Koeltz: Koenigstein, Germany, 1986.
(22) Kröger, N.; Deutzmann, R.; Bergsdorf, C.; Sumper, M. *Proc. Natl. Acad. Sci. U.S.A.* **2000**, *97*, 14133−14138.
(23) Brunner, E.; Lutz, K.; Sumper, M. *Phys. Chem. Chem. Phys.* **2004**, *6*, 854−857.
(24) Lutz, K.; Gröger, C.; Sumper, M.; Brunner, E. *Phys. Chem. Chem. Phys.* **2005**, *7*, 2812−2815.
(25) Sumper, M. *Science* **2002**, *295*, 2430−2433.
(26) Hecky, R. E.; Mopper, K.; Kilham, P.; Degens, E. T. *Mar. Biol.* **1973**, *19*, 323−331.
(27) Bray, A. J. *Adv. Phys.* **1994**, *43*, 357−459.
(28) Kresge, C. T.; Leonowicz, M. E.; Roth, W. J.; Vartuli, J. C.; Beck, J. S. *Nature* **1992**, *359*, 710−712.
(29) Karim, A.; Douglas, J. F.; Nisato, G.; Liu, D.-W.; Amis, E. J. *Macromolecules* **1999**, *32*, 5917−5924.
(30) Clarke, N. *Phys. Rev. Lett.* **2002**, *89*, 215506.
(31) Buxton, G. A.; Clarke, N. *Macromol. Symp.* **2006**, *233*, 102−107.
(32) Collins, A.; Carriazo, D.; Davis, S. A.; Mann, S. *Chem. Commun.* **2004**, 568−569.

dimensional, two-component incompressible fluid mixture with fixed overall composition. The x, y, and z dimensions of the system are L, L, and l, respectively, with $l \ll L$ reflecting the quasi-two-dimensional geometries of the SDV and the resulting face of the diatom valve. The composition of the fluid is assumed to depend only on the lateral coordinates x and y. Component 1 is the organic material and component 2 is aqueous. The parameter signaling phase separation (demixing) is the local excess volume fraction of organic material, given by $\phi(x,y) = \phi_1(x,y) - \phi_2(x,y) = 2\phi_1(x,y) - 1$, where $0 \leq \phi_i(x,y) \leq 1$ is the local volume fraction of component i. Mass conservation implies that the quantity

$$\bar{\phi} = \frac{1}{L^2}\int_L \int_L \phi(x,y)\mathrm{d}x\mathrm{d}y \tag{1}$$

representing the overall composition, is a constant. Phase separation is driven by the requirement to minimize the free energy, which, in the current model, is represented by the equation

$$F[\phi] = \frac{l}{v_0}\int_L \mathrm{d}x \int_L \mathrm{d}y\left[\epsilon\left(-\frac{1}{2}\phi^2 + \frac{1}{4}\phi^4\right) + \kappa_1\left|\nabla\phi\right|^2 + \kappa_2(\nabla^2\phi)^2 + h\phi\right] \tag{2}$$

where v_0 is a molecular volume. The first two terms (proportional to ϕ^2 and ϕ^4) describe the local free-energy per particle with energy scale ϵ; this familiar Landau-theory expression drives phase separation into coexisting phases with $\phi = \pm 1$.[33] The square-gradient and Laplacian terms, with coefficients κ_1 and κ_2, respectively, are the first two terms in an expansion of the interfacial free energy[34−36] In the final term, $h(x,y)$ models the local field arising from prepatterning by the pre-existing silica costae within the base layer; the charged silica surface will provide an attractive field for the aqueous component and a repulsive field for the organic component. Gradients in the chemical potential give rise to a flux in ϕ given by $\mathbf{j} = -M\nabla\mu$, where $M(x,y)$ is the local mobility. The constitutive relation for an incompressible fluid is $\partial\phi/\partial t + \nabla\cdot\mathbf{j} = 0$. The phase-separation dynamics is therefore described by integrating the differential equation

$$\frac{\partial\phi}{\partial t} = \nabla\cdot(M\nabla\mu) \tag{3}$$

where the local chemical potential is given by the functional derivative of the free-energy functional in eq 2:

$$\mu = \frac{\delta F}{\delta\phi} = \epsilon\phi(\phi^2 - 1) - \kappa_1\nabla^2\phi + \kappa_2\nabla^2(\nabla^2\phi) + h \tag{4}$$

In all simulations, the perimeter of the diatom valve was taken to be an ellipse with a boundary defined by $(x/a)^2 + (y/b)^2 = 1$, where a and b are the ellipse semi-axes (for centric diatoms, $a = b$). A schematic diagram of the simulation cell dimensions is shown in Figure 1. In the rare case of a concentric field in a centric diatom, we define an additional angle $\beta = 2\pi\sqrt{x^2+y^2}/a$, where $a = b$ is the radius of the circular domain describing the diatom valve. To retain the convenience of solving the equation of motion (eq 3) numerically on a Cartesian grid, the elliptical

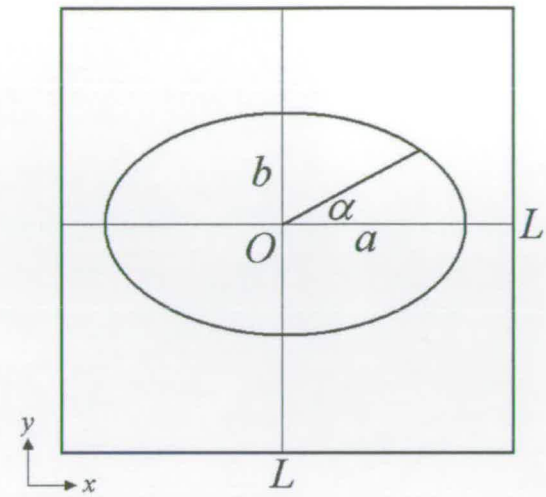

Figure 1. Schematic of the simulation cell. L is the box length, O is the origin, and a and b are the semi−major and semi−minor axes, respectively.

diatom boundary was established by allowing the mobility to depend on the position, interpolating smoothly between a value M_0 inside the boundary and zero outside the boundary. For convenience, the expression used was

$$M(x,y) = \frac{M_0}{[1 + \mathrm{e}^{(R-S)/W}]} \tag{5}$$

where W controls the width of the boundary, R is the sum of the distances between the point (x,y) and the two foci of the ellipse, and S is the sum of the distances between a point on the boundary of the ellipse and the two foci (which is always equal to twice the major semi-axis). The width W was made small compared to the diatom dimensions so that the boundary was relatively sharp but still continuous; this meant that complicated discontinuous boundary conditions did not have to be accommodated within the numerical scheme. The dynamical eq 3 was integrated numerically using a three-point, finite-difference algorithm[37] on a square Cartesian grid with spacing l and periodic boundary conditions applied. The integration time step was adjusted to conserve $\bar{\phi}$ to within 1 part in 10^4. All calculations were performed in dimensionless units defined using the grid spacing l, the energy ϵ, and the basic unit of time $\tau = l^2/\epsilon M_0$: dimensions L/l (and equivalent expressions for a, b, and W); time t/τ; interfacial energy parameters $\kappa_1^* = \kappa_1/\epsilon l^2$ and $\kappa_2^* = \kappa_2/\epsilon l^4$; and prepattern field $h(x,y)/\epsilon$. τ is the most obvious unit of time for calculations based on a grid with spacing l, although one could also define a unit based on a natural length scale, such as the equilibrium width of an interface separating coexisting phases. This choice is made solely on the basis of convenience, and the conversion from simulation time to real time (such as in section 3) will still yield the correct results.

Parameters were adjusted heuristically to generate a particular diatom structure. In each case, the initial state of the fluid was an almost homogeneous mixture with a ±1% random variation in ϕ among 200 × 200 (or occasionally 350 × 350) cells on a square grid of side L and spacing l. (The exact size of the initial, random variations does not affect the final results.) Then, phase separation was allowed to occur as a result of mutual diffusion of organic and aqueous components, driven by local free-energy

(33) Chaikin, P. M.; Lubensky, T. C. *Principles of Condensed Matter Physics*; Cambridge University Press: Cambridge, U.K., 1995.
(34) Cahn, J. W.; Hilliard, J. E. *J. Chem. Phys.* **1958**, *28*, 258−267.
(35) Teubner, M.; Strey, R. *J. Chem. Phys.* **1987**, *87*, 3195−3200.
(36) Gompper, G.; Schick, M. Self-assembling amphiphilic systems. In *Phase Transitions and Critical Phenomena*; Domb, C., Lebowitz, J. L., Eds.; Academic Press: London, 1994; Vol. 16.
(37) Pang, T. *An Introduction to Computational Physics*, 1st ed.; Cambridge University Press: Cambridge, U.K., 1997.

Table 1. Model Parameters Used to Generate the Simulated Diatom Structures Shown in Figures 2−5[a]

figure	species	L/l	$\bar{\phi}_{in}$	$\bar{\phi}_{ex}$	κ_1^*	κ_2^*	a/l	b/l	W/l	$h(x,y)/\epsilon$	t/τ
2a	*Arachnoidiscus ehrenbergii*[49]	200	−0.3	+0.0	0.2		70	70	1	$0.5\cos^{10}(8\alpha)$	3.00
2b	*Surinella linearis v. helvetica*[50]	200	−0.65	−0.65	0.2	0.05	60	25	4	$0.4\cos^{2}(8\alpha)$	1000.00
2c	*Actinocyclus confluens*[49]	200	−0.4	−0.2	0.4		90	90	1	$0.3\cos^{10}(\beta)$	10.90
3a	*Stictodiscus californicus*[49]	200	−0.4	−0.3	0.6		40	40	4		30.00
3b	*Psammodiscus nitidus*[51]	200	−0.4	−0.3	0.43		60	50	6		18.00
3c	*Aulacodiscus argus*[49]	350	−0.3	−0.3	0.4		100	100	8		8.00
3d	*Actinoptychus undulatus*[49]	200	−0.4	−0.4	0.3		60	60	6	$[0.02(0.1+\sin^2(4\alpha)]/[0.1+\cos^2(4\alpha))]$	10.00
3e	*Actinoptychus campanulifer*[49]	200	−0.3	+0.0	0.2		60	60	6	$1/[1+10\sin^2(3\alpha)]$	2.80
3f	*Cyclotella meneghiniana*[50]	200	−0.5	−0.5	0.2		60	60	4	$0.4\cos^2(18\alpha)$	2800.00
3g,5	*Melosira sol*[49]	200	−0.2	−0.2	0.5		60	60	6	$0.18\cos^2(26\alpha)$	20.00
3h	*Stictodiscus johnsonianus*[49]	200	−0.3	−0.1	0.6		60	60	3	$0.06\cos^2(12\alpha)$	20.75
3i	*Arachnoidiscus indicus*[49]	200	−0.5	−0.5	0.4		50	50	1	$0.08\cos^8(8\alpha)+0.05\cos^8(4\beta)$	10.60
3j	*Stephanodiscus*[52]	200	−0.5	−0.1	0.3		60	60	1	$0.15\sin^4(6\alpha)$	13.00
3k	*Psammodiscus*[52]	200	−0.6	−0.6	0.1		40	40	6	$0.1\cos^2(4\alpha)$	50.00
3l	*Aulacodiscus kittonii*[49]	200	−0.35	−0.1	0.5		70	70	1	$[0.05\ (0.1+\cos^2(2\alpha)]/[0.1+\sin^2(2\alpha))]$	10.70
4a	*Cocconeis disculoides*[51]	200	−0.45	−0.1	0.5	0.08	70	38	2.5		20.80
4b	*Achnanthes parvula*[51]	200	−0.3	−0.3	0.5	0.1	60	5	4		35.00
4c	*Achnanthes parvula*[51]	200	−0.3	−0.3	0.3	0.06	70	30	2	$0.1\sin^2(\alpha)$	9.00

gradients as computed from eq 4. Long-lived structures adopted by the phase-separating fluid are sensitive to the average excess concentration of organic material, as measured by the conserved quantity $\bar{\phi}$. In the absence of the local field $h(x,y)$, the time-dependent phase-separation structures are well-known: when $\bar{\phi} \ll 0$ or $\bar{\phi} \gg 0$, long-lived droplets of organic and aqueous phases, respectively, are formed so as to minimize the interfacial free energy; when $\bar{\phi} \simeq 0$, labyrinthine spinodal structures result. As a rule, it was found that the composition of the fluid had to be adjusted such that $\bar{\phi} \simeq -0.3$, corresponding to a volume fraction of organic component of about 0.35; this relatively low volume fraction means that the organic material forms droplets in water. In some cases, the organic fractions inside and outside the valve perimeter ($\bar{\phi}_{in}$ and $\bar{\phi}_{ex}$, respectively) were altered independently to "fine-tune" the template structure at the boundary, but this was by no means vital, and the effects on the interior structures were seen to be negligible. The simulation parameters are reported in Table 1.

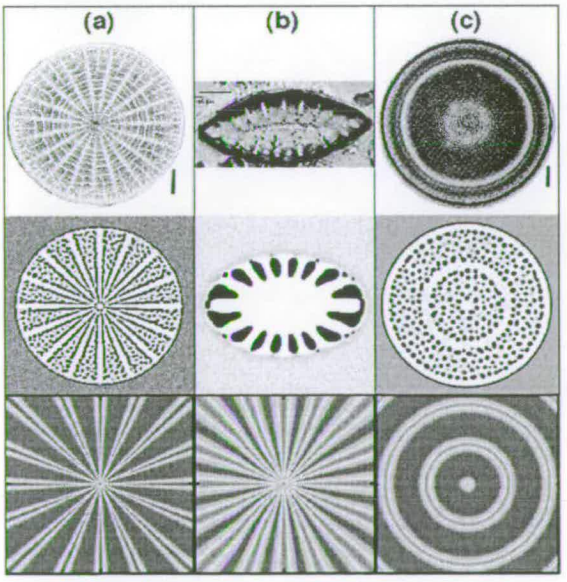

Figure 2. Experimental (top) and simulated (middle) images of diatom structures, and the prepattern field (bottom) required for each simulated structure: (a) *Arachnoidiscus ehrenbergii*;[49] (b) *Surinella linearis v. helvetica*;[50] (c) *Actinocyclus confluens*.[49] In the simulated images, the dark regions correspond to organic-rich domains. In the prepattern fields, blue and red correspond to low and high free-energy regions, respectively. Scale bars are 10 μm. Experimental images are reproduced with permission.

3. Results

Figure 2 compares experimental and simulated structures for three different diatom species, and the simulated prepatterning field $h(x,y)$ required as input in eq 2. The colors in the experimental images arise from diffraction effects, and do not reflect any pigmentation or staining of the silica. In the instantaneous simulated structures, the black regions denote high concentrations of organic material ($\phi \gg 0$), representing the template for silica deposition. The white regions ($\phi \ll 0$) therefore indicate the aqueous domains where the silica will condense. In the case of the centric diatom *Arachnoidiscus ehrenbergii* in Figure 2a, the formation of the radial spokes in the simulated structure is dictated by the prepatterning field shown, which may correspond to the influence of costae in the base layer. Cross-costae are not apparent in the simulated structure, but the overall similarity with the experimental image is high. The gross features of the pennate diatom *Surinella linearis v. helvetica* can be modeled using an elliptical domain and a radial prepatterning field, as shown in Figure 2b. It is also possible to mimic structures with apparent concentric-ring motifs, such as the *Actinocyclus confluens* shown in Figure 2c. The diffraction colors in the experimental image highlight variations in the density of silica in the frustule, which can be matched by the model.

Figure 3 shows a selection of observed and simulated centric-diatom structures. In Figure 3a−c, there are no prepatterning fields, and the simulated structure consists of a disordered array of droplets, which provides a template for a disordered array of pores. The key variables here are the overall concentration of organic material $\bar{\phi}$, and the diameter of the circular cell a. The structures are, by themselves, not so surprising, but these images serve to illustrate the complementarity of the pore structure of the diatom valve and the droplet structure of the fluid template. In the remaining figures, there is a clear requirement for prepatterning; each of the diatoms possesses highly developed costae emanating from the center of the face of the valve. Figure 3g,h in particular requires further comment. For these species (*Melosira sol* and *Stictodiscus johnsonianus*, respectively), the simulated template structure switches over from droplets near the center to spokes near the perimeter. The crossover arises spontaneously in the simulations: near the center, the spacing between minima in the prepatterning field is small compared to the characteristic droplet size, and so, in terms of the free energy, it is more favorable for the droplets to remain intact than for them to break up and collect in the minima; near the perimeter, the free energy can be lowered by the droplets coalescing in the minima, thus forming spokes. (The characteristic droplet size is,

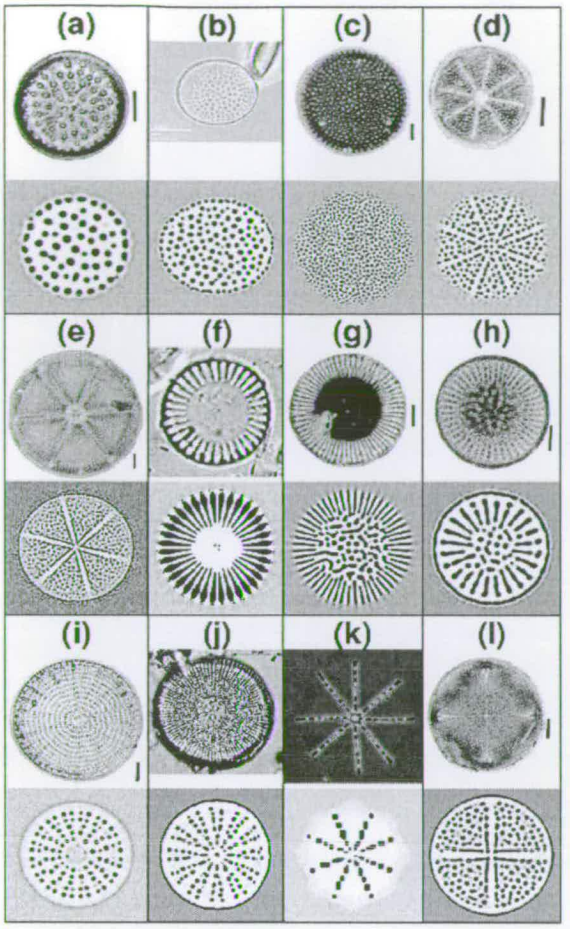

Figure 3. Experimental (upper) and simulated (lower) structures of centric diatoms: (a) *Stictodiscus californicus*;[49] (b) *Psammodiscus nitidus*;[51] (c) *Aulacodiscus argus*;[49] (d) *Actinoptychus undulatus*;[49] (e) *Actinoptychus campanulifer*;[49] (f) *Cyclotella meneghiniana*;[50] (g) *Melosira sol*;[49] (h) *Stictodiscus johnsonianus*;[49] (i) *Arachnoidiscus indicus*;[49] (j) *Stephanodiscus*;[52] (k) *Psammodiscus*;[52] (l) *Aulacodiscus kittonii*.[49] In the simulated images, the dark regions correspond to organic-rich domains. Scale bars are 10 μm, except in panel j, which is 20 μm. Experimental images are reproduce with permission.

of course, time-dependent; it increases like $t^{1/3}$.[27,38]) In Figure 3i (*Arachnoidiscus indicus*) the concentric organization of pores (droplets) is driven by an additional concentric field: it is emphasized that the physical origin of such a field has not yet been identified; it has only been invoked in this case, and that of *Actinoicyclus confluens* shown in Figure 2c.

Some results for pennate diatoms are shown in Figure 4. Pennate diatoms often possess parallel *striae* (rows of pores) aligned parallel to the long axis of the valve.[7] We found that these features were favored specifically by the inclusion of a weak $(\nabla^2\phi)^2$ term in eq 2. It is known that in models of three-dimensional oil−water−surfactant solutions, such a term is required to stabilize modulated cubic (bicontinuous) phases.[39−41] In two dimensions, this might be expected to favor a "square" array of pores, as required in pennate diatoms. Indeed, Figure 4 shows that the experimental structures could be templated by a phase-separated structure, provided that κ_2 is nonzero. In an experiment, this might require the addition of a surfactant to the organic and

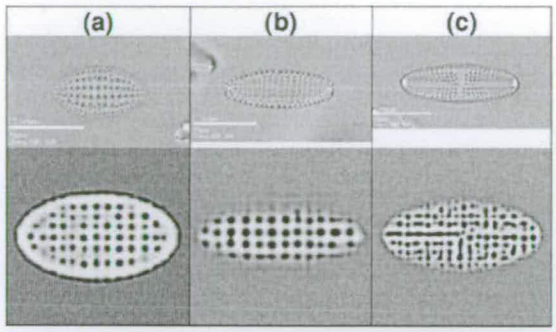

Figure 4. Experimental (upper) and simulated (lower) structures of pennate diatoms: (a) *Cocconeis disculoides*;[51] (b) *Achnanthes parvula*;[51] (c) *Achnanthes parvula*.[51] In the simulated images, the dark regions correspond to organic-rich domains. Scale bars are 10 μm. Experimental images are reproduced with permission.

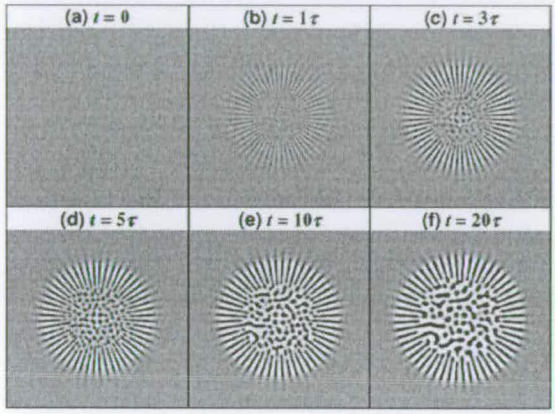

Figure 5. Simulation images of the diatom *Melosira sol* at times (a) $t = 0$, (b) $t = 1\tau$, (c) $t = 3\tau$, (d) $t = 5\tau$, (e) $t = 10\tau$, and (f) $t = 20\tau$.

aqueous components. Note that, in the simulated centric diatoms, $\kappa_2 = 0$, and hence no surfactant should be required.

The majority of the simulated images presented in this work are "snapshots" of the fluid template at some particular late stage of the simulation. In Figure 5, we show a representative example of the time dependence of phase separation; the particular diatom is *Melosira sol* shown in Figure 3g. Figure 5a shows the initial, homogeneous state. At short times $t^* \sim 1$, the only apparent structures are the spokes near the perimeter of the circular cell. The interior of the circular domain is still essentially homogeneous. At $t^* \sim 5$ the fluid has produced two distinct regions, spokes near the perimeter and droplets in the interior. These motifs are long-lived, and persist up to and well beyond times $t^* \sim 10$. The structure is essentially static at times beyond $t^* \sim 20$, and therefore corresponds to a quasi-static template that might direct the deposition of silica to form a porous valve. The wide range of time scales reported in Table 1 reflects the different distributions of droplets in the fluid-phase templates. For example, the parameters required for the diatoms in Figure 3a,b are comparable, except for the choices of κ_1^* and t/τ. A larger value of κ_1^* is required to generate the target structure in Figure 3a, which consists of a small number of large droplets; Figure 3b shows a large number of small droplets. Given that both the compositions and diatom dimensions are comparable, the structure in Figure 3b forms faster than that in Figure 3a because of the distances over which the organic material has to diffuse. The slowest forming templates (in Figures 2b and 3f) are characterized by a complete absence of organic material near the center. The

(38) Huse, D. A. *Phys. Rev. B* **1986**, *34*, 7845−7850.
(39) Gompper, G.; Klein, S. *J. Phys. II* **1992**, *2*, 1725−1744.
(40) Komura, S.; Kodama, H. *Phys. Rev. E* **1997**, *55*, 1722−1727.
(41) Gonnella, G.; Ruggieri, M. *Phys. Rev. E* **2002**, *66*, 031506.

simulations are long in these cases because of the time required for complete evacuation of the central regions.

The major conclusion of this work is that the pore structures of the valves in a diverse range of diatom species can be mimicked qualitatively by a simple fluid phase separation model. We are not seeking precise reproductions of the observed diatom structures; to mimic every last detail would require a much more complicated and unwieldy model, which takes account of processes on a variety of length scales (including, for example, simultaneous costa formation, self-assembly of biomolecules and colloidal silica on the 1−10 nm scale, the chemistry of silica condensation, etc.). Nonetheless, the gross features of the diatom frustule, specifically the costae and the pores, can be produced "in negative" by a phase-separated, fluid template.

The biological relevance of the results can only be assessed through further (challenging) experiments with real diatoms. From a materials-chemistry perspective, however, the model makes predictions that could be readily tested. After all, the model is essentially one of phase separation in a thin fluid layer on a patterned substrate. Hence, it should be possible to test the predictions by preparing emulsions on hydrophilic−hydrophobic patterned surfaces, the latter being prepared by lithographic techniques, for example. In order to estimate the physical parameters required to produce the theoretically predicted template structures, we must convert the dimensionless simulation parameters in to real units. The fluid composition $\bar{\phi}$ is defined in terms of volume fractions and can therefore be read off directly from Table 1. The grid spacing is $l \sim 10^{-7}$ m because $\sim 10^2$ points are used to represent a typical diatom dimension of $\sim 10\,\mu$m; all cell dimensions in Table 1 are reported as multiples of l.

The numerical values of κ_1^* can be rationalized by relating κ_1 for a planar interface to the interfacial tension γ between phase-separated organic and aqueous domains. The calculation is standard,[34,42] and, for the specific free-energy functional presented in eq 2, the result is $\kappa_1 = 9\gamma^2 v_0^2/16\epsilon$, so that

$$\kappa_1^* = \left(\frac{3\gamma v_0}{4\epsilon l}\right)^2 \tag{6}$$

The interfacial tensions between water and typical organic liquids are normally several millijoules per square-meter,[43] and so $\gamma \sim 10^{-2}$ J m^{-2}. The molecular volume $v_0 \sim 10^{-27}$ m^3 may be estimated from typical molecular dimensions of 10 Å and, as noted earlier, the grid spacing $l \sim 10^{-7}$ m. Finally, the energy parameter ϵ driving phase separation (see eq 2) is unlikely to be much more than 0.1 $k_B T$, where k_B is Boltzmann's constant and T is the temperature. Combining these order-of-magnitude estimates in eq 6 gives $\kappa_1^* \sim 0.5$, which is very close to the typical values determined heuristically in the simulations (reported in Table 1).

The order-parameter profile across a planar interface is $\phi(x) = \tanh(x/2\xi)$,[34,42] where the interfacial width $\xi = \sqrt{\kappa_1/\epsilon}$. From the numerical values obtained above, we estimate that $\xi \sim 10^{-8}$ m, which is small compared to the dimensions of the porous structures reported in section 3; hence, the resolution of the simulated images should be attainable in experiment.

The typical strength of the prepatterning field (measured by the difference between the minimum and maximum field) is, from Table 1, less than 0.5ϵ. With the assumption made above for ϵ, this equates to around 0.05$k_B T$, which does not seem excessively strong. As for the basic unit of time, $\tau = l^2/\epsilon M_0$, it is difficult to estimate the mobilities, or the diffusion coefficient $D = M/k_B T$, of organic molecules in as confined a space as the SDV. The Stokes−Einstein expression for a spherical solute of radius $R \sim 10$ Å in a water-like solvent with viscosity $\eta \sim 10^{-3}$ Pa s gives $D = k_B T/6\pi\eta R \sim 10^{-10}$ m^2 s^{-1}. In combination with the estimates of l and ϵ given above, we find that $\tau \sim 10^{-3}$ s. The simulation times reported in Table 1 therefore correspond to real times from tens to thousands of milliseconds. These are probably serious underestimates because of the likely macromolecular crowding within the SDV and the effects of confinement; if the mobility M_0 is decreased, then the basic unit of time $\tau \sim 1/M_0$ increases. Hence, the reduced times reported in Table 1 may well correspond to biologically relevant time scales (seconds and minutes).

It is strongly emphasized that these are very rough, order-of-magnitude estimates, intended only to show that the simulation results are physically reasonable.

4. Conclusions

From a materials-science perspective, it may be neither possible nor necessarily desirable to mimic the precise details of diatom structures on every length scale. A given application might only require a material with a well-defined pore structure of a particular dimension. Nonetheless, in this work we have shown that the basic structural features of the diatom valve may be templated by long-lived domains in phase-separating fluids, controlled by a balance of confinement, composition, interfacial tension, and a mild degree of prepatterning (which may be present in real diatoms). As far as we are aware, we have presented the most accurate, quantitative model of the pore structure in diatom valves to date.

It should be possible to meet the necessary physical conditions for template formation in the laboratory, which would then lead to the production of synthetic diatom valves and other complex microstructures fashioned from simple solids. The strength of the prepatterning field $h(x,y)$ need only be about one tenth of the characteristic energy ϵ, and a prepatterned surface could be fashioned using lithographic techniques. The required values of κ_1 correspond to typical values of the interfacial tension γ for water and organic liquids, and the dimensions of the confining cell are on the 10 μm scale. Experimental tests of the theoretical predictions are eagerly anticipated.

From the biological perspective, this work represents only a preliminary study. Future work should concentrate on combining the phase-separation process presented here, along with the DLA of silica nanoparticles thought to be responsible for the formation of costae in the underlying base layer. In addition, the condensation of silica and thickening of the frustule (vertical differentiation) should be accounted for simultaneously with phase separation. The basic assumption made here is that phase separation and silica condensation occur on distinct time scales, and that the fluid template is essentially static on the time scale for silica condensation. Experiments indicate that the base layer is formed within minutes while vertical differentiation can take up to several hours. This suggests that, to a first approximation, the assumption of a static fluid template is justified. Nonetheless, it should be possible to model these processes simultaneously without making any strong assumptions a priori. A specific process of interest is the formation of hexagonal "close-packed" arrays of pores, which are featured in the valves of some diatom species.[3] In Thompson's classic work *On Growth and Form*,[44] the hexagonal

(42) Rowlinson, J. S.; Widom, B. *Molecular Theory of Capillarity*; Dover Publications, Inc.: Mineola, NY, 2002.
(43) Donahue, D. J.; Bartell, F. E. *J. Phys. Chem.* **1951**, *56*, 480−484.
(44) Thompson, D. W. *On Growth and Form*; Cambridge University Press: Cambridge, U.K., 1917.

array of pores is attributed to "electromagnetic vibrations" on the surface of the cell "like standing waves on drums".[7] There are a number of dynamical mechanisms by which such arrays might arise;[7] in two dimensions, these have been generated from equations of the Cahn–Hilliard or Landau–Ginzburg type for three-component, phase-separating, *reactive* fluids[45,46] and phase-separating adsorbates.[47]

The present model was inspired by the results of experimental observations of diatom morphogenesis, and so it may shed some light on a specific stage of the biological mechanism (although, of course it offers no insight on the nature and extent of cellular control). In nature, there are a number of mechanisms by which complex patterns are known to be formed. The distribution of reacting compounds and pigments can be described by a reaction–diffusion equation (Turing equation), which explains, for example, leopards' rosettes and tigers' stripes.[48] In this case, the patterns are associated with mathematical instabilities in the underlying reaction–diffusion equation. However, no two tigers have the exactly the same set of stripes, and this is a very different situation from that in diatoms; the structures of the diatoms within a given single-species colony are essentially identical, at least on the 100 nm scale. It therefore seems unlikely that a reaction–diffusion mechanism applies to diatom morphogenesis, and in any case, the experimental clues point much more clearly toward the type of phase-separation mechanism described in this work. Experimental studies will shed light on whether the simple model presented here, and Occam's law of parsimony, are sound.

Acknowledgment. L.L. thanks the School of Chemistry at the University of Edinburgh for support. We are grateful to Prof. John Hodgkiss (Fleetwood, England),[49] Dr. Rex Lowe (Bowling Green State University, Bowling Green, OH),[50] Prof. David Mann (Royal Botanic Garden Edinburgh),[51] and Dr. Hans Schrader (Ulset, Norway)[52] for granting permission to reproduce experimental images of diatoms. Finally, we are extremely grateful to Prof. Richard Gordon (University of Manitoba, Canada) and Prof. David Mann for helpful discussions and correspondence.

LA702278F

(45) Okuzono, T.; Ohta, T. *Phys. Rev. E* **2001**, *64*, 045201(R).
(46) Sugiura, S.; Okuzono, T.; Ohta, T. *Phys. Rev. E* **2002**, *66*, 066216.
(47) Verdasca, J.; Borckmans, P.; Dewel, G. *Phys. Rev. E* **1995**, *52*, R4616–R4619.
(48) Murray, J. D. *Mathematical biology*; Springer-Verlag: Berlin, 1989.
(49) Dickman, M.; Hodgkiss, J.; Cheng, Z.; Gao, Y. *Diatoms from South China Sea*; University of Hong Kong: Hong Kong. http://life.xmu.edu.cn/diatom/diatomphoto/mainmenu.htm (accessed Feb 2007).
(50) BGSU Center for Algal Microscopy and Image Digitization Home Page. http://www.bgsu.edu/departments/biology/facilities/algae/index.html (accessed Feb 2007).
(51) Algae World database of the Royal Botanic Garden Edinburgh. http://rbg-web2.rbge.org.uk/algae/ (accessed Feb 2007).
(52) Schrader, H. Private communication.